# DEVELOPMENT OF SINGLE WALL CARBON NANOTUBE TRANSPARENT CONDUCTIVE ELECTRODES FOR ORGANIC ELECTRONICS

A Dissertation
Presented to
The Academic Faculty

by

Roderick Kinte´ Jackson

In Partial Fulfillment
of the Requirements for the Degree of
Doctor of Philosophy in the
George W. Woodruff School of Mechanical Engineering

Georgia Institute of Technology
August 2009

# DEVELOPMENT OF SINGLE WALL CARBON NANOTUBE TRANSPARENT CONDUCTIVE ELECTRODES FOR ORGANIC ELECTRONICS

Approved by:

Dr. Samuel Graham, Advisor
School of Mechanical Engineering
*Georgia Institute of Technology*

Dr. Srinivas Garimella
School of Mechanical Engineering
*Georgia Institute of Technology*

Dr. Shreyes Melkote
School of Mechanical Engineering
*Georgia Institute of Technology*

Dr. Jud Ready
School of Materials Science / GTRI
*Georgia Institute of Technology*

Dr. Bernard Kippelen
School of Electrical Engineering
*Georgia Institute of Technology*

Date Approved: 6/18/2009

# ACKNOWLEDGEMENTS

But by the grace of God I am what I am, and His grace toward me did not prove vain; but I labored even more than all of them, yet not I, but the grace of God with me.

-1 Corinthians 15:10 (New American Standard Bible)

I would like to first acknowledge my Lord and Savior Jesus Christ. It is only by the grace of God that I have progressed to this point. Everything I have thus accomplished and the many things I look forward to achieve are only possible by God's unmerited grace upon me. God has been faithful and has provided me with the energy, support, time, motivation, finances, intellect, perseverance, and scientific results necessary for the research presented in this dissertation. God and Science are not mutually exclusive and I pray my life and work will serve as testament and empirical proof of this truth. I truly believe that Science is the attempt to systematically investigate the many works of God to attain knowledge and discernment. I wish I could hasten the day when an appreciation of God and Science are embraced and not set as warring ideals. I will continue to reject the false choice of God or Science that has been presented by many, as I continue in my own quest to leverage my scientific studies as a means to better understand and appreciate God.

I want thank my family for their love, support, and prayers during this time. I would like to acknowledge my wife, Nadriene for making the sacrifice to pack up everything and head east to Atlanta with me so that we could embark upon my doctoral studies. I also thank her for enduring the many nights that I worked through my laboratory and dissertation writing challenges audibly in my sleep. I thank my momma who has epitomized "a mother's love" for 32 years and rendered "No Charge". Momma

and Daddy have always been a constant support in every endeavor I have set out to do and for that I am most appreciative. I thank my father for the example he has been for me. There have been many days and nights that I knew that I could do the work necessary to complete the task ahead because I had witnessed my father do the same many times before. I thank my siblings, with special appreciation to Debbie, Irene, Matt, and Keith. It really meant a lot to have loving siblings that I knew wanted me to achieve to my fullest ability and would do whatever they could to enable that. I thank Irene for the timely "joke-cracking" emails. I acknowledge Jasen, my nephew, for his support and love.

I acknowledge both the Jackson and Ward extended families. I have always been made to feel proud to be a Jackson and have always known how much my extended families loved me and supported me. For that I am thankful. No matter how bad things got in the laboratory, I knew of at least 300 people who shared my lineage that considered me to be "somebody". In special remembrance of my Aunt Lettie, who passed away during my doctoral studies. As the song goes, "She was a very special lady".

I acknowledge all of my friends who have been a support during this process. I am appreciative of the friendship rendered by Rodney, Kevin, Mike, Mela, Dimitri, Seyhan, Jamal, Ashley, Chris, Kelly, Malcolm, Jerriot, Brent, Ashish, Vish, and Jermaine over the last four years. I am indebted to Teddy for often providing a listening ear, sincere empathy, and timely wit during the many challenges of this process.

I want to acknowledge Dr. Samuel Graham and the Graham research group. I am glad and appreciative to have had the opportunity to work under the advisement of Dr.

Graham. After four years, I cannot recall any other graduate student that I have encountered that could speak of a better student / advisor relationship. I am grateful of the environment facilitated by Dr. Graham that promoted scientific growth and maturity. I am also appreciative of the fact that I could get excited about a research discovery in the laboratory and mistakenly revert to cultural colloquialisms in our discussions, such as "this is a tight result". I am grateful for the time extended by Adam Christensen to answer a question, or simply listen to me talk about a topic mostly so that I hear myself. I appreciate his personality extension beyond the world of science that allowed us to have fruitful non-technical conversations. I am thankful to Dr. Thomas Beechem for the many, many discussions about science, religion, and life that we have shared in our time at GT together. Thomas served as a colleague and true friend throughout this process. Thanks to group members (past and present) Namsu, Chris, Ashante, Fernando, Minseok, Yongjin, Sukwon, Prem, Steven, Eric, and Abe.

I would like to thank Dr. Mahera "Mimi" Philobos for her support and advice that given to me throughout my tenure at Georgia Tech since in 1997. Mimi has been a constant motivation and was the first person to tell me that I should get a PhD. I thank Dr. Gary May for his sound advice and professional mentorship offered to me. I also thank Terrance Mosley for his mentorship since 1994 when I first expressed interest in attending Georgia Tech. I would like to thank Dr. Raymond Vito for his professional advice and our long conversation in July 2004 that stressed the importance of developing a career in your passion that led to my return to Georgia Tech to attain my doctorate. I thank Drs. Valerie Thomas and Marilyn Brown for providing most helpful instruction, guidance, and mentorship in the energy policy and technology arena. In addition to

attaining my Mechanical Engineering doctorate during my graduate studies at Georgia Tech, they have facilitated a level of knowledge and understanding of the intersection of energy technology and policy that will enable me to make the type of social impact I that I wish to do in the future.

I thank Drs. Bernard Kippelen and Neal Armstrong for providing access to their students, expertise, and laboratory equipment throughout my doctoral studies. I acknowledge my PhD reading committee members: Drs. Srinivas Garimella, Shreyes Melkote, Jud Ready, and Bernard Kippelen. I am appreciative of the helpful advice offered during my dissertation completion process.

I acknowledge the ONR/HBEC Fellowship program, Georgia Tech Facilitating Academic Careers in Engineering and Science (FACES) program, George W. Woodruff School of Mechanical Engineering, and the Center for Materials and Devices for Information Technology Research (CMDITR) as funding providers.

# TABLE OF CONTENTS

# LIST OF TABLES

# LIST OF FIGURES

# LIST OF SYMBOLS AND ABBREVIATIONS

| | |
|---|---|
| 1-D | one-dimensional |
| 2-D | two-dimensional |
| 3-D | three-dimensional |
| $a$ | graphene lattice constant |
| $a_1, a_2$ | carbon nanotube lattice vectors |
| $a_{C\text{-}C}$ | nearest-neighbor carbon - carbon bond distance |
| AFM | atomic force microscope |
| ATPS | Aminopropyltriethoxysilane |
| b | integer |
| C | Carbon |
| $\boldsymbol{C_h}$ | chiral vector |
| CMC | cellulose (sodium carboxymethyl cellulose) |
| Co | Cobalt |
| COOH | carboxylic acid |
| CVD | chemical vapor deposition |
| D | SWNT bundle diameter |
| dc | direct current |
| DC | dip-coating |
| DCE | dichloroethane |
| DGU | density gradient ultracentrifugation |

| | |
|---|---|
| DI | deionized |
| $d_i$ | spacing between metal contact pad |
| DMAc | dimethyl acetamide |
| DMF | *N*,*N*-dimethylformamide |
| *DOS* | density of states |
| $d_t$ | carbon nanotube diameter |
| *E* | energy |
| *e* | electronic charge |
| ED | electrophoretic deposition |
| $E_F$ | Fermi level |
| $E_{Fi}$ | intrinsic Fermi level |
| *f(E)* | Fermi function |
| Fe | Iron |
| FM | vacuum filtration method |
| *G* | electrical conductance |
| H | Hydrogen |
| HiPCO | high pressure Carbon monoxide |
| $HNO_3$ | nitric acid |
| HOMO | highest occupied molecular orbital |
| HP | horsepower |
| IPA | isopropyl alcohol |
| IR | infrared |
| ITO | indium tin oxide |

| | |
|---|---|
| $J$ | current density |
| $k$ | wave vector |
| **K** | reciprocal lattice vector |
| $k_B$ | Boltzman constant |
| $L$ | length |
| $L_T$ | characteristic transfer length |
| M | energy transition between van Hove singularities in metallic SWNTs |
| $m$ | slope |
| MCE | mixed cellulose esters |
| $N$ | number of hexagons |
| $n$ | charge carrier density |
| $n,m$ | integer indices |
| Ni | Nickel |
| NMP | dimethyl pyrrolidone |
| O | Oxygen |
| OLED | organic light emitting diode |
| OPV | organic photovoltaic |
| $p$ | density of holes |
| PDMS | Polydimethylsiloxane |
| PECVD | plasma enhanced CVD |
| PEDOT:PSS | Poly(3,4-ethylenedioxythiophene) poly(styrenesulfonate) |
| PET | poly(ethylene terephthalate) |

| | |
|---|---|
| $P_{loss}$ | resistive power losses |
| Pr | probability |
| q | integer |
| $R$ | electrical resistance |
| $R_a$ | average surface roughness |
| $r_b$ | bending radius |
| $R_c$ | contact resistance |
| rf | radio frequency |
| rms | root mean square |
| $R_{path}$ | electrical resistance of SWNT network conducting pathway |
| $R_s$ | series resistance |
| $R_{sh}$ | sheet resistance |
| $R_{SWNT}$ | intratube SWNT resistance |
| $R_{SWNT\text{-}SWNT}$ | intertube SWNT resistance |
| S | energy transition between van Hove singularities in semiconducting SWNTs |
| s,p | electronic orbitals |
| SC | spray-coating |
| SDS | sodium dodecyl sulfate |
| $SOCl_2$ | thionyl chloride |
| sq | square |
| SWNT | single wall carbon nanotube |

| | |
|---|---|
| **T** | translation vector |
| $t$ | thickness |
| TLM | Transfer Length Method |
| UPS | Ultraviolet Photoelectron Spectroscopy |
| UV-Vis-NIR | ultraviolet-visible-near infrared |
| $V$ | voltage |
| $W$ | width |
| $x$ | number of conducting pathways in SWNT network |
| XPS | X-ray Photoelectron Spectroscopy |
| Y | Yttrium |
| $\gamma_0$ | nearest-neighbor transfer integral |
| $\theta$ | chiral angle |
| $\lambda$ | mean free path |
| $\lambda_{de}$ | de Broglie wavelength |
| $\mu$ | charge mobility |
| $\rho_c$ | specific contact resistance |
| $\sigma$ | electrical conductivity |
| $\Phi$ | work function |
| $\varphi_b$ | Schottky barrier |

# SUMMARY

Organic electronic devices are receiving growing interest because of their potential to employ lightweight, low-cost materials in a flexible architecture. These devices contain organic semiconductor materials that can be uniquely tuned to enable properties and performance which can be competitive with entrenched inorganic electronics, while facilitating other exciting niche applications. Organic electronic devices such as organic photovoltaics and organic light emitting diodes require the use of a transparent electrode to allow photons to enter or exit the devices efficiently and to simultaneously allow the extraction or injection of charge carriers. Typically, indium tin oxide (ITO) is utilized as the electrode due to its excellent transparency throughout the visible spectrum, its relatively low sheet resistance, and its work function, which is compatible with the injection and collection of charge carriers in organic semiconductors. However, ITO may ultimately hinder the full market integration of organic electronics due to its increasing cost, lack of mechanical flexibility, chemical instability, and sustainability pertaining to the environment and material utilization. Therefore, alternatives for ITO in organic electronics are being pursued.

Transparent electrodes comprised of single wall carbon nanotubes (SWNTs) are an appealing choice as a surrogate for ITO in organic electronics because of the extraordinary electrical and mechanical properties these 1-D structures possess, and the demonstrated potential of state of the art SWNT films. As such, the research presented in this dissertation has been conducted to advance the goal of manufacturing SWNT networks with transparent electrode properties that meet or exceed those of ITO.

Specifically, ultraviolet photoelectron spectroscopy was used to determine and present the first summarized report of the variation in work function of as-made, annealed, and chemically doped polydisperse SWNT films. This information was corroborated with x-ray photoelectron spectroscopy analysis, optical transmittance observations, electrical sheet resistance measurements, and a theoretical understanding of carbon nanotube electronic density of states to clearly elucidate the effect of unintentional and chemically induced doping on SWNT films. The insight gained from this information was used to provide evidence of possible spurious observations and conclusions in the present literature, and a simple optical solution was presented. While the doping effects were shown to be reversible in air and under moderate thermal loading, sustained electrical conductivity of heavily doped SWNT films was achieved via a thin conductive polymer "capping layer".

In order to fully realize the potential of SWNT networks as a transparent electrode, monodisperse networks that leverage the electronic homogeneity of the film were investigated and discussed. Chemically doped semiconducting SWNT films were found to have superior optoelectronic properties in comparison to similarly processed metallic SWNT films. Photoelectronic spectroscopy, electrical sheet resistance evaluation, and optical spectroscopy combined with a theoretical understanding of metallic and semiconducting SWNT were employed to clearly describe the impact of charge carrier doping on these films.

Finally, due to the potential demonstrated for SWNT films, electrical contact resistance to metallic grids that are often utilized in system level photovoltaic applications were investigated. The specific contact resistance of SWNT films in contact

with a metallic silver pad was found to be significantly higher than typical values obtained in silicon-based photovoltaic applications, thus resulting in non negligible power losses. This data represented the first reported measurement of specific contact resistance and thereby provided a forewarning to the SWNT research community of the potential impact on electrical power losses in organic photovoltaics.

In this dissertation, SWNT films were characterized with regard to the collective and individual properties of the SWNTs that comprise the network. The insight gained from evaluation of intrinsic SWNT properties was effectively leveraged to expand the present understanding of SWNT networks to facilitate future SWNT electrode development.

# CHAPTER 1: INTRODUCTION AND MOTIVATION

## 1.1. Background

Organic electronic devices are receiving growing interest because of their potential to employ lightweight, low-cost materials in a flexible architecture. These devices contain organic semiconductor materials that can be uniquely tuned to enable properties and performance which can be competitive with entrenched inorganic electronics, while facilitating other exciting niche applications. Organic light emitting diode (OLED) technology is the leading device platform for organic electronics since seminal work by Tang et al. [1] on small molecule OLEDs and Friend et al. [2] on polymer OLEDs. OLED development has recently reached commercialization status with Sony introducing a 3 mm thick, 11-inch television with a 178° viewing angle based on OLED technology [3]. OLEDs have also been successfully employed in solid state lighting applications with research yielding luminous efficacies of 102 lm/W [4] compared to approximately 15 lm/W and 60 lm/W for incandescent and compact fluorescent lighting respectively. Examples of applications that incorporate OLED technology are shown in Figure 1.1.

(a) (b)

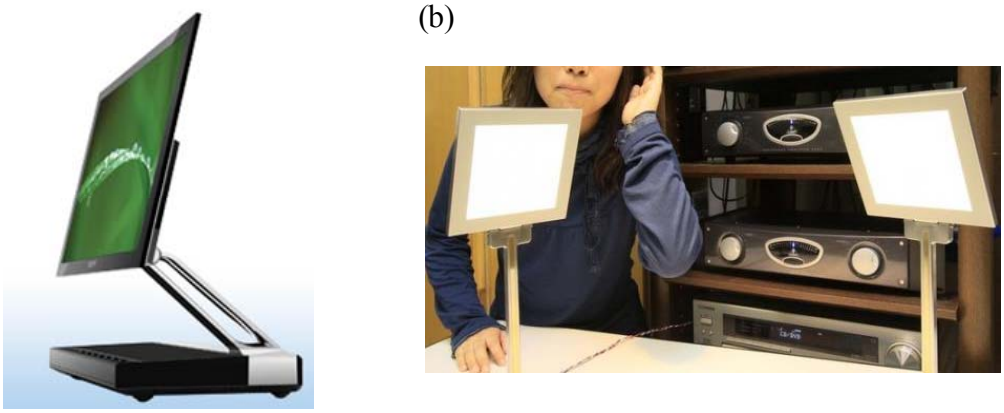

**Figure 1.1.** (a) Sony OLED TV (*http://www.sonystyle.com*)**.** (b) Kenwood OLED speakers (*http://www.gadgetvenue.com/kenwood-oled-speakers-04282414/*)

Organic photovoltaics (OPVs) have recently received significant attention based largely on their capability to enable low-cost, solar-powered technologies with flexible form factors [5]. In 2007, the market value for photovoltaics exceeded $10 billion with a yearly growth rate of 30-40% [6]. Because OPVs operate in reverse principle to OLEDs, some of the fundamental understanding achieved in OLED research can readily be leveraged in OPV advancement. Therefore, OPVs will continue to benefit from the successful development of OLED technology. Similar to OLEDs, OPVs can be fabricated via evaporation or solution processing of small molecules and/or polymer blends. Currently, the best laboratory power efficiencies (i.e. efficiency of light conversion to electricity) achieved are in the 5-6% range with future achievable goals of 10-15% [6].

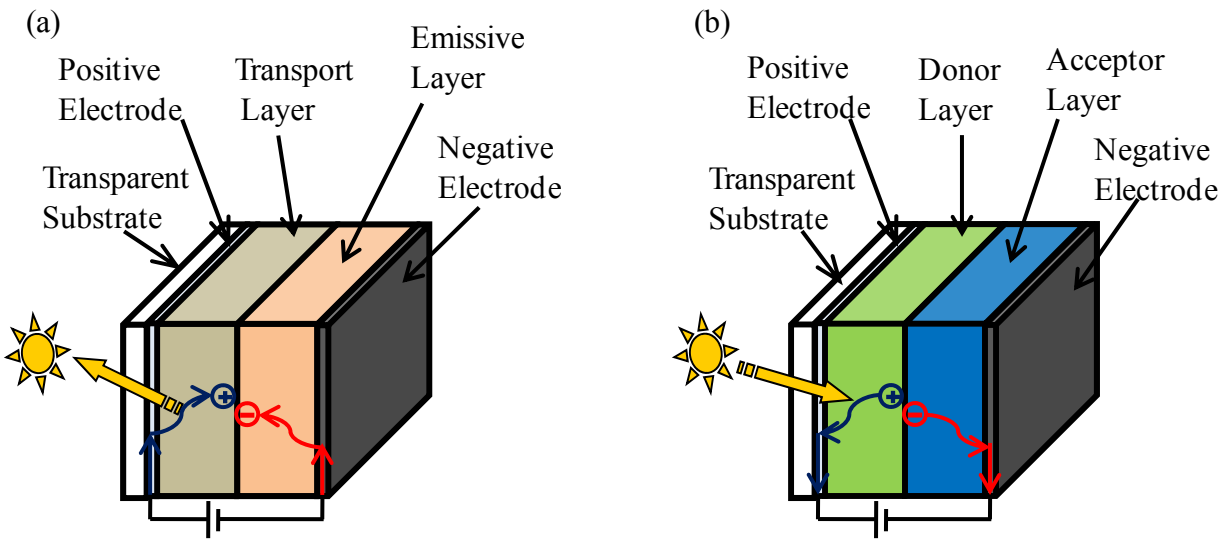


**Figure 1.2.** (a) Schematic architecture of typical OLED (b) Schematic architecture of typical OPV.

Sample OLED and OPV architectures are shown in Figure 1.2. OLED devices contain active layers consisting of a transport and emissive layer bounded by positive and negative electrodes. When a voltage is applied across the electrodes, holes are injected into the transport layer via the positive electrode, while electrons are injected into the emissive layer by the negative electrode. Electrons and holes then drift to the interface of the active layers and combine to generate light, which is emitted through the transparent positive electrode and substrate as illustrated in Figure 1.2a. OPVs operate in a reverse manner as demonstrated in Figure 1.2b. Light is transmitted through the transparent substrate and positive electrode where it is absorbed by the organic donor layer, resulting in the generation of an electron and hole pair. The resultant electron-hole pair, defined as an exciton, is coulombically bound as it drifts to the interface of the donor and acceptor layers. If the acceptor layer is appropriately selected, it is energetically favorable for the exciton to separate at this interface such that the electron is transferred to the acceptor

layer, while the hole remains in the donor layer. The charges subsequently diffuse to the electrodes where they are extracted for power output.

As described, both of these devices require the use of a transparent positive electrode to allow light to enter or exit the devices efficiently and to simultaneously allow the extraction or injection of charge carriers. Therefore, the selection of an acceptable transparent electrode is paramount to optimal device performance. Electrodes with poor electrical conductivities contribute to high device series resistance, $R_s$, with resistive power losses, $P_{loss}$, defined as

$$P_{loss} = I^2 R_s \tag{1.1}$$

where $I$ is the current of the device. Electrodes provide optimal hole injection or extraction when the work function is as close as possible to the highest occupied molecular orbital (HOMO) of the adjacent organic layer. Differences in the work function and HOMO energy level result in the formation of an energy barrier that holes must overcome which in turn, further contributes to increase $R_s$ [7]. Specifically, a work function that exceeds the energy of the HOMO will result in a hole collection barrier in OPVs, whereas a work function less than the energy of the HOMO will result in a hole injection barrier in OLEDs. Because organic device layers are typically less than 200 nm in thickness, an electrode must be sufficiently smooth in order to minimize current leakage in the device [8]. Furthermore, the electrode must be as transparent as possible to limit optical losses.

At present, tin doped indium oxide, (ITO) deposited on glass substrates is utilized as the positive electrode in standard organic devices, due to its unique ability to reasonably meet the aforementioned performance criteria. ITO can be rf-sputtered onto transparent substrates followed by annealing at elevated temperatures to provide a crystalline structure with a sheet resistance, $R_{sh,}$ of less than 10 Ω-sq$^{-1}$ and corresponding average transmission in the visible spectrum exceeding 90% [9]. ITO is a degenerately n-doped semiconductor with a work function between ca. 4.3 - 4.7 eV, as reported in the literature [7, 10]. However, ITO can be surface treated to increase the work function to become more compatible with the HOMO level of many organic semiconductor layers, thereby reducing the energy barrier to charge injection [11]. In addition, ITO has a smooth surface with measured root mean square (rms) roughness values less than 2 nm [8].

While ITO may be the present solution for organic electronics with seemingly appropriate material properties for device incorporation, it is accompanied by significant challenges that may ultimately hinder the full market integration of OLED and OPV devices. High conductivity ITO requires annealing at high temperatures (> 200 °C) to achieve crystallinity [12]. However, polymer substrates desired for flexible organic electronics cannot undergo such elevated temperatures. Thus ITO deposited on flexible polymer substrates remain amorphous in structure and have considerably higher $R_{sh}$ (ca. 60 - 300 Ω-sq$^{-1}$ [13]) than ITO deposited and subsequently annealed on glass. ITO is also used in liquid crystal displays and plasma screens, which have both experienced substantial demand increases in recent years. Therefore, as recently published in Nature,[14] the price per kilogram of indium, the primary constituent of ITO, has

increased from $100 in 2002 to $1,000 in 2005 with prices still around $700 in 2007. In addition, because ITO is an oxide material, it suffers from a lack of mechanical flexibility. Typical fracture strains are as low as 1.5% which result in catastrophic loss of electrical conductivity in flexible applications [15]. ITO also suffers from a lack of surface composition homogeneity and overall environmental instability [16]. Since the work function of a material is highly sensitive to the state of the surface, the work function of ITO can vary with its environmental conditions [11]. This instability is exacerbated in circumstances that require surface treatment to increase the work function for better organic semiconductor layer compatibility [10]. Also, surface treatment of ITO can result in increased film sheet resistance due to absorption of oxygen in the film [17]. Moreover, most ITO films are deposited via a sputtering process. Sputtering processes are especially inefficient [18] and only a small percentage of the sputtered material makes contact with the substrate. Because the cost of recycling is considerably high, little is recycled, thereby resulting in significant material underutilization. Therefore, alternatives for ITO in organic electronics are being pursued. These include other transparent conducting oxides [19], conducting polymers [20, 21], polymer-carbon nanotube composites [22, 23], and two-dimensional random network single wall carbon nanotube (SWNT) films [24-27].

Other transparent conducting oxides may ultimately experience similar electrical and mechanical instability issues that affect ITO, while conducting polymers and polymer composites suffer from insufficient optoelectronic properties. Recent polymer based electrodes demonstrated electrical sheet resistance values of 400 – 2,000 $\Omega$-sq$^{-1}$ for PEDOT:PSS films [20, 28] and 250 $\Omega$-sq$^{-1}$ for PEDOT:PSS-carbon nanotube composites

[23] in comparison to 10 Ω-sq$^{-1}$ for ITO. Electrodes comprised of SWNTs are an appealing choice as a surrogate for ITO in organic electronics because of the extraordinary electrical and mechanical properties these 1-D structures possess. Exploiting the metallic behavior of SWNTs is desired because individual SWNTs can support electrical current densities exceeding $10^9$A-cm$^{-2}$ [29] while SWNT ropes and bundles of individual SWNTs have demonstrated axial conductivity values as high as 10,000 - 30,000 S-cm$^{-1}$ [30]. In addition to significant electronic potential, SWNT electrodes have been shown to exhibit sustained electrical performance under extreme bending conditions [31]. The higher work function of SWNTs (ca. 5.0 eV) [32] in comparison with ITO (ca. 4.3 - 4.7 eV) may provide a more optimal hole injection into typical OLED hole transport layers due to the reduced energy barrier arising from the difference of the organic HOMO level and the positive electrode work function [11]. Additionally, a larger selection of organic materials compatible with the high work function of SWNTs may also be available. Moreover, SWNT films can be processed at room temperature under ambient conditions. While the potential is great, full realization of the optoelectronic properties of individual SWNTs integrated into a random network has yet to be achieved.

### 1.2. Goals of the Research

Given the potential of SWNT networks, this research will seek to advance the goal of manufacturing SWNT films with transparent electrode properties that meet or exceed those of ITO. To this end, methods to enhance the optoelectronic properties of SWNT films fabricated in a manner consistent with state of the art processing techniques

will be investigated. In addition, SWNT films will be characterized from the perspective of the collective and individual properties of the SWNTs that comprise the network. Insight gained from the evaluation of intrinsic SWNT properties will be subsequently leveraged to expand the current understanding of SWNT networks and thereby suggest the best route to successful electrode integration for organic electronics.

The dissertation format will be as follows. Chapter 2 will give background information and theory necessary for chapters 3-6, in addition to presenting the state of the art in SWNT films. Chapter 3 will summarize the baseline properties of the SWNT films used in this study with regard to salient figures of merits. Chapters 4-6 will demonstrate a clear contribution to the advancement of SWNT films as a transparent electrode. In particular:

- Chapter 4 will characterize the optoelectronic behavior of SWNT films via corroborative theoretical and experimental observations to expand the understanding of how SWNT electrode properties are enhanced and sustained through chemical treatment and subsequent processing. This chapter will focus on SWNT films of heterogeneous electronic type (i.e. metallic and semiconducting SWNTs present in film).
- Chapter 5 will present an investigation of SWNT films of homogeneous electronic type (i.e. only metallic or only semiconducting SWNTs present in film). The impact of using SWNT films of homogeneous electronic type will be discussed with regard to how the fundamental electronic properties of SWNTs can be leveraged to understand network performance.

- Chapter 6 will give the first report of the electrical nature of the interfacial contact between thin SWNT films and metallic contacts. Elucidation of its impact on device power loss will also be presented.

# CHAPTER 2: RELEVANT SWNT THEORY AND SWNT FILM BACKGROUND

## 2.1. Introduction

Originally discovered as a by-product of carbon fullerene research [33], carbon nanotubes have received prodigious amounts of research interest since 1991. Researchers have sought to employ the one dimensional nanoscale properties of SWNTs in applications that range from space elevators [34] and batteries [35] to cancer treatment [36] and chemical sensors [37]. This dissertation seeks to advance the goal of realizing the potential of single wall carbon nanotubes in random networks as a transparent electrode replacement for ITO, in which chapters 3 – 6 will present the research contribution to this end. However, to first provide a knowledge framework for subsequent discussion and theoretical leverage, this chapter will give pertinent background information on the properties of individual SWNTs with regard to their application as a thin film network for transparent electrodes. This chapter will also present a literature review of state of the art in the fabrication of SWNT films to demonstrate the current viability of nanotube networks as a transparent electrode and to serve as a basis for the scientific contribution made in this dissertation.

## 2.2. Carbon Nanotube Structure

As first described by S. Iijima [38], carbon nanotubes are "helical microtubules of graphitic carbon". Single wall carbon nanotubes refer to cylinders of graphene with diameters on the order of nanometers that can have wrap angles from 0 – 30°. As shown

in Figure 2.1, a chiral vector, $\boldsymbol{C_h}$, can be used to uniquely identify each possible wrap angle. $\boldsymbol{C_h}$ is defined as a linear combination of the graphene lattice vectors, $a_1$ and $a_2$:

$$\vec{C}_h = \vec{n}a_1 + \vec{m}a_2 \equiv (n,m) \tag{2.1}$$

where $n$ and $m$ are integers ($n \geq m$) [39] that are used as indices to describe $\boldsymbol{C_h}$. Physically, $\boldsymbol{C_h}$ connects two equivalent sites on the original graphene crystal lattice, $A$ and $A'$, such that the cylindrical nanotube is formed by connecting the two points together with the cylinder joint made along the lines perpendicular to $\boldsymbol{C_h}$ [39]. The chiral angle, $\theta$, is defined as the angle between $a_1$ and $C_h$ and is equal to

$$\theta = \tan^{-1}\left(\frac{\sqrt{3}m}{2n+m}\right) \tag{2.2}$$

The range of $\theta$ is $0 \leq |\theta| \leq 30$. SWNTs with indices of ($n$,0) ($\theta = 0°$) are described as zigzag tubes, because of their zigzag pattern along the circumference. SWNTs with indices of ($n$,$n$) ($\theta = \pm 30°$) are described as armchair tubes because of their armchair pattern along the circumference [40]. All other tubes (n,m) are classified as chiral. An example of a zigzag, armchair, and chiral SWNT are shown in Figure 2.2.

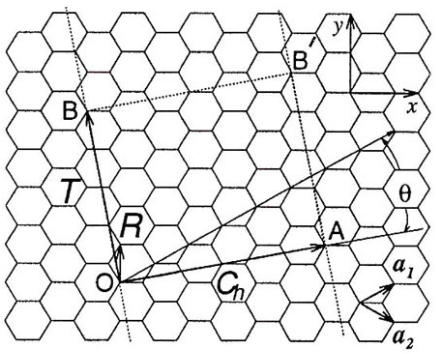


**Figure 2.1.** Graphene honeycomb network with lattice vectors $a_1$ and $a_2$. The chiral vector, $\mathbf{C_h}$, with (n,m) = (4,2), represents a possible wrapping of the two-dimensional graphene sheet into a tubular form. The translation vector, **T**, of the nanotube is also shown. Adapted from reference [41].

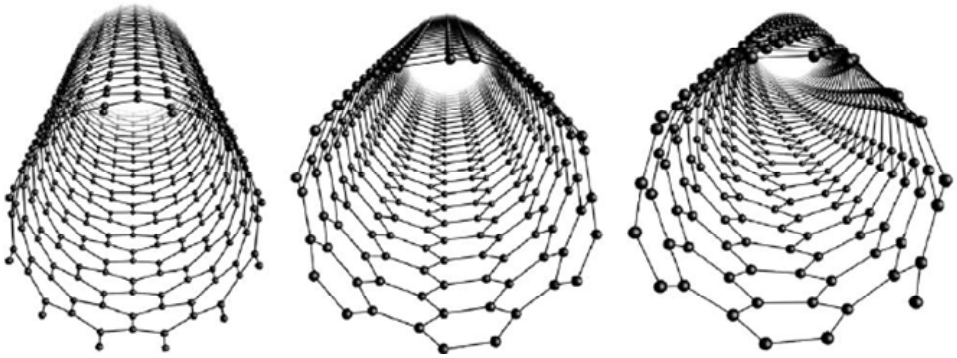

(12,0) (6,6) (6,4)

**Figure 2.2.** Atomic structures of (12,0) zigzag, (6,6) armchair and (6,4) chiral nanotubes. Taken from reference [40].

Since $\boldsymbol{C_h}$ defines the circumference of the nanotube, the diameter, $d_t$, can be estimated from

$$d_t = \frac{|C_h|}{\pi} = \frac{a}{\pi}\sqrt{n^2 + nm + m^2} \tag{2.3}$$

where the lattice constant, *a,* is given by

$$a = \sqrt{3}a_{C-C} = \sqrt{3} \times 0.142 \text{ nm} = 0.246 \text{ nm} \tag{2.4}$$

and $a_{C\text{-}C}$, is the nearest-neighbor C-C bond distance.

### 2.3. Electronic Properties of SWNTs

As cylindrical tubes of graphene, the electronic nature of SWNTs can be best discussed with reference to planar graphene sheets. Specifically, the electronic properties can be developed by imposing a periodic boundary condition in the circumferential direction of nanotubes on the energy dispersion relations for 2-D graphene. The details of this process are summarized in the discussion to follow.

Graphene is a planar, one-atom thick sheet of carbon atoms in a hexagonal arrangement similar to a sheet of chicken wire (Figure 2.1). Each carbon atom has four valence electrons with the electronic structure $(2s)^2$ $(2p)^2$. Three of the four valence electrons in each carbon atom are hybridized to $sp^2$ orbitals that form strong covalent bonds with the three neighboring carbon atoms [42]. The remaining valence electron in the $p_z$, or $\pi$, orbital provides the electron band network that is largely responsible for charge transport in graphene [43]. Detailed electronic band structure calculations for graphene were first carried by P.R. Wallace [44]. The two dimensional energy, $E_{2D}$, of an electron in graphene defined by wave vectors $k_x$ and $k_y$ was determined to be:

$$E_{2D}(k_x, k_y) = \pm\gamma_0 \left\{ 1 + 4\cos\left(\frac{\sqrt{3}k_x a}{2}\right)\cos\left(\frac{k_y a}{2}\right) + 4\cos^2\left(\frac{k_y a}{2}\right) \right\}^{\frac{1}{2}} \qquad (2.5)$$

where $\gamma_0$ is the nearest-neighbor transfer integral. The resulting electronic band structure for graphene is shown in Figure 2.3. The Fermi energy is located at 0 eV, which is also where the π and $\pi^*$ bands meet at the high symmetry K point of the Brillouin Zone. π and $\pi^*$ bands represent bonding orbitals in the valence band and antibonding orbitals in the conduction band, respectively. The significance of the Fermi energy is that it is the highest energy level of an electron at a temperature of absolute zero. Graphene is considered to be a "zero-gap" semiconductor [45], since there is no overlap in the conduction and valence bands at the Fermi energy. However, because there is also no energy bandgap as in traditional semiconductors, electrons at the Fermi energy can be easily elevated to the $\pi^*$ band, thereby allowing graphene to exhibit high conductivity at room temperature.

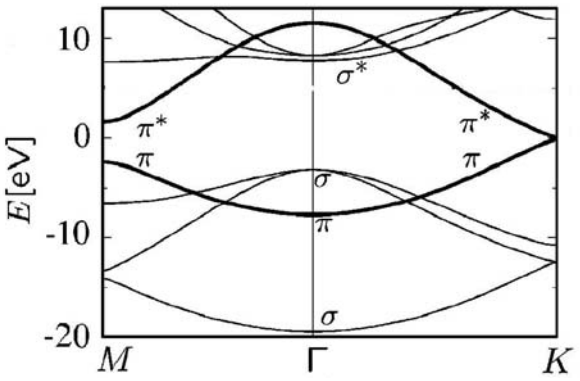


**Figure 2.3.** Electronic band structure of graphene. The π and $\pi^*$ bands meet at the K points of the Brillouin zone. Adapted from reference [40].

When a graphene sheet is in the cylindrical form of a carbon nanotube, a periodic boundary condition can be imposed in the circumferential direction defined by the $\boldsymbol{C_h}$ such that:

$$\vec{C}_h \bullet \vec{k} = 2\pi \mathrm{b} \tag{2.6}$$

where b is an integer [39]. Now, instead of a continuous distribution of available $k$ wave vectors, only a discrete set are allowed in that direction that satisfy $n\lambda_{de} = \pi d_t$, where $\lambda$ is the de Broglie wavelength [41]. The $k$ wave vectors in the direction of the nanotube axis remain continuous. The new resulting set of $k$ wave vectors can then be used with Eq. (2.5) to generate the 1-D energy dispersion relations for carbon nanotubes such that [46]:

$$E_\mu(k) = E_{2D}\left( k\frac{\mathbf{K_2}}{|\mathbf{K_2}|} + \mu\mathbf{K_1} \right) \tag{2.7}$$

where $\mathbf{K_1}$ and $\mathbf{K_2}$ are reciprocal lattice vectors that correspond to the translation vector, $\mathbf{T}$, and $\boldsymbol{C_h}$, from the unit cell in real space (Figure 2.2). $\mu$ is an integer (1,2...,$N$) where $N$ is the number of hexagons of the graphene honeycomb lattice in the nanotube unit cell. $N$ also describes the number of discrete wave vectors allowed from Eq. (2.6) and consequently the number of pairs of energy dispersion curves for each SWNT that results from Eq. (2.7). The electronic band structures for selected SWNTs are shown in Figure 2.4 [42]. In particular, an armchair (i.e. ($n$,$n$)) and two zigzag (i.e. ($n$,0)) SWNTs are

shown in Figures 2.4a and 2.4b,c respectively . The energy dispersion curves for the three SWNTs differ significantly at the Fermi energy. A conduction $\pi^*$ band and valence $\pi$ band cross the Fermi energy in the armchair (5,5) SWNT such that metallic behavior is possible. SWNTs with similar energy dispersion relations are described electronically as metallic SWNTs. Because all other armchair SWNTs have similar energy bands that cross at the Fermi energy, all armchair SWNTs are likewise described as metallic. The zigzag (9,0) SWNT has dispersion curves at the Fermi energy that are similar to the curves observed in graphene where a valence and conduction energy band meet instead of cross at the Fermi energy, thus yielding a energy bandgap, $E_g$, equal to zero. Akin to graphene, only a negligible amount of energy is needed to promote electrons from the valence band to the higher energy conduction band, thus permitting SWNTs with such energy dispersion relations to also be classified as metallic. In contrast, a significant gap exists between the conduction and valence bands in the zigzag (10,0) SWNT, such that these nanotubes are defined as semiconducting. As the diameter of the nanotube increases, the periodic boundary conditions applied in Eq. (2.6) allow more wave vectors in the circumferential direction. Also, since $E_g \sim 1/d_t$ [41], $E_g$ disappears with increasing diameter to the limit of $d_t \rightarrow \infty$, which yields the "zero-gap" semiconducting behavior of graphene [39].

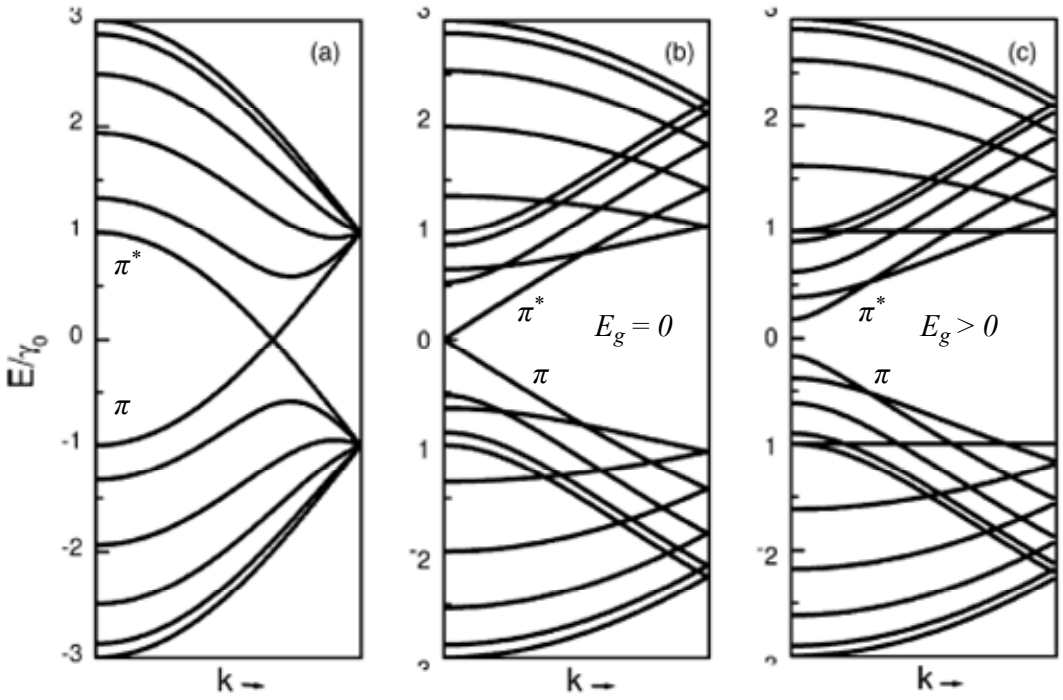


**Figure 2.4.** Electronic band structure of carbon nanotubes (a) (5, 5), (b) (9, 0) and (c) (10, 0) derived by zone-folding of the band structure of the graphene sheet. $\gamma_0 = 2.9$ eV. Adapted from reference [42].

By substituting the wave vector at the Fermi energy of graphene into the periodic boundary condition in Eq. (2.6), the particular SWNT chiral vectors, $\boldsymbol{C_h}$, that will result in wave vectors that include the Fermi energy can be determined. Saito et al. [39] found the (n,m) indices of $\boldsymbol{C_h}$ to be metallic (i.e. allowed wave vectors include the Fermi energy) if the following relationship is true:

$$2n + m = 3q \tag{2.8}$$

where $q$ is an integer. All other SWNTs are semiconducting. Under a uniform distribution of $\boldsymbol{C_h}$ vectors, 1/3 of the nanotubes are metallic and 2/3 semiconducting.

The density of states (*DOS*) represents the number of available states for a given energy level and is important in determining the electrical conductivity of a material. The *DOS* can be determined from the energy dispersion relations, *E(k)*, by [46]:

$$DOS(E) = \frac{2}{N}\sum_{\mu=1}^{N}\int \frac{1}{\left|\frac{dE_\mu(k)}{dk}\right|}\delta\left(E_\mu(k) - E\right)dE \tag{2.9}$$

It is known that *DOS* is affected significantly by geometry. Dimensional confinement results in considerable departure from the 3D characteristic parabolic relationship of *DOS* to energy $\left(\text{i.e. } DOS \sim \sqrt{|E|}\right)$ near band extrema [40]. In 1-D materials, *DOS* scales with the inverse of the square root of the absolute value of $E$ $\left(\text{i.e. } DOS \sim 1/\sqrt{|E|}\right)$ [47]. Figure 2.5 illustrates this distinction.

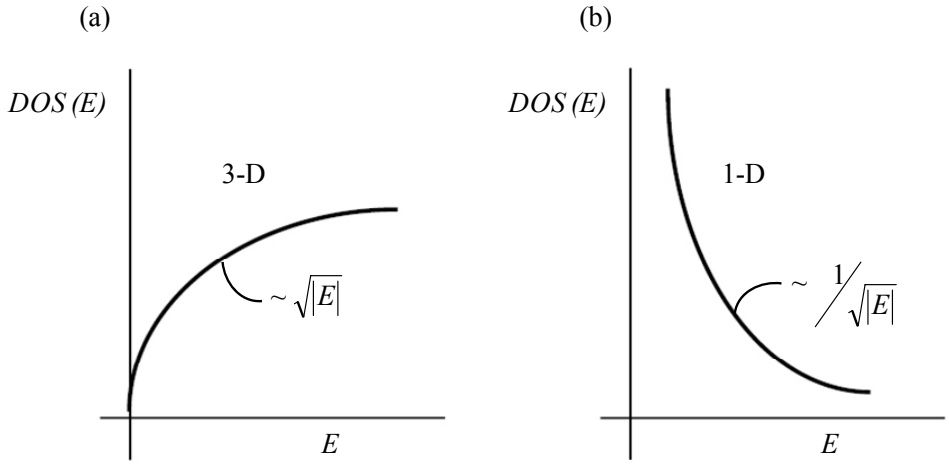


**Figure 2.5.** Density of states behavior close to a band extrema of *E(k)* in (a) three dimensions and (b) one dimension. Adapted from reference [47].

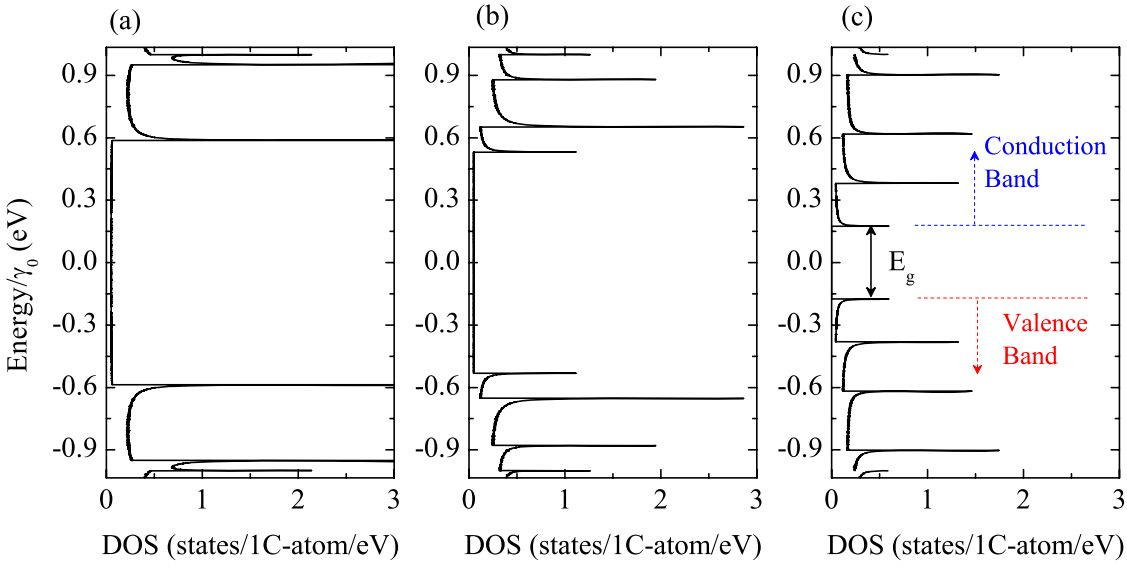


**Figure 2.6.** DOS versus energy for (a) (5,5), (b) (9,0) and (c) (10,0) SWNT derived by zone-folding of the band structure of the graphene sheet. Fermi energy located at 0 eV. Plots created with data from reference [48].

Figure 2.6 shows the *DOS(E)* plots for a (5,5), (9,0), and (10,0) SWNTs. The energy dispersions for these SWNTs were plotted in Figure 2.4. Band extrema from the dispersion relations are manifested as "spikes" in the *DOS* and defined as van Hove singularities [49]. Mirror image spikes exist above and below the Fermi energy. The origin of the van Hove singularities is clear from Eq. (2.9). As the energy dispersion relation for each band becomes flat, *DOS* will be very large (i.e. "spikes" in the *DOS* plot) [46]. Comparison of the energy location of band extremas in Figure 2.4 and the energy location of the van Hove singularities in Figure 2.6 is consistent with this understanding of *DOS* and *E(k)*. The one dimensional nature of SWNTs is also evident as *DOS* diverges from van Hove singularities with the inverse of the square root of the absolute value of *E*.

The *DOS* plots in Figure 2.6 provide further perspective for understanding the electronic properties of carbon nanotubes. As suggested by Saito et al. [39] and discussed earlier, the (5,5) and (9,0) SWNTs are metallic electronically. Therefore, available states must exist at the Fermi energy for electronic charge occupation and subsequent conduction. This is indeed the case for the metallic SWNTs in Figures 2.6a and 2.6b. In contrast, there is an energy gap of ca. 1 eV between mirror van Hove singularities where there are no electronic states in the (10,0) SWNT. A clear distinction can thus be made between the valence and conduction bands in this semiconducting SWNT. The magnitude of the energy gap in semiconducting SWNTs is found by [50]:

$$E_g = \frac{2a_{C-C}\gamma_0}{d_t} \tag{2.10}$$

As shown in Figure 2.4, a symmetric unoccupied $\pi^*$ energy band exists for every occupied $\pi$ energy band. Therefore, wave vector conservation would imply that the strongest optical transitions would occur between symmetric $\pi$- $\pi^*$ energy bands which share a common wave vector, **k** [40]. Because of the high density of electronic states present at van Hove singularities, the energy transitions ($E_{ii}$) between mirror "spikes" dominate optical spectra (i.e. high optical absorption will occur at photon energies equal to $E_{ii}$). Example $E_{ii}$ are illustrated in Figure 2.7 for the metallic (9,0) SWNT and semiconducting (10,0) SWNT. For semiconducting SWNTs, $E_{ii}$, is referenced as a $S_{ii}$, and $M_{ii}$ for metallic SWNTs. Based on the work of Kataura et al. [49], Saito et al. [46] plotted energy transitions versus $d_t$, as shown in Figure 2.8.

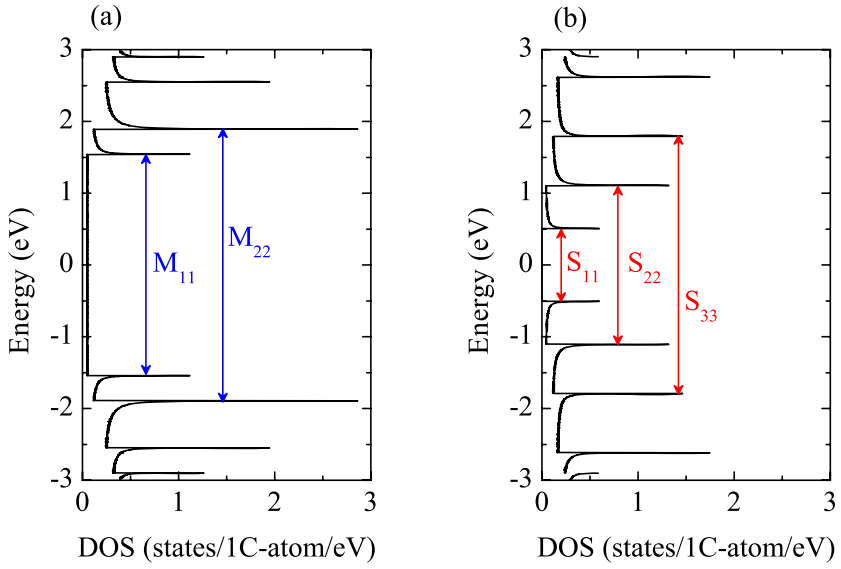


**Figure 2.7.** DOS versus energy for (a) (9,0) and (b) (10,0) SWNT, derived by zone-folding of the band structure of the graphene sheet. Fermi energy located at 0 eV. Plots created with data from reference [48].

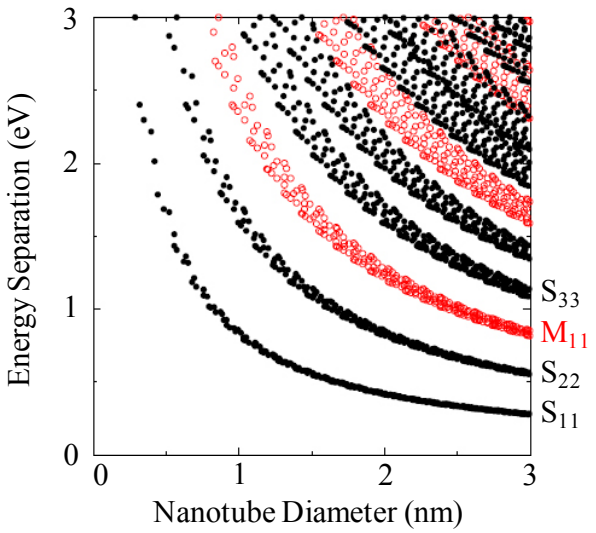


**Figure 2.8.** Reproduced Kataura plot of energy separation of van Hove singularities in carbon nanotubes versus nanotube diameter [48]. Black points are semiconducting nanotubes while red points are metallic nanotubes. The energy separation of van Hove singularities for the $S_{11}$, $S_{22}$, $M_{11}$, and $S_{33}$ energy transitions are denoted.

It must be noted that the zone folding approximation used to determine the electronic properties of SWNTs with reference to graphene did not consider the effects of nanotube curvature. The diameter was only considered to determine a finite circumferential length used to impose periodic boundary conditions on the allowed wave vectors. However, because the carbon atoms are located on a cylindrical wall in SWNTs, the C-C bonds perpendicular and parallel to the axis are slightly different, thus the conditions that defined the K point of graphene are modified due to tube curvature. As a result, the K point is no longer the location of the Fermi energy [40, 51]. Therefore, a small bandgap ($E_{g*}$) is induced in chiral metallic SWNTs that scales with $1/d_t^2$, in contrast to the bandgap in semiconducting SWNTs ($E_g$) that scales with $1/d_t$ [Eq.

(2.10)]. Owing to the wrap angle of metallic armchair SWNTs, there is no curvature induced band gap. In Figure 2.9 the predicted curvature induced energy bandgaps are plotted as a function of nanotube diameter [52]. However, as can be seen in the figure, the scale of $E_{g^*}$ is more than an order of magnitude smaller than the semiconducting bandgap. For nanotubes greater than 10 Å, $E_{g^*}$ is smaller than $k_BT$ at room temperature ($\approx$ 0.03 eV) such that the effects of $E_{g^*}$ are negligible.

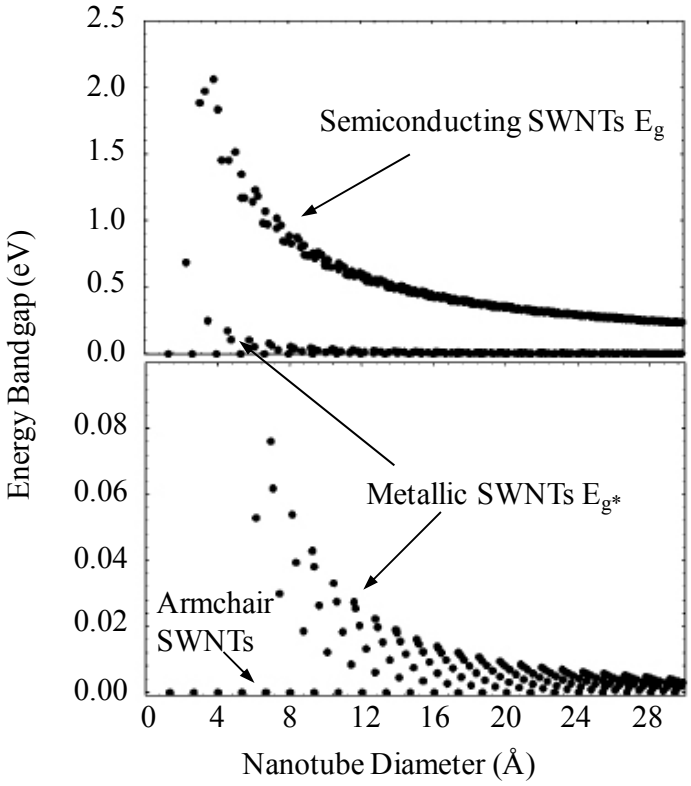


**Figure 2.9.** SWNTs energy bandgaps as a function of tube diameter. Three distinct behaviors are exhibited: semiconducting SWNT bandgaps that scale with $1/d_t$ (top panel, top curve), metallic SWNT bandgaps that scale with $1/d_t^2$ (top panel, lower curve, and shown in the expanded scale in lower panel), and armchair SWNTs with zero energy bandgaps. Adapted from reference [52].

## 2.4. SWNT Synthesis

The three primary methods of SWNT synthesis are arc-discharge, laser-ablation, and chemical vapor deposition (CVD). These techniques have been used since 1991 to produce carbon nanotubes. The details of which are described below.

### 2.3.1. Arc-discharge

First developed by Iijima in 1991 [33], arc-discharge has been described as the easiest and most common method to produce carbon nanotubes [53]. A schematic of this method is shown in Figure 2.10. While both electrodes are graphitic, the anode contains small amounts of transition metals such as Fe, Co, Ni, or Y to facilitate the production of single wall carbon nanotubes. In this method, SWNTs are deposited on the cathode as the anode is vaporized due to a high temperature (> 3000 °C) plasma induced by the arc-discharge between the two electrodes [42]. During processing, a direct current (dc) of 50 - 100A is passed between the anode and cathode at a separation distance of less than 1 mm.

The material deposited on the cathode has a yield of 70 – 90% SWNTs [42]. Accompanying SWNTs are amorphous carbon, graphitic nanoparticles, and metal catalysts that must be removed in future purification processes. The mean diameter of tubes is 1.4 nm [54] with lengths up to several microns [47]. The quantity and quality of SWNTs produced depends primarily on the transition metal / carbon mixture in the anode [47].

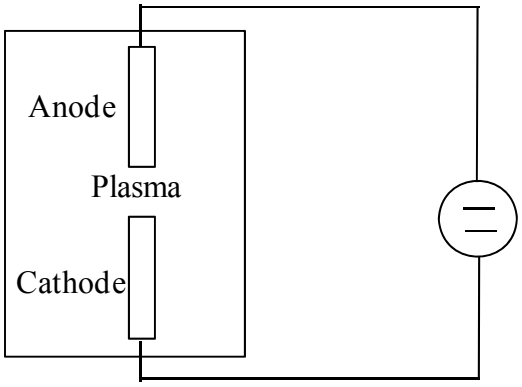


**Figure 2.10.** Schematic of arc-discharge scheme. Adapted from reference [42].

### 2.3.2. Laser-ablation

First developed by Guo et al. [55]. laser ablation involves the vaporization of target located inside a heated tube furnace at ~1200°C with continuous flow of inert gas. The target consists of a mixture of graphite and metal catalyst (Co, Ni) [56]. A schematic of the process is shown in Figure 2.11. The nanotubes nucleate in the vapor phase, coalesce, and condense downstream of the furnace [47]. As such, this method is similar to arc-discharge production of SWNTs in that both processes consist of sublimating a mixture of graphite and metals in a reduced atmosphere [47]. The yield and size of SWNTs produced by laser ablation is also similar to those obtained by arc-discharge (i.e. > 70% purity, mean diameter of 1.3 nm). Two primary drawbacks of both methods are (1) the reliance of the process on the evaporation of carbon atoms from solid graphite targets at temperatures >3000 °C and (2) the resulting SWNTs are tangled which makes subsequent purification processing difficult [42]. In addition it is more expensive to produce SWNTs by laser ablation in comparison to arc-discharge due to the laser and large amount of power necessary [47].

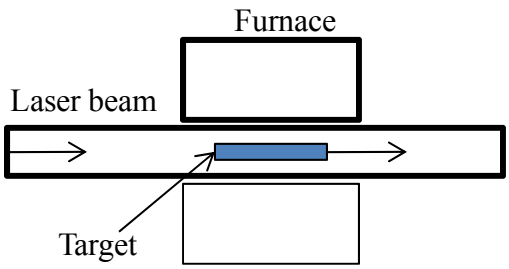


**Figure 2.11.** Schematic of laser-ablation scheme. Adapted from reference [42].

### 2.3.3. CVD

First employed in the production of nanotubes by Yacaman et al. in 1993 [57], the CVD technique consists of the decomposition of hydrocarbons at moderately high temperatures (i.e. 750 – 1000 °C) [42, 47, 58]. Typical hydrocarbons include ethylene [59], methane [58, 60, 61], or carbon monoxide [61]. A schematic of the process is shown in Figure 2.12. As the hydrocarbons enter the furnace and decompose, carbon is absorbed by the nanoscale size metal catalyst and subsequently precipitates to form nanotubes [53]. The metal catalysts are transition metals in which carbon has a high solubility such as iron, nickel or cobalt.

In contrast to methods that require the sublimation of carbon that result in highly entangled ropes of SWNTs, ca. 90% of the nanotubes produced from CVD are individual SWNTs [60]. Also, nanoscale positional control and SWNT alignment can be achieved using CVD [58]. The diameter of SWNTs produced from this method is closely determined by the diameters of the catalytic particles [58]. Therefore, the range of reported SWNTs diameters is 0.7 nm to 5 nm [42, 58]. With typical lengths in the range of 50 – 250 μm, SWNTs produced via CVD are considerably longer than arc-discharge and laser ablation. Zheng et al. [62] obtained a CVD fabricated SWNT of 4 cm long.

Also, SWNTs fabricated via CVD can be directly grown on a desired substrate, in contrast to arc-discharge and laser ablation methods that require the collection of vapor produced SWNTs that condense to form a carbon "soot" of entangled nanotubes.

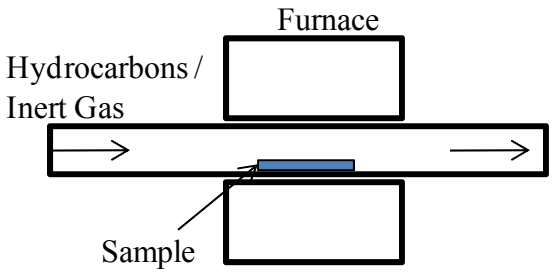


**Figure 2.12.** Schematic of CVD scheme. Adapted from reference [42].

## 2.5. SWNT Film Electrodes

The architecture of a typical SWNT film is shown in Figure 2.13. In this arrangement SWNTs are randomly distributed in a 2-D array. Because of the 1-D nature of SWNTs, they can be modeled as electronic "conducting sticks" [63]. Due to the nature of SWNT batch synthesis, 2/3 of the SWNTs in the network are semiconducting, with the remaining 1/3 being metallic in electronic behavior. Electrical charges are conducted across the film by traveling along conducting paths similar to the path illustrated in **bold color** in the figure. In this construction, both the SWNT intertube resistance and the intratube resistance are important in determining the overall film conductivity.

The random network arrangement of SWNT films permits statistical averaging to compensate for electrical anisotropy in the film, particularly with regard to varying electronic type (i.e. metallic and semiconducting). With sufficient SWNT coverage,

nanotube networks can be fabricated that exhibit metallic behavior in spite of the fact that 2/3 of the network are semiconducting [64]. The converse is true for low density networks. The metallic SWNTs in low density films are not sufficiently numerous to form pure metallic pathways in the film [64]. The random architecture also provides mechanical stability to the network. In this regard, the film can maintain electrical contact points even under extreme bending [24, 65], as nanotubes pivot at intertube junctions throughout the film.

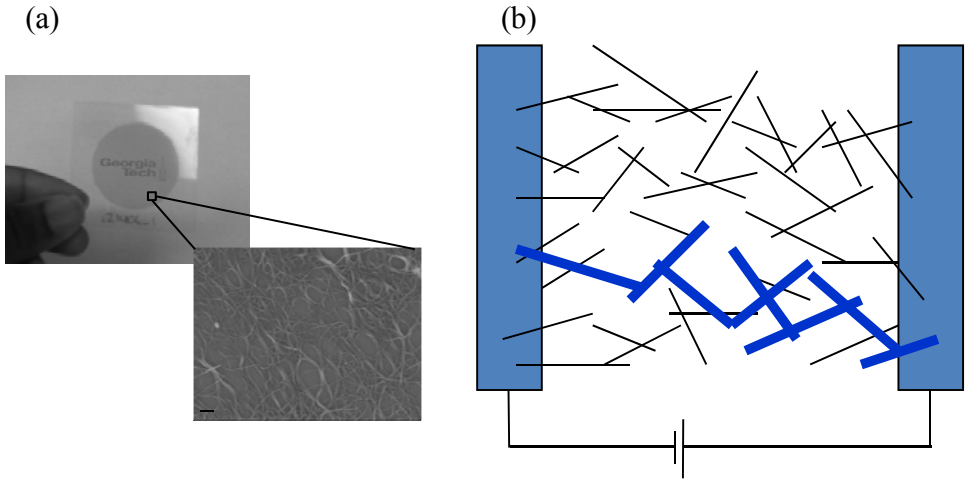


**Figure 2.13.** (a) Upper image: Photograph of SWNT electrode on plastic substrate. Lower image: SEM image of SWNT network. Scale bar = 100 nm. (b) Schematic of SWNT film architecture. Possible conduction pathway is illustrated in **bold.**

Numerous techniques for the deposition of thin film SWNT networks onto transparent substrates have been demonstrated. Primarily these can be classified in 2 categories: (1) direct CVD growth to desired substrate [66] or CVD growth and subsequent transfer to desired substrate [67, 68] and (2) solution processed SWNT

deposition. Films grown by CVD have long average tube lengths, few number of tube aggregation into larger bundles, and the ability to control tube alignment in the film [69]. In general, SWNT films grown in this manner are employed in small scale electronic applications such as electrical transistors with channel lengths on the same length scale as the nanotubes ca. < 500 μm [64, 69]. However, for application as a transparent electrode, the ability to produce large area depositions (ca. > 1 $m^2$) cost effectively is desired for which films deposited by solution processing are most amenable.

### 2.5.1. SWNT Solution Preparation

The method used to generate SWNT solutions can be generally described in the following processing steps: (1) SWNTs are batch synthesized, (2) SWNTs are purified to remove any residual catalysts, amorphous carbon, and other impurities, and (3) SWNTs are dissolved into solution with the aid of high power sonication. The details of SWNT synthesis was previously described (section 2.4). It is known that all current SWNT synthesis techniques generate significant amounts of carbonaceous impurities, such as amorphous carbon, graphite sheets, and residual catalysts [42, 70]. Without a rigorous purity process to remove the aforementioned impurities, subsequent integration of as-synthesized SWNTs into organic electronics would result in suboptimal performance. After successful purification, it is possible to reach purities of SWNTs exceeding 90% (P3 SWNTs by Carbon Solutions, Inc.). While many variations of purification processes exist, the most common methods include acid purification and subsequent centrifugation as primary steps [71, 72]. In this process, SWNTs are refluxed in acid (e.g. nitric acid) before room temperature cooling, dilution with DI water, centrifugation, and membrane

filtration [71, 72]. In addition to removing unwanted residual impurities, acid purification also results in the significant modification of the SWNTs. Because acids, such as nitric acid, are strong oxidants, too harsh of a treatment can result in the conversion of SWNTs into carbonaceous impurities [72]. Therefore, much care has to be undertaken during purification as to only dissolve metal catalysts and attack amorphous carbon. After membrane filtration, SWNTs are collected and exist in "soot" powder form in aggregated SWNT ropes that can easily be handled for later processing. SWNT ropes are bundles of individual SWNTs aggregated together due to the high van der Waals forces between SWNTs.

With the aid of high power sonication such as probe sonication or bath sonication, purified SWNTs in powder form can be dispersed into solvents for future solution processing. Due to the hydrophobic nature of carbon nanotubes, pristine SWNTs will not readily disperse into aqueous solutions. Therefore, approaches that are most commonly pursued are: dispersion in organic solvents and surfactant based aqueous dispersion. Good solubility has been demonstrated in only a limited number of organic solvents, such as nitromethane [73], *N*,*N*-dimethylformamide (DMF) [73, 74], dimethyl acetamide (DMAc) [74], and dimethyl pyrrolidone (NMP) [73, 74]. However, SWNT dispersion into these organic solvents typically requires excessive sonication (ca. 100 hours in bath sonicator [73]) that can lead to considerable mechanical damage and thereby electrical degradation to the nanotubes [75]. Also, because of down-stream processing, highly flammable and toxic organic solvents such as those aforementioned are not desired and as such, water is the preferred solvent.

Pristine carbon nanotubes are non-polar and thus exhibit hydrophobic behavior in water. Therefore, the aggregated bundles of SWNTs do not break up and easily disperse into the aqueous medium. However, amphiphilic molecules (i.e. molecules containing a hydrophilic head and a hydrophobic tail) such as surfactants can be used to aid in aqueous dissolution. In this approach, the hydrophobic tail readily adsorbs on the surface of SWNTs while the hydrophilic head mixes with water (Figure 2.14).

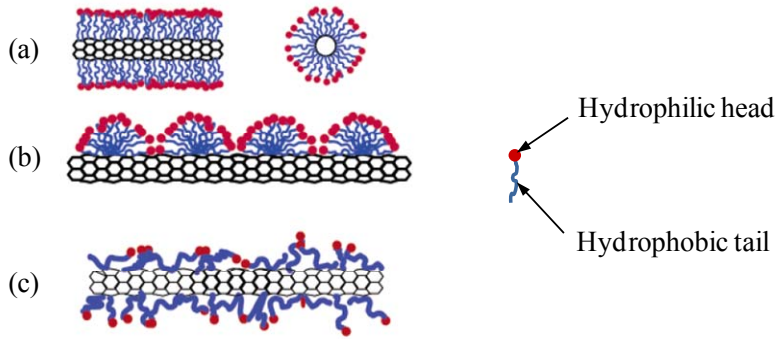


**Figure 2.14.** Schematic representations of the mechanisms by which surfactants adsorb on the surface of SWNTs to aid in dispersion. (a) SWNTs at the core of cylindrical surfactant micelles (side view on left, cross section on right). (b) Hemispherical adsorption of surfactant micelles on energetically favorable positions on the SWNT. (c) Random adsorption of surfactant molecules on SWNT surface. Adapted from reference [76].

The surfactant also provides sufficient electrostatic repulsion to nearby SWNTs to prevent re-aggregation. With the aid of mechanical sonication to break up SWNT bundles, the hydrophobic tails of the surfactant can attach to individual SWNTs and create stabilized solutions of individual SWNTs in water [74]. Figure 2.15 illustrates this

process. Common surfactants that have been used to disperse SWNTs are sodium dodecyl sulfate (SDS) [77], sodium dodecylbenzenesulfonate (SDBS) [78], Triton X [65, 79], and poly(vinylpyrrolidone) PVP [78]. The typical surfactant concentration by weight percent is 1% [13, 80]. Shown in Figure 2.16 are examples of poorly dispersed and well dispersed aqueous based SWNT solutions.

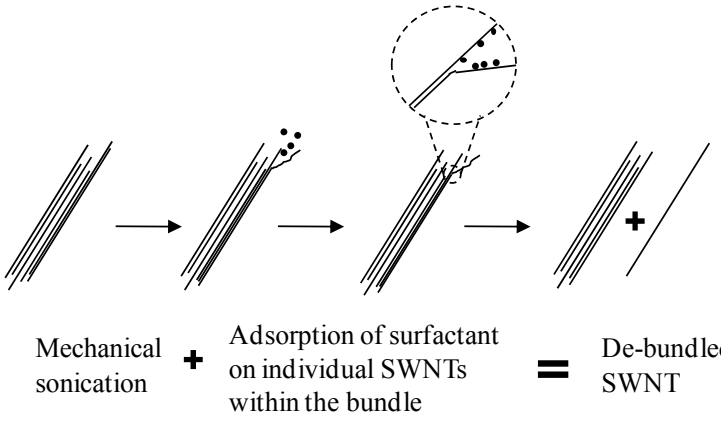


**Figure 2.15.** Schematic of individual nanotube isolation from bundle via ultrasonication and surfactant adsorption. Mechanical sonication provides sufficient energy to break up SWNTs such that subsequent adsorption of surfactants result in de-bundled SWNTs. Adapted from reference [74].


**Figure 2.16.** Photograph of poorly dispersed SWNT solutions (2 images on left) and a well dispersed SWNT solution (image on right). Taken from reference [81].

Covalent functionalization of SWNTs can also assist in aqueous dispersion by creating interactions with the tube surface and surrounding environment. In particular, covalent functionalization of SWNTs with carboxylic acids (COOH) has been shown to significantly enhance SWNT solubility in water [82, 83]. Refluxing in nitric acid, or sonication in a mixture of sulfuric acid and nitric acid lead to high concentrations of carboxylic acids covalently bonded defects on the sidewalls and the free ends of SWNTs (Figure 2.17) [84]. Carboxylic acids are preferentially bonded to the highly reactive defect sites due to large local strains [84]. Surface attached carboxylic acid groups result in the development of a negative electrostatic charge on the SWNTs [85]. As a result, the SWNTs lose their pristine non-polar characteristics and become more hydrophilic. Also, the net surface charges act as repulsive forces between individual SWNTs to promote de-bundling and hinder subsequent aggregation [85]. Because SWNTs are typically purified using acid reflux, if no further treatment is taken to remove carboxylic acid groups, all purified SWNTs will contain a non-negligible amount of acid groups [86]. However, some SWNTs manufacturers provide SWNTs with enhanced levels of attached carboxylic acid groups (P3 SWNTs, Carbon Solution, Inc.) by ensuring that functional groups created during acid treatment are retained throughout the purification process.

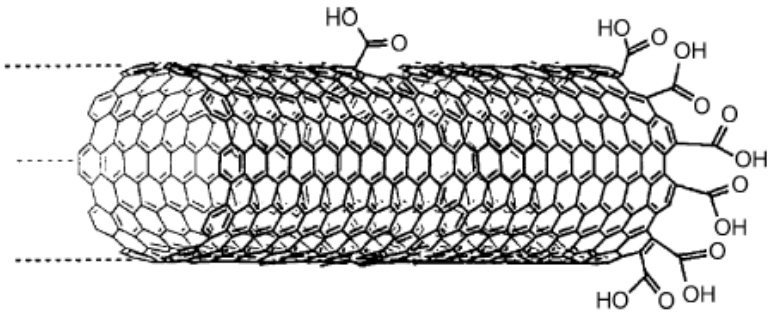


**Figure 2.17.** Chemical structure of SWNT with carboxylic groups attached. Taken from reference [84].

Dispersion of SWNTs in solution is done with the aid of mechanical separation via sonication. The amount of ultrasonic energy necessary to produce stable solutions of SWNTs is dependent on the surfactant/solvent selection, attractive forces between individual SWNTs, and the degree of individual SWNT to bundles/ropes of SWNTs desired (e.g. 100% individual SWNTs with no SWNT ropes or solution containing a mixture of the two). As more energy is added to the solution via sonication, the percentage of individual SWNTs increases. However, sonication has been shown to induce mechanical damage to SWNTs; therefore, an acceptable compromise must often be met [75]. After initial SWNT solutions are prepared via sonication, centrifugation is also used to produce SWNT solutions high in individual SWNT content and low in non-SWNTs impurities [80, 87]. Centrifugation has been shown to remove graphitic impurities, catalyst residuals, and large SWNT bundles from SWNT solutions due to density variations [87].

### 2.5.2. SWNT Films Processed From Solution

Successful methods to produce randomized SWNT networks from solution include spray coating [88], dip coating [65], electrophoretic deposition [89], spin coating [90], and vacuum filtration [13, 77]. In addition to differing manufacturing complexity, these methods also vary in scalability, film-to-film consistency, and film properties. The primary figures of merit used to evaluate SWNT networks as transparent conductors are sheet resistance, $R_{sh}$, optical transmittance at 550 nm, surface roughness, and electrical stability under bending induced strain. Prior to presenting the different SWNT film deposition techniques, these primary figures of merit will be discussed in the following section.

#### 2.5.2.1. Primary Figures of Merit

##### 2.5.2.1.1. Sheet Resistance of SWNT Films

The sheet resistance of SWNT networks is of importance because of its contribution to the resistive power losses in organic devices. $R_{sh}$ losses are in series with other resistive losses in the devices with an associated power loss of $P_{loss}^{sh} = I^2 * R_{sh}$ where $I$ is equal to the current collected by the electrode. $R_{sh}$ is used to characterize the two-dimensional electrical properties of the conductor. This property assumes negligible current flow in the direction perpendicular to the plane of the electrical conductor, thereby only describing lateral conduction within the film. It is given in terms of Ω-sq$^{-1}$, and is defined as

$$R_{sh} = R\frac{W}{L} \tag{2.10}$$

Therefore, $R_{sh}$ can be simply understood to give the resistance, $R$, between two contacts of width, $W$, at a length, $L$, apart. Due to the percolating nature of SWNT networks, $R_{sh}$ is expected to vary inversely with film surface density [30]. Since surface density is directly proportional to film thickness ($t$), $R_{sh}$ should also scale with the inverse of film thickness. An example of this relationship is shown in Figure 2.18. A clear inverse relationship can be seen between $R_{sh}$ and the film thickness, as $R_{sh}$ approaches a saturation level. This can also be illustrated with regard to Figure 2.13 where the nanotube network was schematically shown. As the film thickness increases, more conducting pathways are created. Since the conducting pathways are in parallel across the 2D network, the overall resistance $R_{sh}$ should also vary as:

$$R_{sh} \sim \frac{1}{x} R_{path} \tag{2.11}$$

where $x$ is equal to the number of conducting pathways in the film.

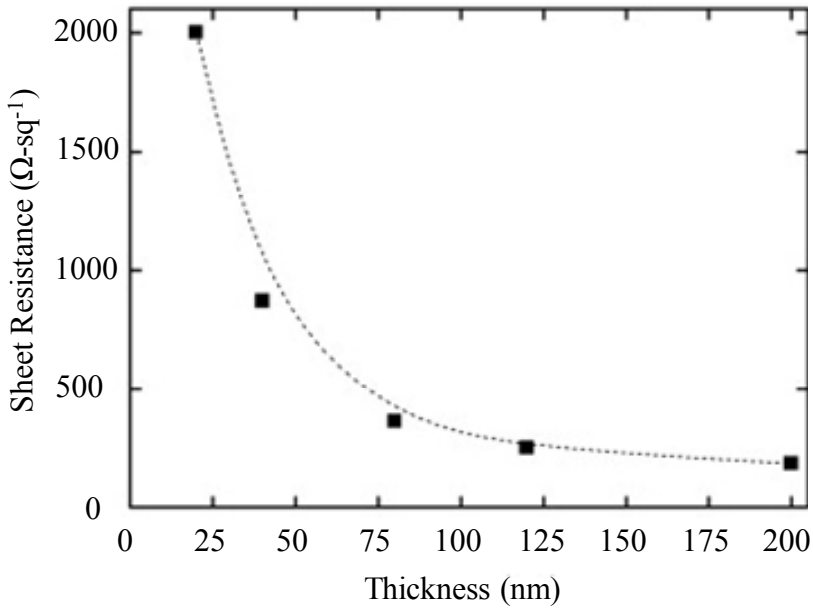


**Figure 2.18.** $R_{sh}$ as a function of SWNT film thickness. Line is drawn as a guide to the eye. Adapted from reference [91].

2.5.2.1.2. Optical Transmittance of SWNT Films

Typically when the optoelectronic properties of transparent electrodes are presented and discussed in the literature, the optical transmittance near the visible spectrum is given [92]. Only wavelengths near the visible spectrum are shown for electrodes employed in organic electronics because OLEDs emit colors visible in this range, while the optimal absorption efficiency of OPVs is in the range of 400-800 nm. Sample SWNT films of varying thickness are shown in Figure 2.19 [91]. As expected, the optical transmittance decreases with increasing film thickness. By convention, the transmittance at 520 or 550 nm is given as a representative value of the overall transmittance in the visible spectrum due in large part to the relative optical consistency of transparent conductors used as electrodes for organic devices (e.g. Figure 2.19) [93]. Therefore, optical transmittance at 550 (or 520) nm can be seen as a useful gauge of the transmission losses due to absorption by the electrode.

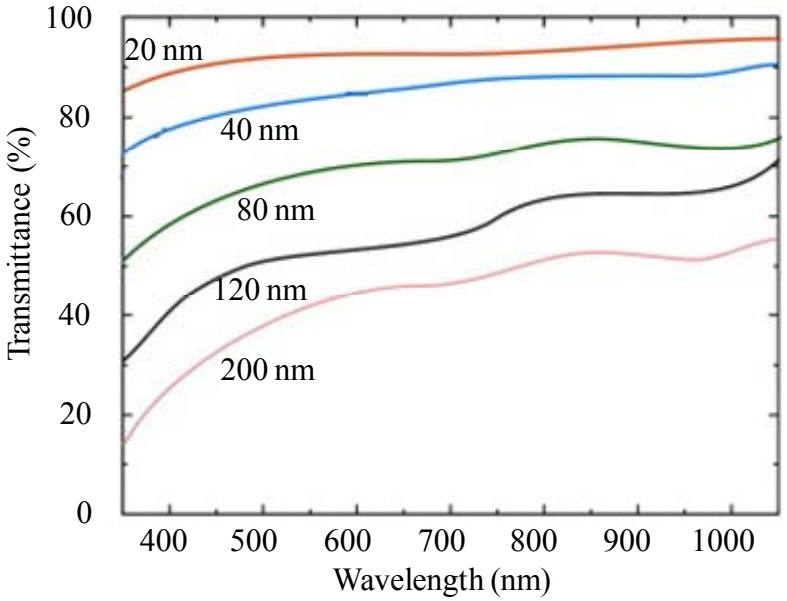


**Figure 2.19.** Optical transmittance of SWNT films of several thicknesses. Adapted from reference [91].

As seen in Figures 2.18 and 2.19, optical losses increase with increasing film thickness due to lower film transmittance while electrical losses decrease with a similar increase in thickness. Therefore, a tradeoff must be achieved between optical and electrical losses in SWNT films. Shown in Figure 2.20 is a plot of the corresponding relationship and expected competing performance goals. Since, a decrease in $R_{sh}$ is most often accompanied with a decrease in transmittance, they are most often combined when presented. In this regard, $R_{sh}$ is often quoted with a given transmittance at 550 nm. Since 80% transmittance at 550 nm is often viewed as a standard benchmark transmission that SWNTs transparent electrodes must meet or exceed to be a viable replacement for ITO, $R_{sh}$ is often presented with transmittance ≥ 80% [13, 94]. State of the art optoelectronic values of pristine SWNT films include $R_{sh}$ of 186 Ω-sq$^{-1}$ and 129 Ω-sq$^{-1}$ with

transmittances at 550 nm of 86% [94] and 80% [95] respectively. It must be noted that these state of the art values represent by far some of the best optoelectronic values seen in the literature. Typical $R_{sh}$ values with transmittances at 550 nm of 80-85% are in the range of 250 Ω-sq$^{-1}$ – 400 Ω-sq$^{-1}$ [80, 96, 97], with many $R_{sh}$ values presented on the kΩ-sq$^{-1}$ range for a similar transmittance [65, 98].

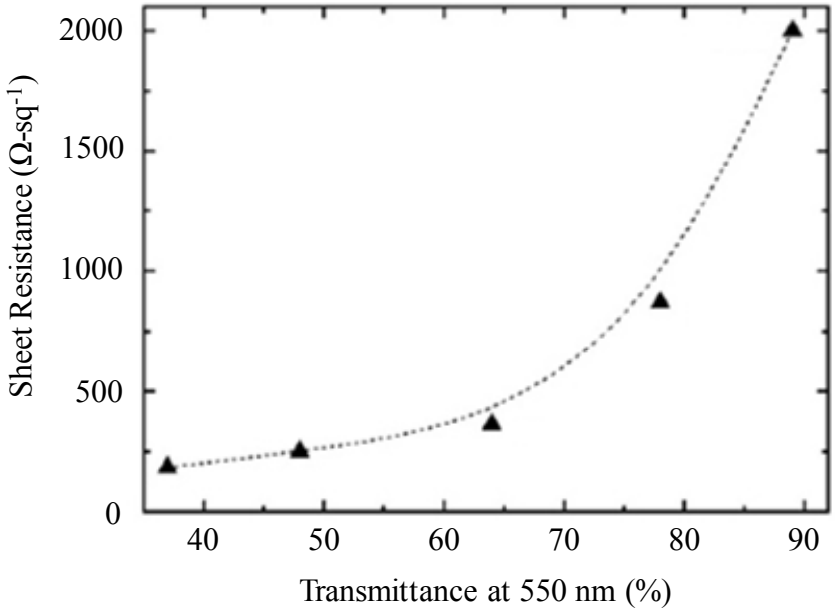


**Figure 2.20.** Correlation between transparency and $R_{sh}$. Film transparency represented by transmittance at 520 nm. Taken from reference [91].

2.5.2.1.3. Roughness of SWNT Films

As shown in Figure 1.2, the active layers of organic devices are sandwiched between the positive and negative electrode. Because the active layers in organic photovoltaics are on the order of 10 to 100 nm in thickness due to the relatively short exciton diffusion lengths [99], the surface roughness of each electrode layer is of

significant importance to the operation of the device. Highly rough SWNT films can develop electrical shorts by piercing through active layers to extend to the negative electrode. An atomic force microscope (AFM) image of example SWNT film (~40 nm thick) is shown in Figure 2.21 [80]. The average roughness, $R_a$ is approximately 7 nm. However, a thin layer of a commonly used conductive polymer (PEDOT:PSS) can be applied to smoothen the sample (Figure 2.21b) to a $R_a$ of 3.1 nm. For comparison, an AFM image of ITO is shown with a $R_a$ of 2.4 nm [80].

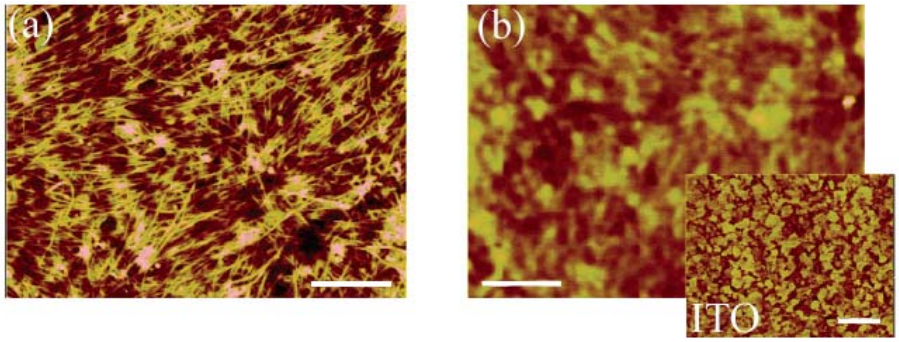


**Figure 2.21.** (a) AFM image of a pristine SWNT film on glass with an average surface roughness of ca. 7 nm. (b) AFM image of a PEDOT:PSS – passivated nanotube film with an average surface roughness of 3.1 nm. Inset: AFM image of typical ITO substrate on glass with an average surface roughness of 2.4 nm. Scale bar = 1 μm. Adapted from reference [80].

2.5.2.1.4. Mechanical Stability of SWNT Films

Mechanical stability is determined in SWNT films by measuring electrical resistance as a function of bending. SWNT films demonstrate excellent bending performance as shown in Figure 2.22, where the film resistance is plotted as a function of

bending angle. For comparison, the resistance of ITO under similar loading is shown. Even under extreme bending conditions of a 180° bending angle, the SWNT film exhibited sustained electrical conductivity, while the ITO film experienced catastrophic electrical failure at a bending angle around 45°. The electrical stability of SWNT films is further illustrated in Figure 2.23 [65]. As revealed in a less than 10% increase in $R_{sh}$ after 10,000 cycles of bending to 12.5 mm, SWNT films also demonstrate sustained electrical conduction under fatigue loading.

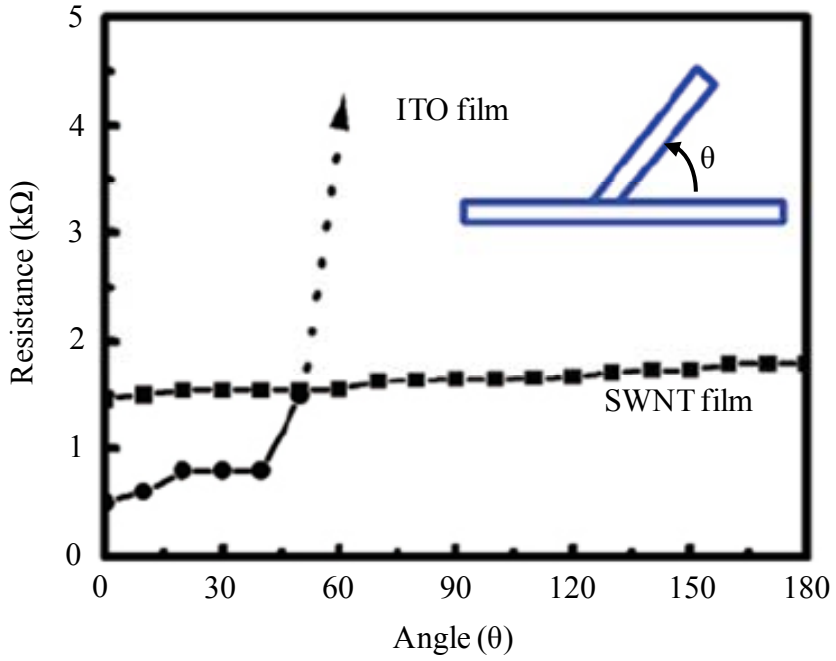


**Figure 2.22.** Electrical stability of a SWNT film on a flexible PET substrate. Taken from reference [31].

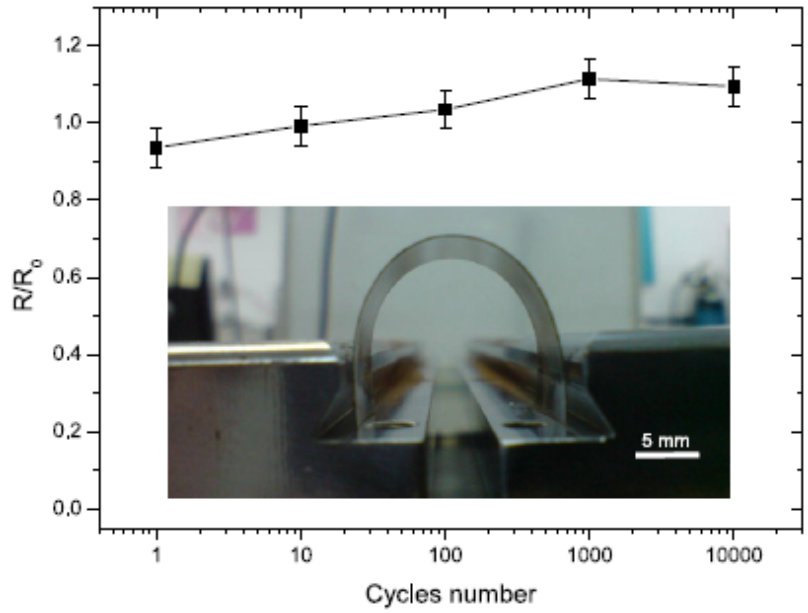


**Figure 2.23.** Change in $R_{sh}$ (after repeated bending to a radius of 12.5 mm) as a function of the number of cycles. Mechanical stability is illustrated by a final $R_{sh}$ of less than 10% greater than the initial $R_{sh}$ of 385 Ω-sq$^{-1}$. The distance between the parallel plates was changed at a rate of 50 mm-s$^{-1}$. Scale bar = 5 mm. Taken from reference [65].

2.5.2.2. SWNT Film Electrode Fabrication Methods *(Processed From Solution)*

2.5.2.2.1. Spray Coating

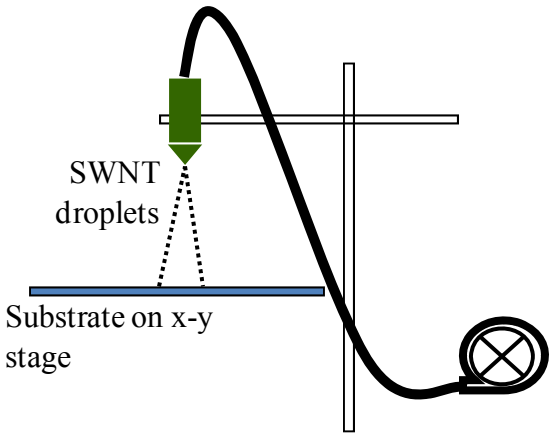


**Figure 2.24.** Schematic of spray coating method.

In this simple approach, SWNT solutions are directly sprayed onto substrates via an air brush pistol or other "spray" tools (Figure 2.24). The substrate is kept hot during the process (ca. 100°C) to accelerate drying of the fine solution droplets on the surface [88]. While the airbrush technique provides a simple and quick method to tune film thickness, significant heterogeneity on the nanometer scale can exist as evidenced by the relatively large error bars for film transparency versus thickness in Figure 2.25 reported by Kaempgen et al. [88]. An example $R_{sh}$ of SWNT films deposited by these authors was 1 kΩ-sq$^{-1}$ with 90% transmittance at 500 nm. However, with a $R_{sh}$ of ca. 160 Ω-sq$^{-1}$ and transmittance of 80% at 550 nm, Geng et al. [100] later demonstrated that low $R_{sh}$ films could be produced using spray deposition. An acid treatment process was subsequently used to remove residual surfactant and further decrease $R_{sh}$ by a factor of ~ 2.5 to a final value of 70 Ω-sq$^{-1}$.

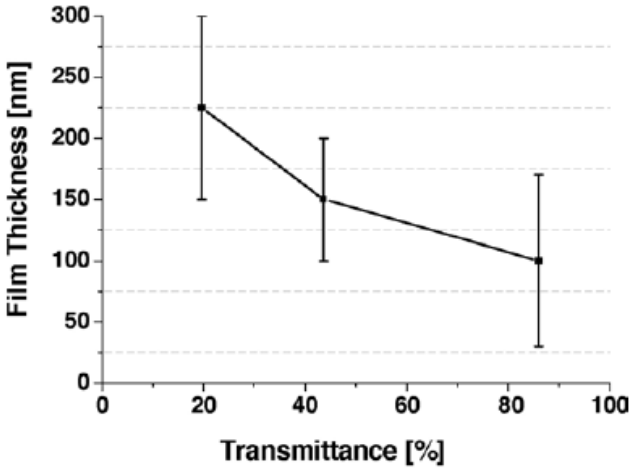


**Figure 2.25.** Transmittance (at 550 nm) versus film thickness of SWNT networks determined by AFM at step edges. Taken from reference [88].

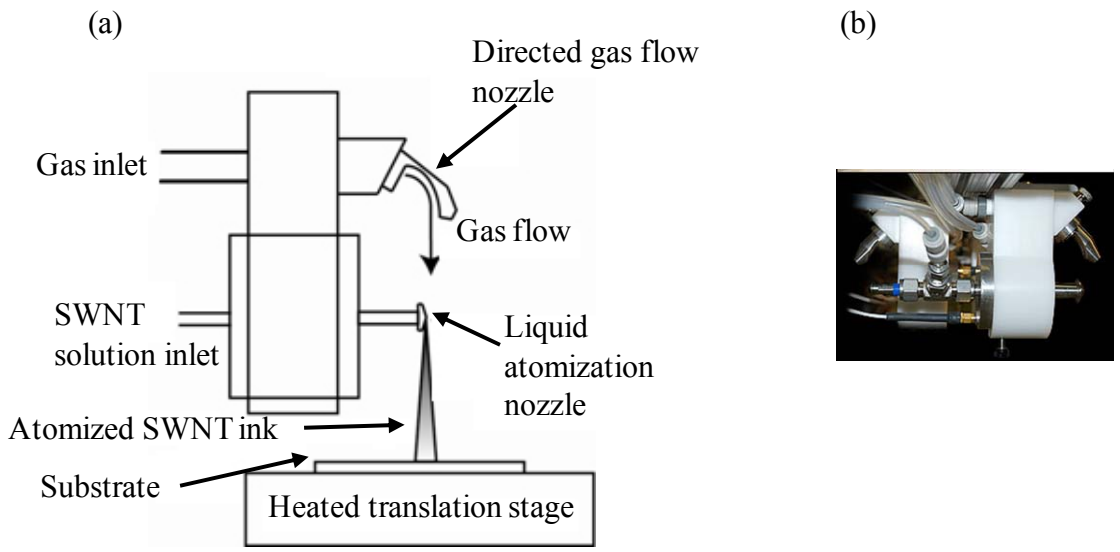


**Figure 2.26.** (a) Ultrasonic spray apparatus. Gas is directed over the atomized SWNT ink to uniformly dispense SWNTs over the substrate. Figure adapted courtesy Dr. Robert Tenent at the National Renewable Energy Laboratory. (b) Photograph of ultrasonic spray nozzle (*http://www.sono-tek.com*).

The successful deposition of SWNT films by spray coating with high surface uniformity and low surface roughness was recently achieved by Tenent et al.[101]. They attributed the improved surface properties to two major advances: (1) aqueous SWNT solutions were dispersed using a polymeric derivative of cellulose (sodium carboxymethyl cellulose (CMC)) and (2) ultrasonic spraying of the solution onto the substrate (Figure 2.26). While other spray techniques utilize SDS to disperse SWNTs [88], CMC was found to disperse ca. 20 times the amounts of SWNTs into water than possible with SDS. The authors asserted that due to the strong binding between CMC and the SWNTs, individual nanotubes were isolated and suspended with more gentle sonication and centrifugation than typically required for SDS. Their data suggested that ca. 95% of the SWNTs in the CMC based dispersion were individual in nature versus

aggregated bundles. The rms roughness of sprayed films was 3 nm over a 10 μm x 10 μm area. A representative AFM image and line scan are provided in Figure 2.27. After removal of the CMC polymer via overnight exposure to 16 molar $HNO_3$, low $R_{sh}$ values of 150 Ω-sq$^{-1}$ with 78% transmittance at 550 nm were obtained for sprayed SWNT films. This work represents an easily scalable SWNT film deposition technique, as the authors demonstrated with an optically homogenous 6 inch x 6 inch SWNT film on glass (Figure 2.27a).

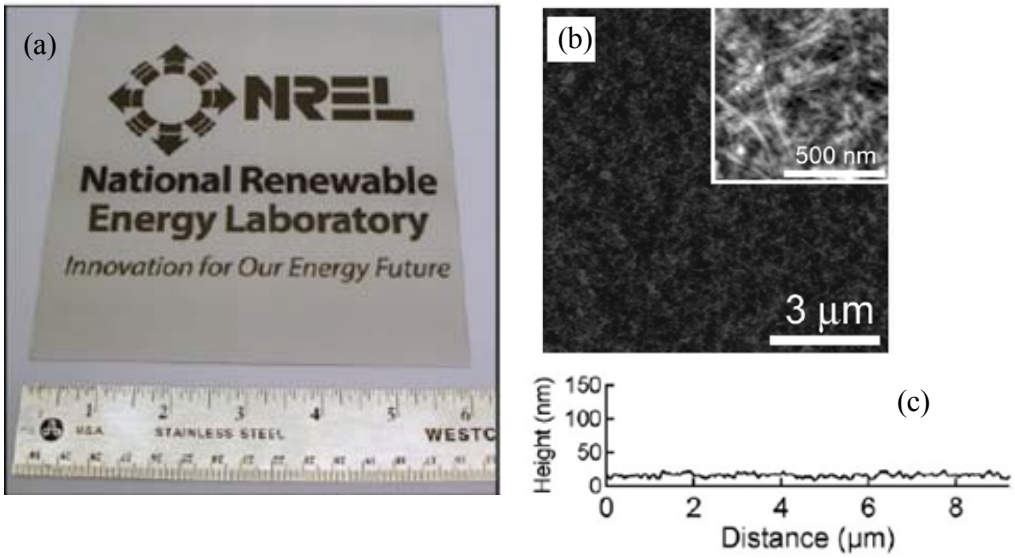


**Figure 2.27.** (a) Photograph of a 6 inch x 6 inch glass substrate prepared using an ultrasonic spray technique. Ruler shown below the film for scale. (b) Large-area AFM image of transparent SWNT film ultrasonically sprayed and subsequently acid treated to remove polymer dispersant. Inset: High magnification AFM image to reveal resolution of individual SWNT and/or small bundles. (c) Line scan of film shown in (b), to demonstrate long-range uniformity and low surface roughness. Adapted from reference [101].

2.5.2.2.2. Dip-Coating

Ng et al. [65] utilized a dip-coating method to fabricate thin networks of SWNTs. Because SWNTs are intrinsically hydrophobic, Aminopropyltriethoxysilane (ATPS) was applied to the substrate as an adhesion promoter to facilitate uniform and controllable nanotube coatings. The substrate was subsequently immersed into the SWNT solution for 2 minutes to allow the substrate and solution to stabilize. Next the substrate was withdrawn at a continuous speed and allowed to dry in ambient nitrogen. After drying, the process was repeated until the desired number of coatings was achieved. A schematic of the process is shown in Figure 2.28. The best results were obtained for films prepared from an aqueous solution of SWNTs dispersed with surfactant (Triton X-100). An AFM image of a film dip-coated 5 times is shown in Figure 2.28b. The rms roughness of the films was ca. 12 nm. Optical images of four samples coated 1, 3, 5, and 10 times are shown in Figure 2.28c. The thickness of the film increased with each additional coating. In turn, $R_{sh}$ and transmittance at 550 nm also decreased with additional coatings as shown in Figure 2.29. Five coatings were necessary to obtain 84% transmittance at 550 nm for the Triton X-100 based SWNT solution, compared to 16 for the SDS based SWNT solution. The Triton X-100 also exhibited a lower $R_{sh}$ of 2.05 kΩ-sq$^{-1}$, in contrast to 2.69 kΩ-sq$^{-1}$ for SDS. The authors found that a post-deposition acid treatment was necessary to remove residual surfactant and ATPS from the surface of the SWNTs and thus result in lower $R_{sh}$. A sample film with a $R_{sh}$ of 736 Ω-sq$^{-1}$ was shown to exhibit a factor of 2.7 decrease in $R_{sh}$ after acid treatment.

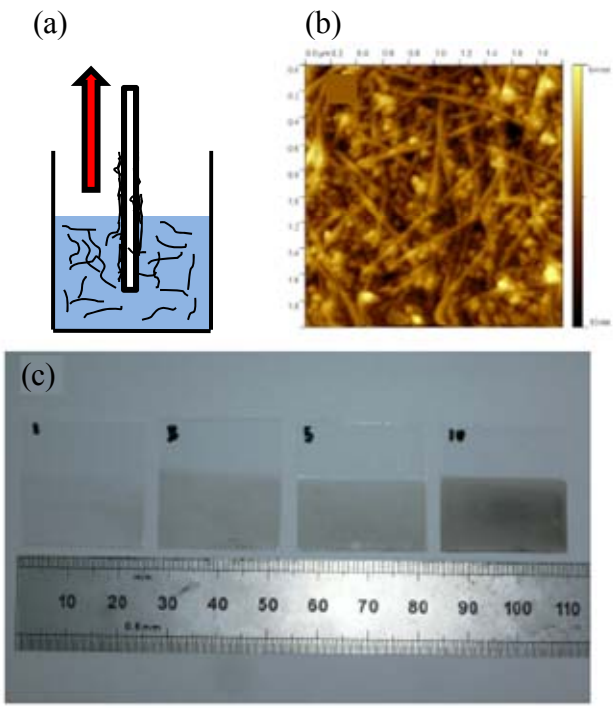


**Figure 2.28.** (a) Schematic of dip coating procedure. (b) 2 μm x 2 μm AFM image of a SWNT film after 5 coatings. (c) Optical image of SWNT films after 1, 3, 5, and 10 coatings. Adapted from reference [65].

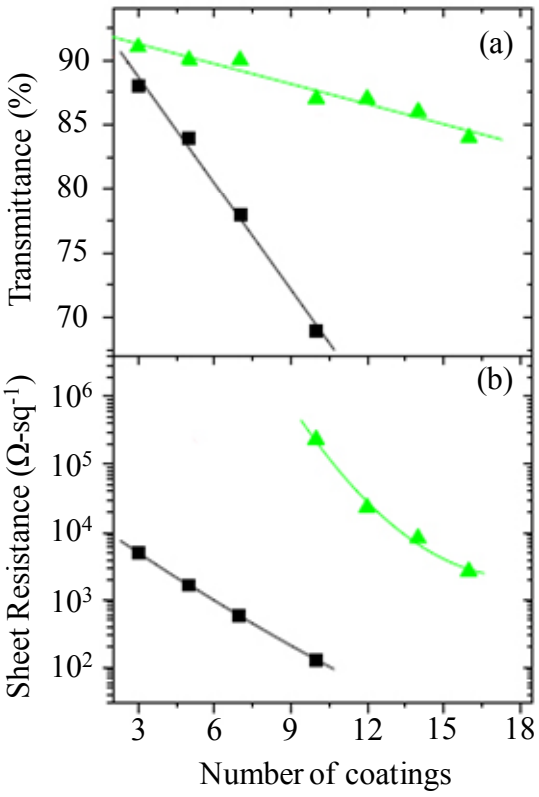


**Figure 2.29.** (a) Transmittance at 550 nm and (b) sheet resistance of SWNT films as a function of the number of coatings for samples coated with (■) SWNT / Triton X-100 aqueous solution and (▲) SWNTS / SDS aqueous solution. Adapted from reference [65].

2.5.2.2.3. Electrophoretic Deposition

Lima et al. [89] successfully deposited thin conductive films of SWNTs on borosilicate glass and poly(ethylene terephthalate) (PET) using a technique based on electrophoretic deposition. A thin layer of metal (aluminum or titanium) was first evaporated onto the transparent substrate to act as the positive electrode during the deposition. The substrate was then immersed into the SWNT solution and a voltage was applied between it and a negative electrode also immersed in the aqueous SWNT solution

(Figure 2.30). During the electrophoretic process, the SWNTs acquired a negative charge in the aqueous solution and thus became attracted to the positive electrode. After deposition, the substrate was withdrawn from solution and the metal was acid etched away. The thickness of the SWNT film was controlled by changing the concentration of the SWNT solution.

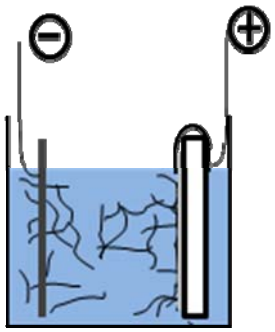

**Figure 2.30.** Schematic of electrophoretic deposition SWNT film deposition. Adapted from reference [89].

While the obtained $R_{sh}$ of films fabricated by this method were relatively high (i.e. $R_{sh} \approx 1$ kΩ-sq$^{-1}$ with 80% transmittance at 550 nm), the authors contended that electrophoretic deposition is a promising technique due to the ability to provide patterned deposition and the smoothness of the SWNT film surface. Shown in Figure 2.31 is a patterned network used to illustrate the potential for this process. The smallest features achieved by Lima et al. were of the order of 8 μm. Also, for thin networks (~ 81% transmittance at 550 nm) prepared from SWNTs dispersed in water with the aid of SDS, an average roughness of 5.5 ± 3.4 nm was achieved.

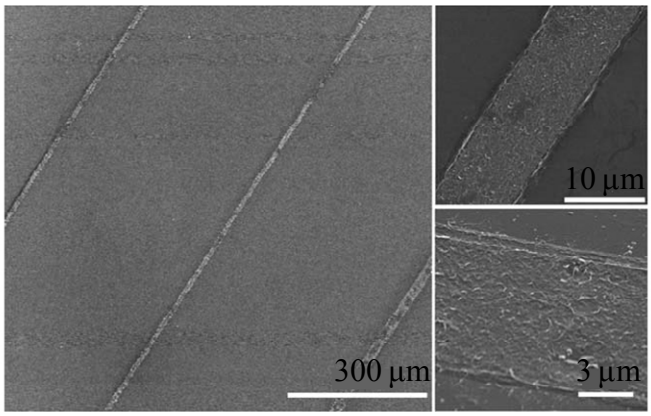


**Figure 2.31.** Patterned SWNT network prepared by electrophoretic deposition. Adapted from reference [89].

2.5.2.2.4. Spin Coating

Spin coating is a common laboratory process used to apply uniform thin films to flat substrates. An excess amount of solution is placed on the substrate that is subsequently rotated at high speeds to produce a centrifugal force that spreads the fluid uniformly over the substrate (Figure 2.32). Yim et al. [102] dispersed SWNTs in dichloroethane (DCE), for spin coating. The authors suggested that the use of DCE as a SWNT solvent and subsequent spin coating solution was key, due its ability to disperse SWNTs and its volatility. The SWNT film thickness was controlled by the number of times a spin-coated layer was allowed to dry to have a successive layer spin coated on top of it. For SWNT films prepared on glass substrates, spin coating was repeated 100 times to obtain an $R_{sh}$ of 320 Ω-sq$^{-1}$ with a transmittance of 83% at 550 nm. The rms roughness of these films was ca. 10 nm.

It must be noted that the use of volatile organic solvents as suggested by Yim et al. must be approached with a high regard for safety. High quality dispersion of SWNTs

into solvents (organic or surfactant based) most often require a centrifugation step after sonication. Therefore, much care must be taken to ensure that during centrifugation, the centrifuge rotor does not exceed a safe operating temperature for volatile liquids under centrifugal force. Yim et al. specified that centrifugation at 48,000 g for 20 minutes was necessary to properly induce sedimentation of large SWNT bundles and carbonaceous impurities. However, the safety precautions necessary for this step were not discussed. It is the opinion of this author that organic solvents should be avoided when preparing SWNT solutions, if centrifugation is necessary.

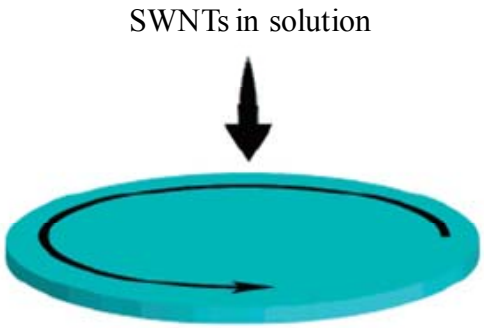


**Figure 2.32.** Schematic process of SWNT spin coating procedure. Adapted from reference [90].

2.5.2.2.5. Vacuum Filtration

The most common method due to its simplicity and processing consistency, vacuum filtration consists of a vacuum-induced flow of the SWNT solution through a membrane filter. Surface consistency is promoted by the nature of the vacuum filtration process [77]. As the solution sifts through the membrane filter, SWNTs are collected on

the surface, forming an interconnected network [63]. As SWNTs accumulate in one area of the membrane surface, the permeation rate of the solution is thereby locally impeded such that areas of less coverage on the membrane can be compensated. During the process, SWNTs tend to lie straight such that frequent overlap between SWNTs is achieved [77]. Lastly, the thickness of the film can easily be controlled by the nanotube concentration and volume of the SWNT solution. After filtration, the film is washed with copious amounts of water to try to remove residual surfactant adsorbed on SWNT surfaces. An illustration of this process is shown in Figure 2.33.

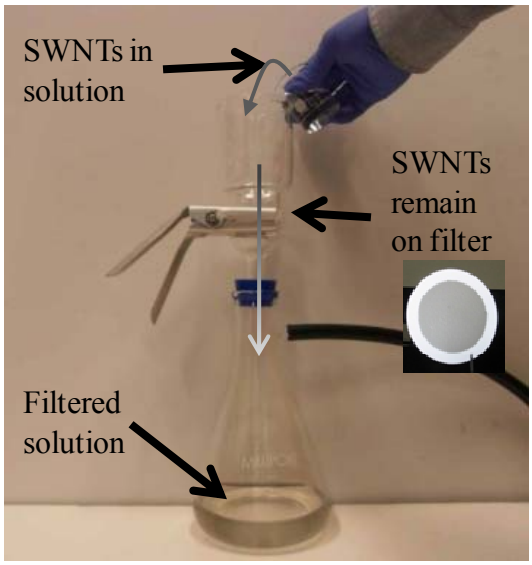


**Figure 2.33.** Schematic of vacuum filtration process. Inset: SWNTs left on membrane filter.

Two primary methods exist for transferring the filtered SWNT film from the vacuum filter to the desired substrates: via an elastomeric PDMS stamp [25] or through chemical exposure of the filter and film such that the filter paper dissolves away [77]. In

the former method, an alumina membrane filter is used in the vacuum filtration process. Conformal contact is made between the PDMS stamp and the SWNT film until full wetting of the SWNTs on the PDMS is seen. The stamp is then raised from the filter with the SWNTs attached and subsequently "printed" onto flat substrates with a higher surface energy than PDMS. Since PDMS has a low surface energy of 19.8 $mJ/m^2$ [13], SWNTs can be transferred to transparent substrates such as PET and glass with surface energies of 44.6 $mJ/m^2$ and 47 $mJ/m^2$ respectively [13]. Substrate heating can be used to further promote film transfer. An illustration of this process developed by Zhou et al.[13] is shown in Figure 2.34. An added advantage of this method is that PDMS can easily be molded to transfer patterned SWNT networks as shown in the figure. Li et al. [95] utilized this method to fabricate SWNT films with a $R_{sh}$ of 120 $\Omega$-$sq^{-1}$ and transmittance of 80% at 550 nm. The rms roughness of films produced in the manner range from 6 -10 nm [13, 95, 103]. A sample AFM image and line scan of the SWNT surface is shown in Figure 2.35. Also, the adhesion of the SWNTs to the substrate is sufficiently strong, such that the films could not be removed using Scotch Magic tape [13].

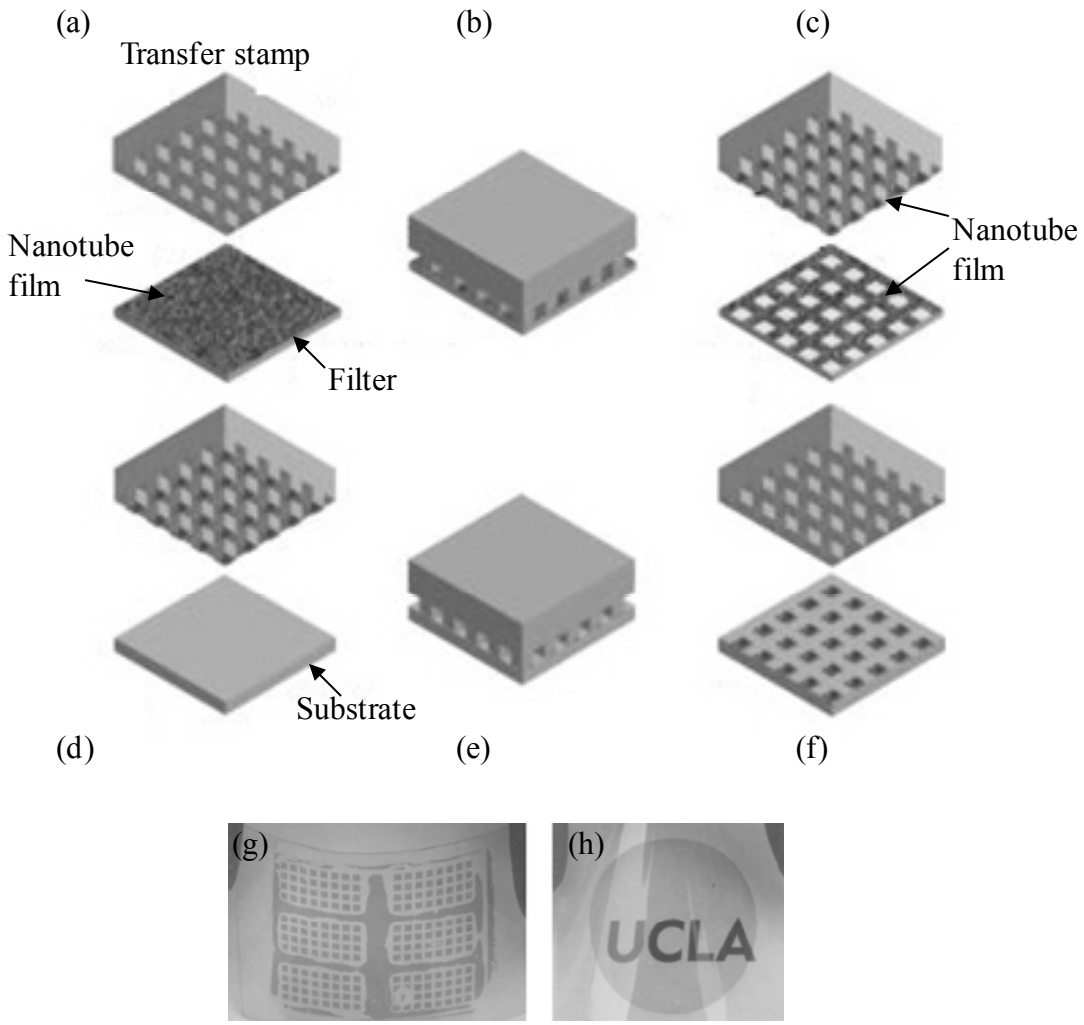


**Figure 2.34.** (a) Illustration of a patterned PDMS stamp and SWNT film. (b) Conformal contact made between the PDMS stamp and SWNTs on the filter. (c) After conformal contact the PDMS stamp is removed from the filter. (d) PDMS stamp and flat substrate. (e) Conformal contact made between PDMS stamp and substrate. (f) PDMS stamp removed from substrate after mild heating. (g) Photo image of patterned SWNT film on PET. (h) Photo image of SWNT film with 2 inch diameter on PET. Taken from reference [13].

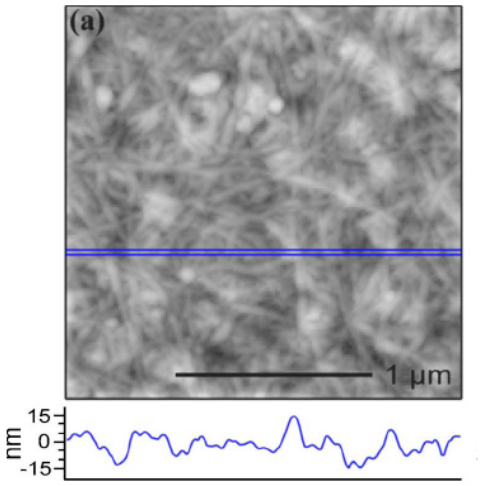


**Figure 2.35.** AFM image of SWNT network. The rms roughness is 7 nm. Adapted from reference [103].

Wu et al. [77] demonstrated that SWNTs films could be transferred to various substrates by utilizing a vacuum filtration membrane made of mixed cellulose esters (MCE) that could be dissolved easily with acetone. After filtration, the MCE membrane was placed on a substrate with the SWNTs in contact with the substrate. Force was also applied to promote adhesion of the SWNTs to the substrate. Subsequent acetone baths were used to dissolve the MCE membrane, leaving behind the vacuum filtered SWNT film firmly attached to the substrate via van der Waals forces. An illustration of this process is shown in Figure 2.36. Aguirre et al. [96] used this method to fabricate a SWNT film with a $R_{sh}$ of ca. 250 Ω-sq$^{-1}$ and 80% transmittance at 520 nm. The rms surface roughness of the film was 12 nm. Wu et al. were able to produce a SWNT film with a $R_{sh}$ of 30 Ω-sq$^{-1}$ and transmittance greater than 70% over the visible spectrum [77]. The $R_{sh}$ and corresponding transmittance of this film represent the best reported

optoelectronic properties of SWNT films in the literature. However, it must be noted that this value was achieved in 2004 and has not since been repeated in the literature.

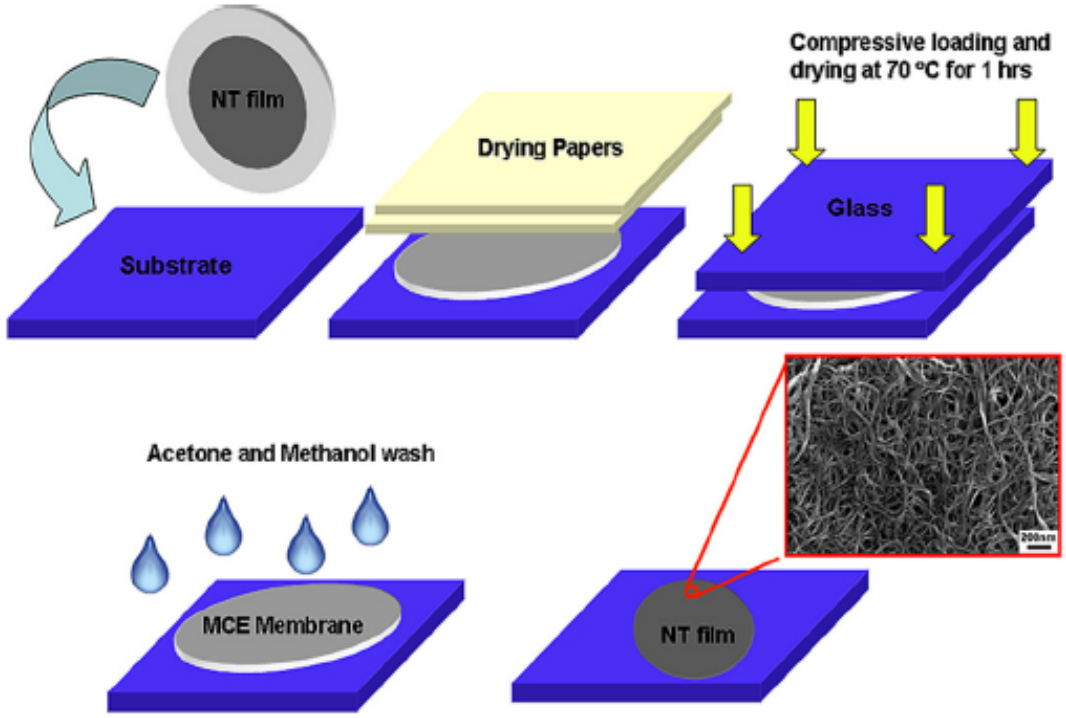


**Figure 2.36.** Illustration of the SWNT film transfer via MCE dissolution process. The process proceeds from left to right. Scale bar is 200 nm. Taken from reference [104].

### 2.5.3. Parameters Affecting Figures of Merit in SWNT Films

#### 2.5.3.1. SWNT Synthesis Method Impact on $R_{sh}$

Zhang et al. [80] compared the sheet conductance of films produced by arc discharge and HiPCO (High Pressure Carbon Monoxide) processes. They were able to show substantially better electrical properties of arc-discharged SWNTs with a sheet resistance 19 times less than HiPCO films with similar transmission at 550 nm. The superior performance of arc-discharged SWNTs was attributed to factors that include

nanotube dimensional differences, reduced defect density of arc-discharged SWNTs, the presence of non-SWNT impurities, and the bundle amount and diameter.

Geng et al. [100] conducted a similar study to ascertain the effect of SWNT synthesis on the optoelectronic properties of SWNT films. However, in addition to arc-discharged and HiPCO produced SWNT films, laser ablation and CVD synthesized SWNTs were compared. Similar to Zhang et al., they also found arc-discharge produced SWNTs to exhibit lower $R_{sh}$ at a given transmittance in comparison to HiPCO. Moreover, arc discharge SWNTs had the lowest $R_{sh}$ of all SWNT types, as shown in Figure 2.37.

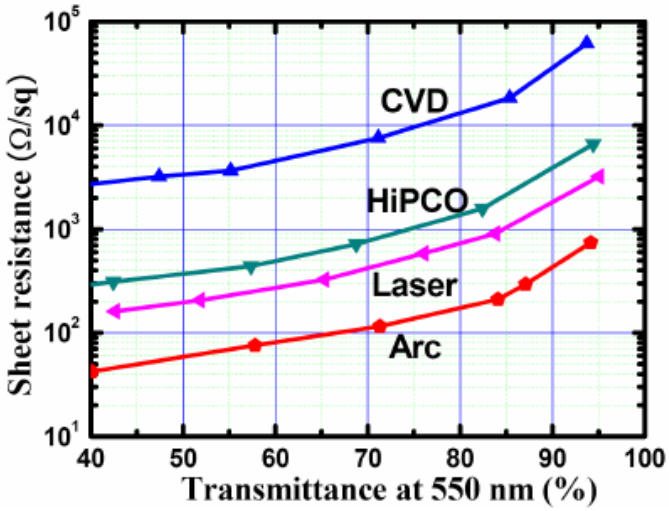


**Figure 2.37.** Sheet resistance versus transmittance at 550 nm for SWNT films fabricated from various synthesis methods. Taken from reference [100].

However, Parekh et al. [24] compared the electrical properties of HiPCO produced and arc-discharge, along with SWNTs produced via laser ablation and observed no salient differences. Hecht et al. [105] compared laser ablation produced SWNTs to arc-discharged produced SWNTs and also found similar electrical behavior. It must be

noted that the SWNTs produced via different synthesis methods in these studies were purchased from different carbon nanotube suppliers (arc-discharge were purchased from Carbon Solutions, Inc. and the HiPCO SWNTs were purchased from Carbon Nanotechnology Inc.). Therefore, different post-synthesis processing methods by the different suppliers may have contributed to the contrasting results of Zhang et al. with similar studies. The study by Geng et al. [100] did not specify that multiple suppliers were utilized and implied that no differentiation in post-synthesis processing was made among the various SWNTs. Therefore, it is likely the most accurate comparison of SWNT synthesis types.

2.5.3.2. SWNT Length and Bundle Diameter Impact on $R_{sh}$

Hecht et al. [105] compared the electrical properties of SWNT films with varying SWNT lengths, $L$, and bundle diameters, $D$. Their results suggested a positive relationship of lower $R_{sh}$ with smaller SWNT bundles and longer SWNTs. In their approach, probe sonication was used to obtain SWNT samples of varying lengths since it is known that mechanical sonication can be used to cut SWNTs into shorter segment. Because sonication also reduces the diameter of the SWNTs, it was difficult to fully decouple the results. The effects of sonication are shown in Figure 2.38. However, since the bundle diameter did stabilize prior the SWNT length, suggestions could be made concerning the behavior.

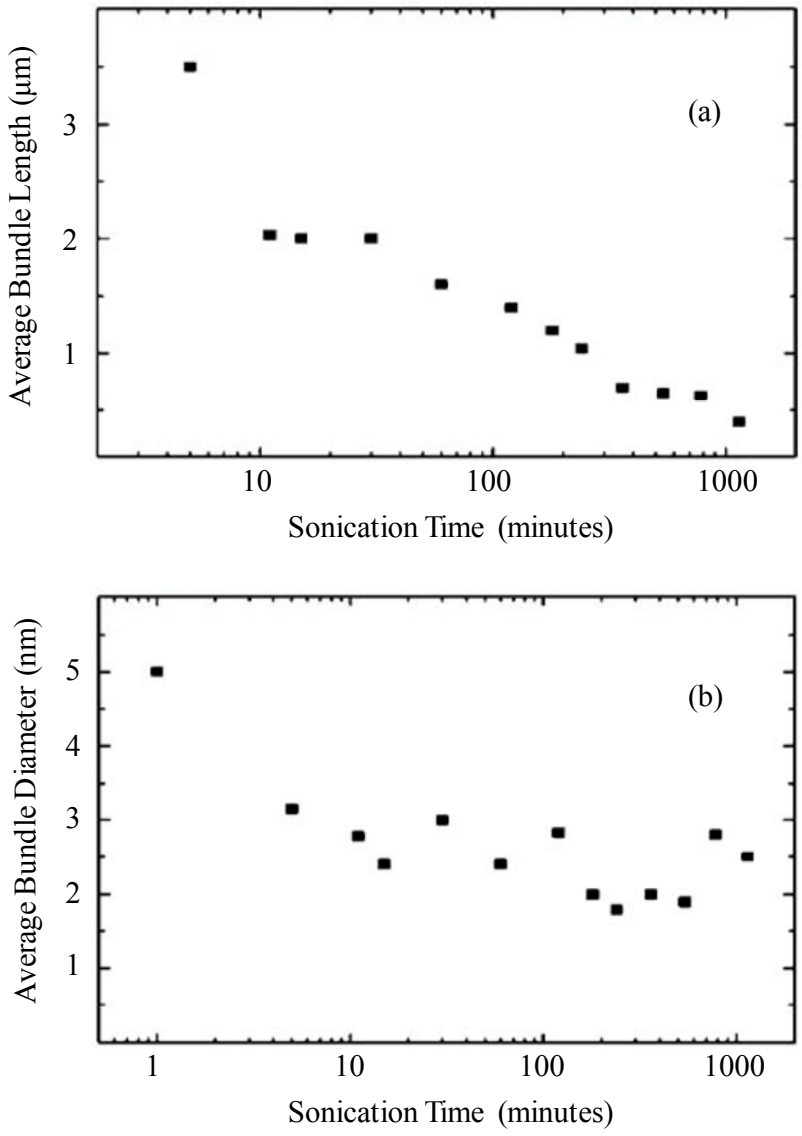


**Figure 2.38.** Plot of the (a) average bundle diameter and (b) average bundle length for various sonication times. (bundle diameter measured from AFM images) Adapted from reference [105].

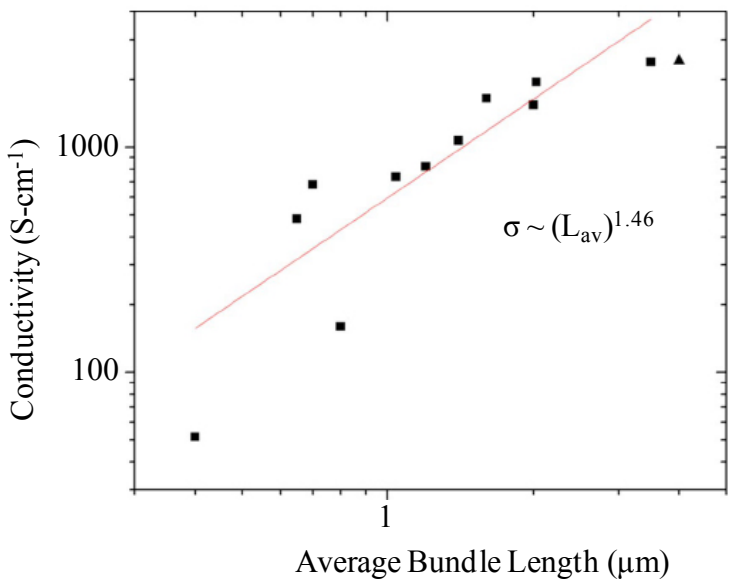


**Figure 2.39.** SWNT film DC conductivity versus average bundle length. Data were fitted to a power law, $\sigma \sim L^{1.46}$. Adapted from reference [105].

The plot shown in Figure 2.39 was used to ascertain the relationship of the film conductivity, $\sigma$, to average bundle length by Hecht et al. The data was fit to a power law relationship of $\sigma \sim L^{1.46}$. Since $R_{sh}$ is proportional to the inverse of $\sigma$ [105], $R_{sh} \sim L^{-1.46}$. These results are consistent with a qualitative understanding of electrical transport in SWNT film. Longer tubes lead to fewer intertube junctions. Since the intratube resistance is much less than the intertube resistance [106], longer tubes should thus result in higher conductive films. Shin et al. [107] examined the effect of nanotube diameter and film conductivity as shown in Figure 2.40. The data was fitted to suggest a power law relationship of $\sigma \sim D^{-1.613}$ or $R_{sh} \sim D^{1.613}$.

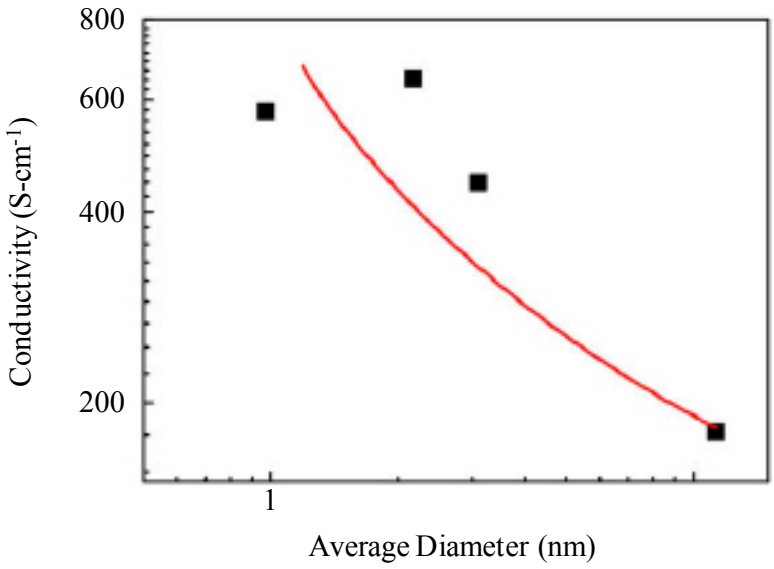


**Figure 2.40.** SWNT film DC conductivity versus average bundle diameter. Adapted from reference [107].

These results provide insight into the impact of mechanical sonication on $R_{sh}$. As can be determined from Figure 2.38 in regard to the suggested correlations of $R_{sh}$ with $D$ and $L$, mechanical sonication yielded two competing effects. Increased sonication time generated smaller diameter bundles which, in turn, should decrease $R_{sh}$. On the other hand, increased sonication time also cut SWNTs into shorter lengths which should increase $R_{sh}$. Therefore, an optimal sonication procedure must be determined that provides sufficient mechanical energy to yield small diameter bundles while not drastically reducing the average SWNT length. For the SWNTs studied in Figure 2.38, a sonication time between 2 to 5 minutes would likely be optimal.

2.5.3.3. SWNT Film Fabrication Impact on $R_{sh}$

Because different research groups use SWNTs produced from different suppliers and/or synthesis methods, much caution must be used when comparing $R_{sh}$ of films produced by different research groups in the literature. A spurious relationship between fabrication method and $R_{sh}$ could easily be made when the actual cause of $R_{sh}$ variation is due to the initial electrical properties of the SWNT batch. De Andrade et al. [94] compared several solution processed SWNT film deposition methods with regard to electrical conduction. All films were produced by the same research group, which provided credibility to the comparison of multi-fabrication methods. SWNTs were deposited onto quartz substrates via dip-coating (DC), vacuum filtration method (FM), spray-coating (SC) and electrophoretic deposition (ED). The results of their study are summarized in Figure 2.41. Between SC, FM, and ED there was no observable difference in $R_{sh}$ as a function of transmittance at 550 nm. However, they observed $R_{sh}$ to be an order of magnitude lower for DC networks. The better conductivity of the DC film was attributed to the fact that DC processing results in smooth networks (low $R_a$) with relatively aligned nanotubes, such that conductivity is enhanced in the direction of alignment [94]. However, it must be noted that the $R_{sh}$ of FM produced films of ca. 1000 $\Omega$-sq$^{-1}$ is significantly higher than other state of the art FM films discussed in 2.4.2.2.6 (i.e. 120 and 250 $\Omega$-sq$^{-1}$ at 80% transmittance). While not invalidating their results, the considerable increase in $R_{sh}$ above what is observed in the current literature suggests interpretational caution be observed and future supporting references and/or research be used to corroborate.

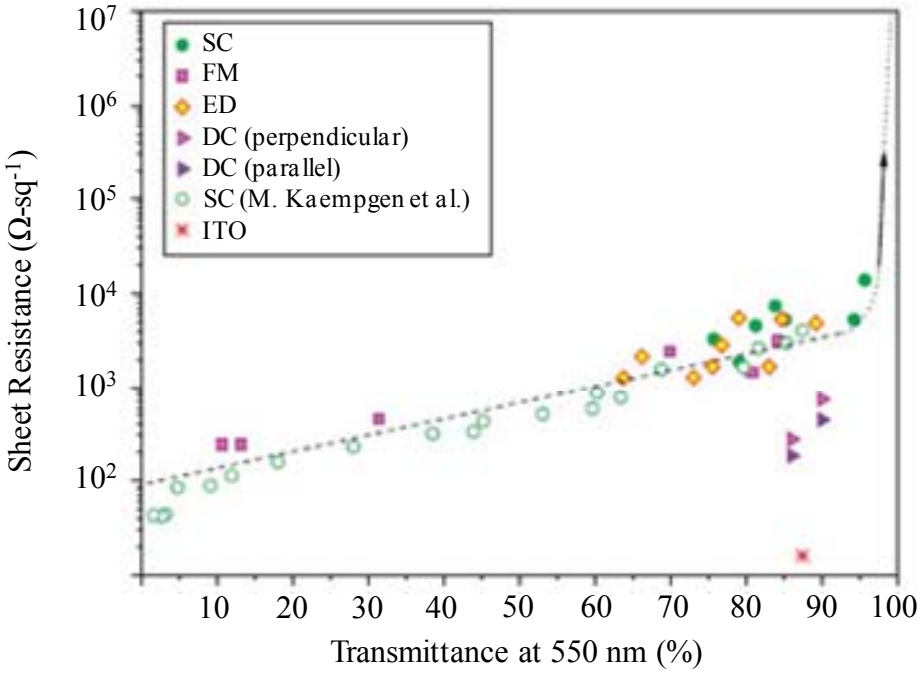


**Figure 2.41.** $R_{sh}$ versus transmittance at 550 nm of several SWNTs films prepared through different techniques. Commercial ITO is shown as a reference. Adapted from reference [94].

2.5.3.4. Post Deposition Processing Impact on $R_{sh}$

To enhance the conductivity of SWNT films while retaining high transmittance, Zhang et al. [80] carried out chemical doping using thionyl chloride ($SOCl_2$). The SWNT film was immersed in $SOCl_2$ for 12 hours followed by drying in nitrogen flow. After $SOCl_2$ treatment, $R_{sh}$ decreased by a factor of 2.4 to 160 Ω-sq$^{-1}$ with a transmittance of 87% at 550 nm. The transmittance spectra of pristine and $SOCl_2$ treated films is shown in Figure 2.42. Only a slight decrease in transmittance due to treatment is observed in the wavelength range of 300 - 400 nm.

The SWNTs used in the films studied by Zhang et al. were purchased with high levels (4-6 atomic %) of carboxylic acid groups covalently bonded to the SWNT sidewalls and ends. Upon immersion in $SOCl_2$, the carboxylic acids were substituted with more electronegative acyl chloride groups [24, 97, 108] as illustrated in Figure 2.43. The acyl chlorides withdrew electrons from the SWNT valence band to p-dope the SWNTs such that increased electrical conductivity was achieved.

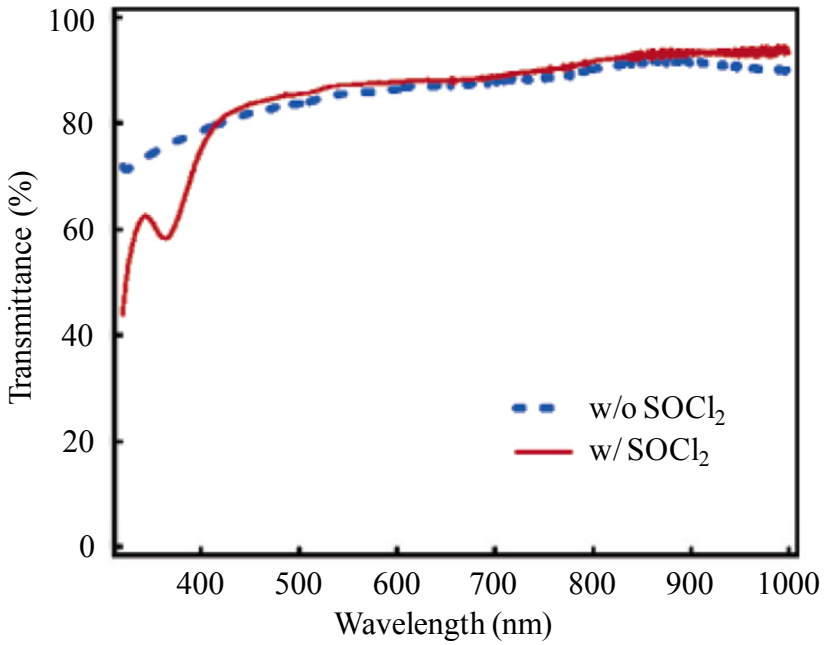


**Figure 2.42.** Transmittance spectra of a pristine (dashed line) and a $SOCl_2$ treated (solid line) SWNT film. Adapted from reference [80].

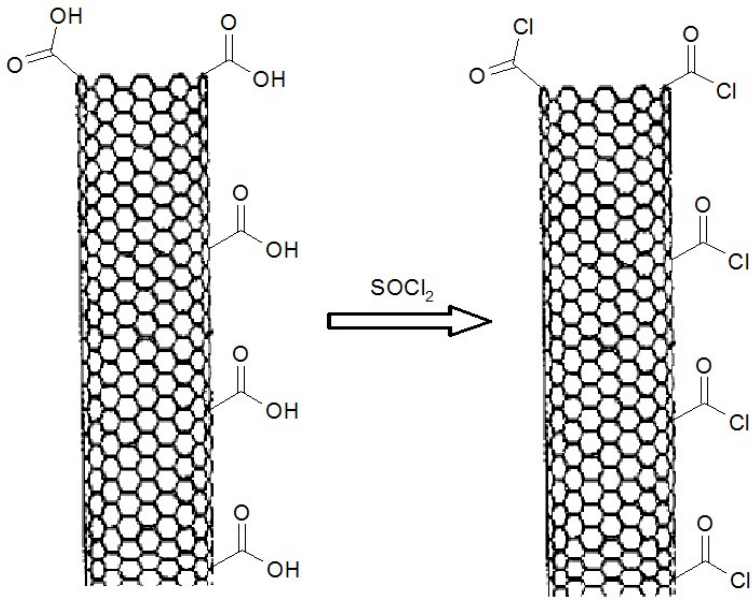


**Figure 2.43.** Nucleophilic substitution of carboxylic acid groups on the sidewalls and tips of the SWNT with acyl chlorides via chemical treatment with $SOCl_2$.

Via immersion in 12 M $HNO_3$ for 60 minutes, Geng et al. [109] increased the conductivity of transparent SWNT films by a factor of 2.5 to yield SWNT films with $R_{sh}$ of ~ 40 Ω-sq$^{-1}$ and 70 Ω-sq$^{-1}$ and transmittances of 70% and 80%, respectively. These optoelectronic properties represent state of the art $R_{sh}$ and corresponding transmittance. The authors attribute the conductivity enhancement to removal of residual surfactant (SDS) used to disperse the SWNTs in solutions. While copious amounts of water are often used to wash SWNT films after vacuum filtration, X-ray photoelectron spectroscopy (XPS) revealed non-negligible amounts of sodium in the film after fabrication, thus suggesting that all of the SDS was not fully removed. Because of its insulating nature, residual SDS on the surface of the SWNTs would limit tube-tube contact and thereby significantly increase the intertube junction resistance to electronic

conduction. After $HNO_3$ treatment, all traces of sodium were removed. Thus, with enhanced intertube electrical contact, the overall conductivity of the film is thereby improved. In addition, they suggest that $HNO_3$ treatment also results in the densification of the film.

Of importance in the study by Geng et al. [109] is their determination that the electrical enhancement was strictly a function of film densification and SDS removal. It was specifically commented that there was "little influence from the chemical-doping effect" and "no significant doping effect was observed". This is in contrast with other reports that suggest the conductivity enhancement achieved after $HNO_3$ treatment is in part attributed to p-doping of the SWNTs due to the highly oxidative nature of $HNO_3$ and $NO_x$ residuals intercalated within the SWNT network [97, 110-113]. Evidence of $HNO_3$ doping can clearly be observed in SWNT films by the bleaching of absorbance peaks due to energy transitions at the first and second van Hove singularities in semiconducting SWNTs, labeled as S1 and S2, respectively, as shown by Hennrich et al. in Figure 2.44 [113].

In the opinion of this author, both communities of thought are likely correct. Removal of residual SDS would surely reduce the intertube electrical resistance of SWNT films. However, it must be noted that the conventional wavelength range used to present the optical properties of SWNT films used by Geng et al. [113] do not include the near-IR spectrum that is seen in Figure 2.44. The optical spectrum presented by Geng et al. (Figure 2.45) only extends to 800 nm (12,500 $cm^{-1}$). Therefore, this author cannot conclude that no p-doping occurs in those SWNTs as suggested.

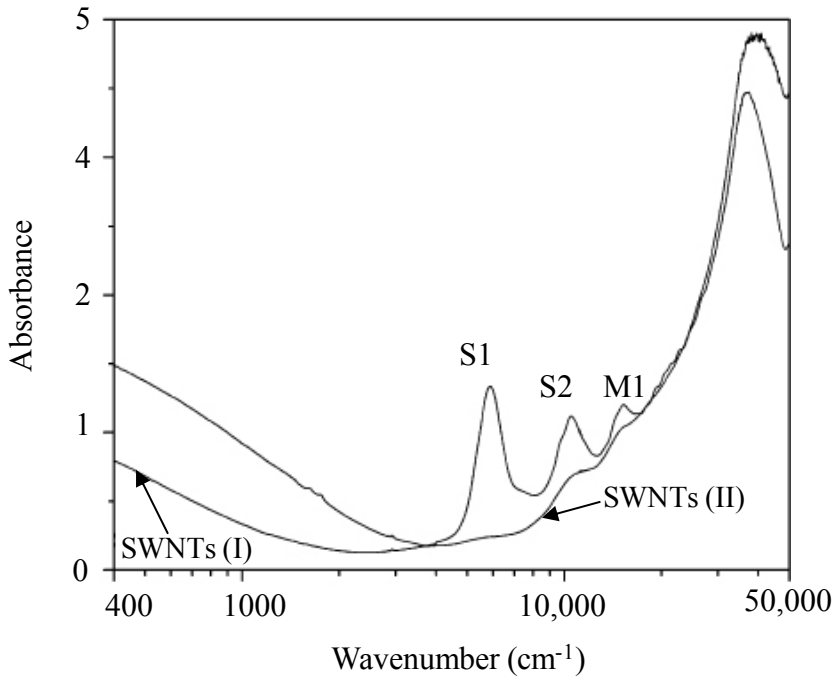


**Figure 2.44.** Far-IR to UV spectra of reference film (SWNTs (I)) comprised of SWNTs with no chemical treatment and $HNO_3$ treated SWNTs (SWNTs (II)). Taken from reference [113].

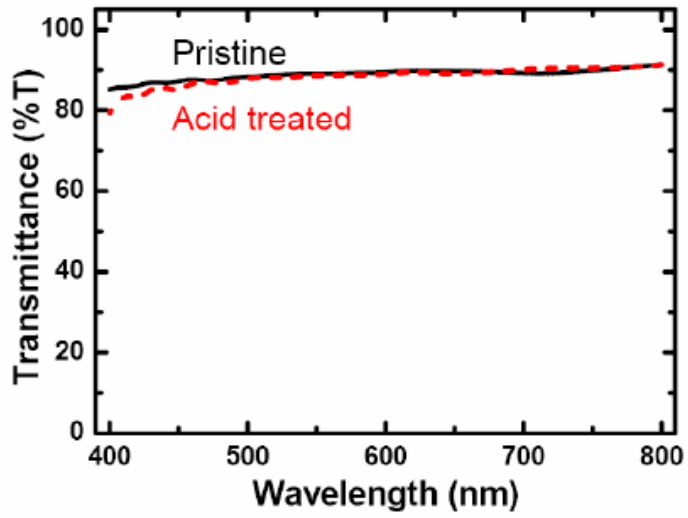


**Figure 2.45.** Transmittance spectra of a pristine (solid line) and a $HNO_3$ treated (dashed line) SWNT film. Adapted from reference [109].

2.5.3.5. SWNT Film Fabrication Impact on Film Roughness

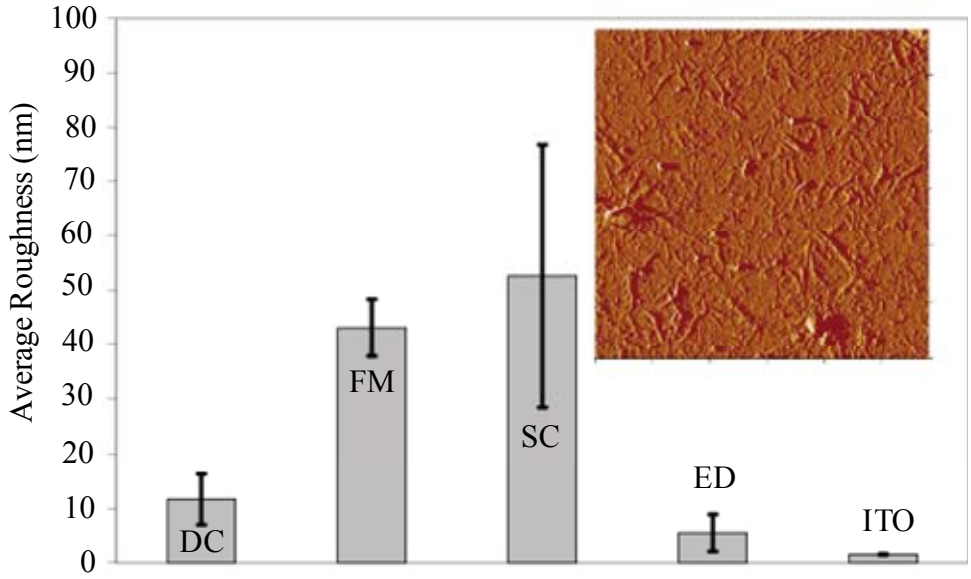


**Figure 2.46.** Comparison of the roughness of SWNT films prepared by different fabrication techniques. Commercially available ITO is shown for comparison. Inset: Micrograph of SWNT film prepared by dip-coating (picture size = 210.25 $\mu m^2$). Taken from reference [94].

De Andrade et al. [94] compared several solution processed SWNT film deposition methods with regards to surface roughness. SWNTs were deposited onto quartz substrates via dip-coating (DC), vacuum filtration method (FM), spray-coating (SC) and electrophoretic deposition (ED). The average roughnesses of the prepared SWNT films are summarized in Figure 2.46 (for each process more than 10 films were analyzed). Films prepared by ED were the most homogenously smooth films followed by DC exhibiting average roughness values around 10 nm. While not as smooth as ITO, ED and DC films were significantly smoother than films fabricated via vacuum filtration

and spray coating. However, it must be noted that the $R_a$ of FM produced films of ca. 40 is significantly higher than the rms roughness of 12 nm presented by Aguirre et al. [96]. While not invalidating their results, the considerable increase in roughness above what is observed in the literature suggests interpretational caution be observed and future supporting references and/or research be used to corroborate.

### 2.6. Progress in the Separation of Metallic and Semiconducting SWNTs

In order to fully exploit the electrical properties of SWNTs in conductive films, networks of monodisperse SWNTs (i.e. only metallic or only semiconducting) are desired. In this manner, the electronic homogeneity of the network can be leveraged to provide superior electrical behavior. Hetereogeneous networks must overcome the significant barriers to electronic interactions that semiconducting and metallic SWNTs have between each other [106]. While research is ongoing in methods to batch produce SWNTs of one electronic type, a SWNT production solution has yet to be achieved. Also, it has been speculated that specific chiral growth of SWNTs may not be possible because of stochastic diameter variations during SWNT growth [114]. On the other hand, other methods have been attempted to achieve monodisperse batches of either semiconducting or metallic SWNTs. These methods include chromatography [115], electrophoretic separation [116], selective destruction [117], selective chemistry [118, 119], and ultracentrifugation [120]. Separation by ultracentrifugation is the most promising and has achieved commercialization status (NanoIntegris, Inc.). In this method, a density gradient is initially formed in the centrifuge tube prior to surfactant encapsulated SWNT loading. Because surfactant encapsulated SWNTs have buoyant

densities that increase with SWNT diameter [121], during ultracentrifugation, the SWNTs sediment through the density gradient to the point where the SWNT density matches the density of the surrounding medium. The net result is that layers of SWNTs will form in the centrifuge tube of varying buoyant density [114]. This process is illustrated in Figure 2.47.

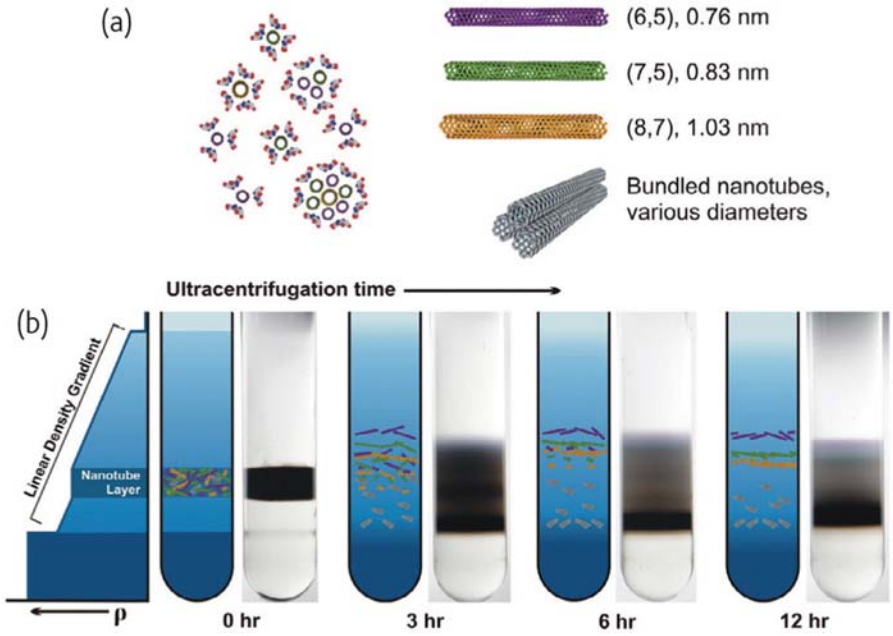


**Figure 2.47.** Illustration of density gradient ultracentrifugation (DGU) process. (a) Schematic of surfactant-encapsulated SWNTs. Chiral indices and corresponding diameters of sample SWNTs are identified. (b) Process illustration with schematic and photographs of ultracentrifuge tube at different points during the DGU process. Taken from reference [121].

## 2.7. Conclusion

Important background information on the present status of SWNT films and theoretical development of the electronic structure of carbon nanotubes were presented in this chapter. A summary of important topics covered in this chapter is as follows

- Sections 2.2 – 2.3 provided pertinent background information on the electronic properties of SWNTs.
- Section 2.4 provided an overview of the three most common methods for the synthesis of SWNTs.
- Section 2.5 provided a literature review of state of the art in the fabrication of SWNT films to demonstrate the current viability of nanotube networks as a transparent electrode and to serve as a basis for the scientific contribution made in this dissertation. SWNT films were shown to demonstrate excellent mechanical stability, rms surface roughness as low as 3 nm, and $R_{sh}$ values as low as 70 Ω-sq$^{-1}$ at 80% transmittance. With an $R_{sh}$ of ca. 60 Ω-sq$^{-1}$ at 80% transmittance for commercially available ITO on PET, current SWNT film state of the art are already competitive with the optoelectronic properties of ITO deposited on flexible substrates. Furthermore, the mechanical stability of SWNT films was shown to far exceed that of ITO.
- Section 2.6 provided a review of current progress in the separation of metallic and semiconducting SWNTs.

**Outstanding Research Issues**

While the current state of the art in SWNT transparent electrodes exhibit significant capability and future potential, a full understanding of the optoelectronic

behavior of SWNT networks extending far beyond the laboratory based "Edisonian approach" has yet to be realized in the SWNT film research community. This is illustrated in how the effect of post-deposition processing is a point of contest in the literature (section 2.5.3.4). Chapter 4 in this dissertation will explicitly address how the electrical conductivity of SWNT electrodes is enhanced and sustained through post-deposition processing. To best elucidate the impact of post-deposition processing, chapter 4 will evaluate the optical and electrical properties of SWNT films from the perspective of the electronic structure of individual SWNTs provided in sections 2.2 – 2.3 of this chapter. Also, given the recent success in the separation of metallic and semiconducting SWNTs by research groups such as Prof. Mark Hersam's group at Northwestern University, an investigation of the impact of using SWNT films of homogeneous electronic type is warranted and is presented in chapter 5. Finally, because the SWNT films discussed in this chapter show significant application potential as a transparent electrode in organic photovoltaics, chapter 6 will discuss the electrical nature of the interfacial contact between thin SWNT films and the metallic grid contacts typically utilized in system level photovoltaic operation.

# CHAPTER 3: BASELINE CHARACTERIZATION OF SWNT NETWORKS

## 3.1. Introduction

Chapter 2 provided a review of state of the art SWNT films that exhibited excellent mechanical stability, rms surface roughness as low as 3 nm, and $R_{sh}$ values as low as 70 Ω-sq$^{-1}$ at 80% transmittance. These properties well position SWNT networks as a viable potential substitute for ITO on transparent substrates, with current state of the art already competitive with ITO deposited on flexible substrates. Chapter 2 also posited important questions remaining in SWNT film research community regarding: (1) how the conductivity of SWNT electrodes impacted, enhanced, and sustained through post-deposition processing, (2) what is the impact of using SWNT films of homogeneous electronic type, and (3) what is the electrical nature of the interfacial contact between thin SWNT films and metallic grid contacts. These questions will be addressed by the research contribution of this dissertation in chapters 4 – 6. However, this chapter will first provide a technical basis upon which subsequent chapters can build. In particular, this chapter will present the methodology used to fabricate SWNT films investigated later. Also, the baseline properties of SWNT films will be evaluated to provide a reference point for comparison with current state of the art and future film processing evaluated in chapters 4 – 6.

## 3.2. SWNT Type

Arc-discharge synthesized SWNTs were purchased in powder form from Carbon Solutions, Inc. (Item #: P3 SWNT). P3 SWNTs (hereafter referenced as SWNTs) are as-

produced SWNTs purified with nitric acid and left in highly functionalized form (4 – 6 atomic % carboxylic acid groups). These SWNTs were utilized due to the high percentage of functional groups that aid in subsequent dispersion and substitutional doping. The metal content (catalyst impurities) of the SWNT powder was quoted as 5-10 weight % and the carbonaceous purity was > 90%. Carbonaceous purity describes the ratio of SWNTs as a percent of all carbonaceous materials, which include amorphous carbon and graphitic nanoparticles. The mean length and diameter of these SWNTs are 1 μm and 1.4 nm, respectively.

## 3.3. SWNT Film Fabrication

The process used in this study to fabricate SWNT film electrodes consisted of an augmented vacuum filtration and subsequent film transfer method first presented by Wu et al. [77] and described in chapter 2. While not as suitable for manufacturing scalability as the spray coating method discussed in chapter 2, this process was selected because of the ease in which SWNT films of consistent surface morphology with controllable thickness could be produced. The details of the augmented method are described below and important steps are illustrated in Figure 3.1.

### 3.3.1. SWNT Film Preparation Process

1. SWNTs in powder form (Figure 3.1a) were added to 0.5 wt % aqueous solutions of sodium dodecyl sulfate (SDS). The concentration of SWNTs was typically 1.1 mg / 2 ml. Then the solution was bath sonicated for 1 hour, followed by centrifugation at 16,000 rpm for 60 minutes. The bath sonicator (VWR 75D) was

operated at 50% for an approximate sonic power of 45 watts. A photograph of the typical SWNT solution after sonication is shown in Figure 3.1b. During centrifugation residual metal catalysts and impurities from the manufacturer and any large undissolved SWNT aggregates and bundles were forced to the bottom of the solution due to centrifugal forces created during the process. The solution was subsequently carefully decanted such that only the top ~80% of the sample was removed for further processing. The remaining bottom ~20% was discarded. The new solution was then sonicated again for 1 hour at 50% power rating and then centrifuged. The second sonication and centrifugation step was used to facilitate SWNT solutions for further processing free of large bundles and impurities. After centrifugation, the top ~80% of the centrifuged solution was again decanted.

2. The concentrated SWNT solution obtained from the previous step was diluted and subsequently vacuum filtered through mixed cellulose ester (MCE) membranes (GE Osmonics) with a diameter of 47 mm and a pore size of 100 nm (Figure 3.1d). In order to promote film formation of homogeneous thickness during the vacuum filtration process, 30 ml was chosen as the minimum volume of SWNT solution filtered. Solutions smaller than 30 ml may result in regions of thick/thin SWNT deposits on the membrane filter. The concentration of the final SWNT solution vacuum filtered was varied according to the desired thickness of the resulting SWNT film. Typically, ~0.3 ml of concentrated SWNT solution from the previous step added to 30 ml of distilled water would result in a film thickness of 20-30 nm. The vacuum filtration setup is pictured in Figure 3.1c. Vacuum was provided via a 1/8 HP vacuum pump.

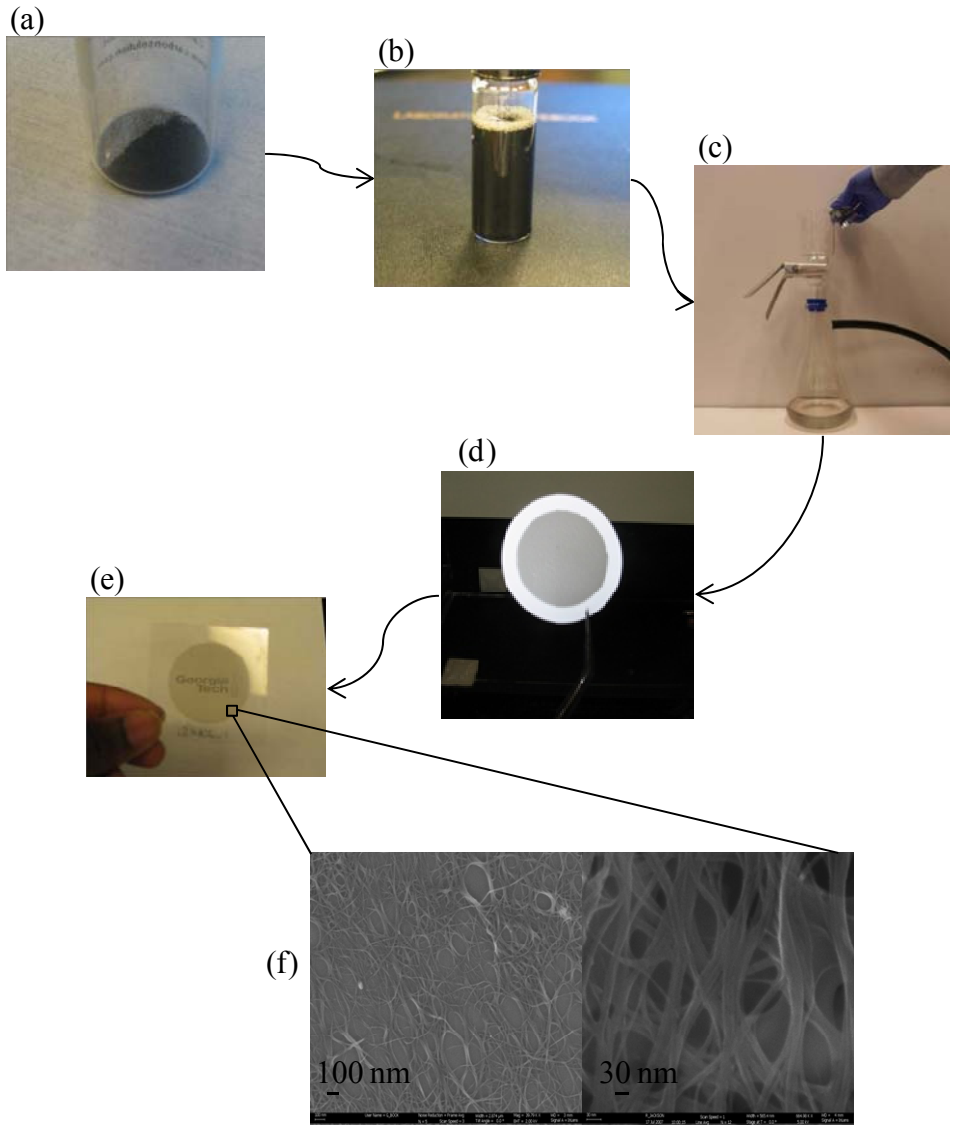


**Figure 3.1.** SWNT film fabrication process. (a) P3-SWNT powders as purchased. (b) Concentrated SWNT solution. (c) Vacuum filtration setup. (d) SWNT film on MCE membrane. e) SWNT film transferred onto PET substrate. (f) Scanning electron microscopy (SEM) images of SWNT film.

3. The SDS surfactant used to facilitate dispersion remains attached to SWNTs after the filtration process. In order to remove the surfactant from the SWNT surface, 40 ml of distilled water was vacuum filtered through the SWNT film as a rinse step.

However, if the water was poured on the SWNT film prior to the van der Waals forces between SWNTs in the network developing, the SWNT network integrity would be compromised resulting in large "swaths" of the SWNT film dislodged from the network. Therefore, after the SWNT solution was filtered, the MCE membrane was removed and heated on a hot plate for ~10 minutes at 80°C to promote van der Waals adhesion of SWNTs and SWNT bundles throughout the nanotube network. Then, the membrane and SWNTs were placed back on the vacuum filtration flask and distilled water was filtered through.

### 3.3.2. SWNT Film Transfer Process

SWNTs on MCE membranes as shown in Figure 3.1d were thoroughly wetted with isopropyl alcohol (IPA) and applied onto transparent substrates. It was necessary to wet the SWNTs on the membrane to promote adhesion to the substrate. IPA was used to wet the SWNTs because of its compatibility with the membrane material and because it evaporates at a lower temperature than water. Once the membrane was placed on the substrate and membrane was allowed to dry, the film was quickly placed on the acetone vapor bath to allow the membrane to begin dissolution. The membrane/SWNT/substrate was placed into 4 sequential acetone baths to dissolve the membrane such that only the SWNT film remained on the substrate. Each acetone bath soaking time was approximately 45 minutes. A SWNT film transferred onto a flexible polyethylene terephthalate (PET) substrate is shown in Figure 3.1e.

## 3.4. SWNT Film Figures of Merit

### 3.4.1. Surface Roughness of SWNT Films

A Dektak 6M stylus profilometer was used to characterize the surface roughness of SWNT films. A total of 29 random line scans of 600 – 1800 μm in length were taken over 8 samples. The mean average roughness, $R_a$, over all samples was 10.48 nm with a standard deviation of 3.47 nm, comparable to the rms roughness of 12 nm observed by Aguirre et al. [96]. An AFM surface scan of a representative film is shown in Figure 3.2. AFM measurements with a Dimension 3100 Nanoscope IV system (Veeco Metrology Group, Santa Barbara, CA) were also made to provide additional film morphology characterization and a 5 μm x 5 μm surface scan of a representative film with a $R_a$ of 9.2 nm is shown in Figure 3.2. As can be seen in the figure, considerable surface roughness exists. The origin of the spikes can likely be attributed to large SWNT bundles, carbonaceous impurities, and/or metal catalysts from the initial SWNT "soot" that were not removed in the centrifugation process described in section 3.3.1. Additionally, impurities such as undissolved MCE membrane, and contamination introduced during the vacuum filtration and subsequent film transfer can contribute to the presence of these spikes. The presence of "spikes" significantly affects the ability to employ these films as electrodes in organic electronics with small active layers as discussed in chapter 2. Therefore it is likely that SWNT films obtained using vacuum filtration and film dissolution will not provide the most feasible approach to large scale production of SWNT electrodes, since Tenent et al. [101] has recently shown the ability to produce SWNT films with rms roughness as low as 3 nm using an ultrasonic spray technique.

(a)

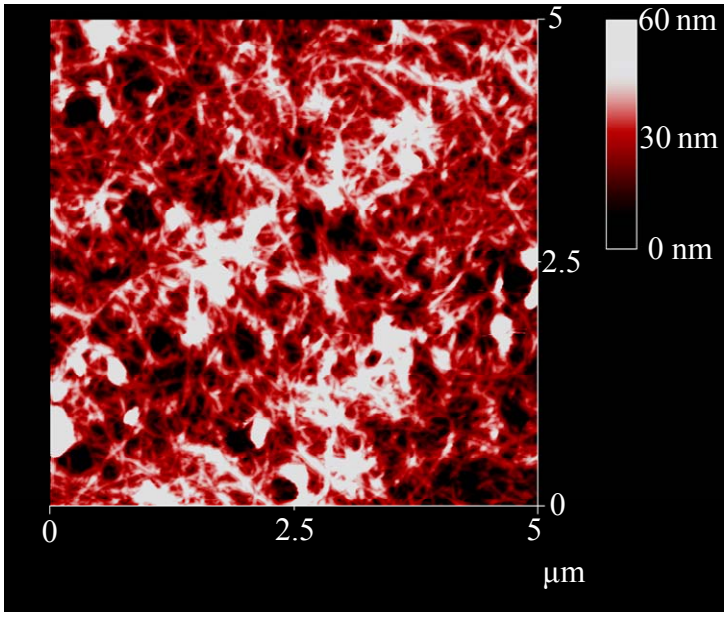


(b)

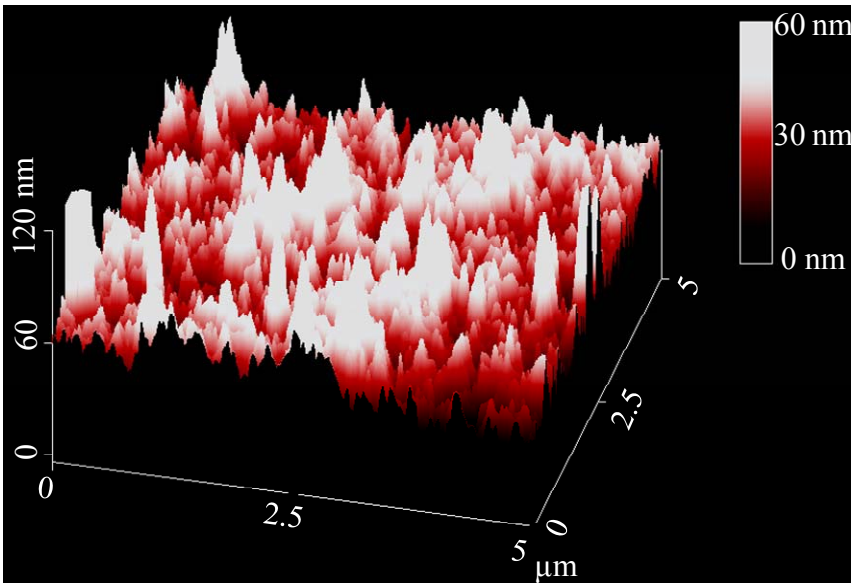


**Figure 3.2.** AFM surface image of sample SWNT film demonstrating film roughness. a) top view (b) surface plot

### 3.4.2. Mechanical Stability of SWNT Films

To evaluate the mechanical stability of SWNT films deposited onto flexible PET, films transferred to PET substrates were attached to mandrels of varying radii and the associated $R_{sh}$ was measured. Mandrels with radii of 20 mm, 10 mm, and 5 mm were used to evaluate films. For comparison, a thin layer of ITO was deposited onto PET substrates via RF sputtering and subsequently tested for mechanical stability. The ITO target used had an $In_2O_3$ : $SnO_2$ percent composition of 90 : 10. A deposition time of 20 minutes at 60 W resulted in an approximate thickness of 350 nm [122]. An Argon flow rate of 26 sccm and pressure of 2.0 mTorr was maintained during the deposition. No substrate heating was applied during deposition. $R_{sh}$ was measured for each bending radii and the results are plotted in Figure 3.3. The equivalent tensile strain, *e*, of each bending radii is shown in the top axis and was calculated using the standard equation for strain:

$$e = \frac{\frac{t}{2}}{r_b + \frac{t}{2}} \tag{3.1}$$

where $t$ and $r_b$ are the thickness and the bending radius, respectively. Since the ITO thickness (0.3 μm) and SWNT film thickness (0.03 μm) were much less than that of the PET substrate with a thickness of 150 μm, $t$ was approximated as the thickness of the PET substrate. Up to 10 mm, neither film demonstrated any adverse response to bending. However, at a bending radius of 5 mm, $R_{sh}$ of the ITO film increased to greater than 30,000 Ω-sq$^{-1}$, while SWNT films exhibited no salient change in $R_{sh}$. The strain at which failure of ITO was observed is consistent with other reported data on the strain at which

ITO fails due to crack propagation [15, 123]. While an appreciable amount of conductivity was returned upon eliminating the bend in the ITO, $R_{sh}$ was still more than 2 orders of magnitude higher than initially recorded. $R_{sh}$ of SWNT film was constant with bending because of the random network properties of the film. As the curvature of the film was increased, SWNTs are free to slide and pivot at interfaces while electrical contact between SWNTs was maintained. As such, none of the initial electrical conduction pathways are broken and mechanical stability was exhibited.

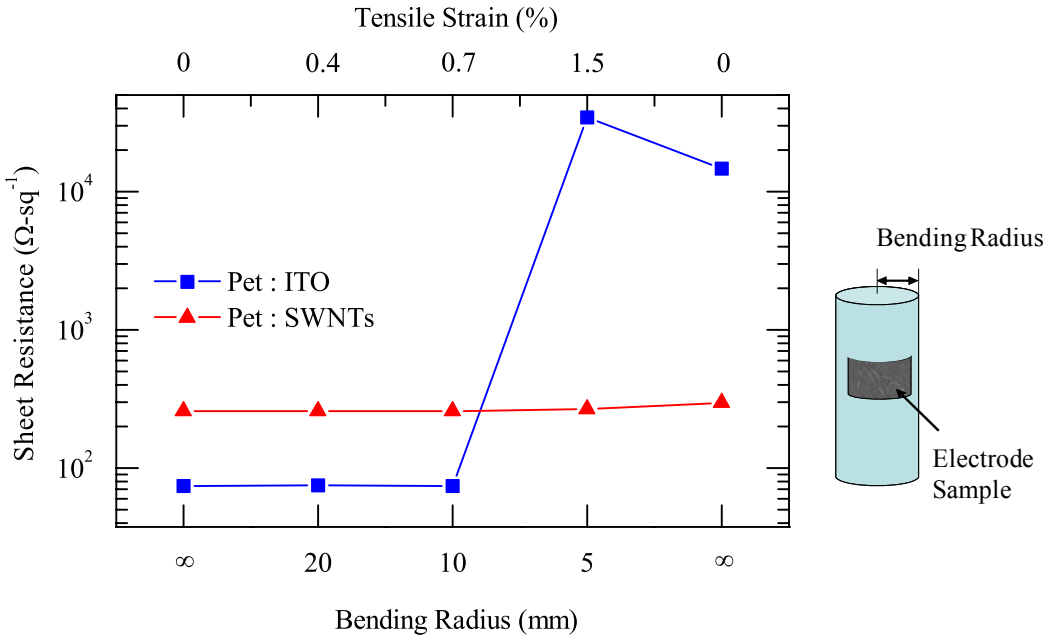


**Figure 3.3.** Mechanical properties of ITO and SWNT films. Sheet resistance is plotted as a function of bending radius. The corresponding strain for each bending radius is shown on the top x-axis. A schematic of the testing apparatus is shown on the right.

### 3.4.3. Optoelectronic Properties of SWNT Films

As previously described, vacuum filtration of SWNT films provides a simple

process for which the film thickness can be controlled. As a result, film transparency and $R_{sh}$ could also be varied in this study. Optical transmittance spectra of sample SWNT films are shown in Figure 3.4. Optical transparency was characterized by measuring the transmittance using a Cary 5E UV-Vis-NIR dual-beam spectrophotometer. The transmittance of the transparent substrate was set as the baseline and subtracted from the optical spectra. Thus, the provided spectra correspond to the transmittance of the SWNT film.

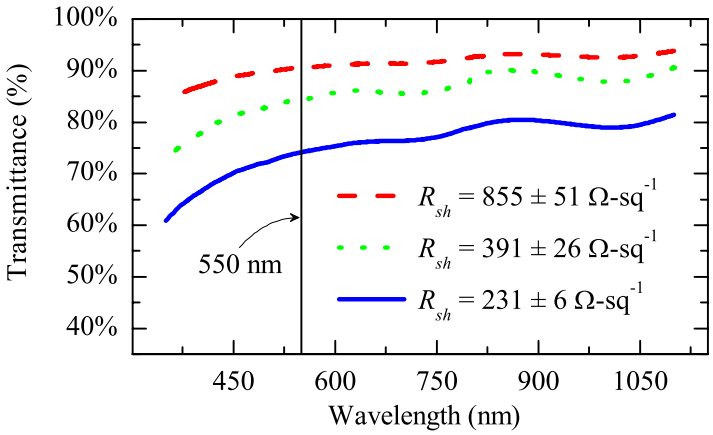


**Figure 3.4.** Transparency in the visible and near infrared spectrum and corresponding $R_{sh}$ for various SWNT films.

For transparent electrode applications in organic electronics, transmittance in the wavelength range of 400 nm to 800 nm is optimal. Therefore, only the wavelength range of 350 nm to 1100 nm is shown in the figure. Percolation theory predicts a critical density (SWNTs per area), or a percolation threshold, such that metallic pathways exists and long range conductivity is established. Prior to reaching the percolation threshold for metallic conduction, conductivity is dominated by semiconducting tubes that comprise

the majority of the SWNT population. Therefore as the density is increased, more metallic tubes contribute to conduction, thereby significantly reducing the sheet resistance, as evidenced between the two most transparent films (91% and 84% transmittance at 550 nm) with sheet resistances of 855 ± 51 Ω-sq$^{-1}$ and 391 ± 26 Ω-sq$^{-1}$ respectively. However, beyond the percolation threshold, increasing SWNT density only adds more metallic pathways in parallel with existing metallic pathways (i.e. parallel resistor model). These conducting paths still contribute to lower sheet resistance, but do not provide as substantial a decrease, as seen in the decrease from 391 ± 26 Ω-sq$^{-1}$ to 231 ± 6 Ω-sq$^{-1}$ for the films with transmittances at 550 nm of 84% and 74% respectively.

The Transfer Length Method (TLM) [124] was used to determine $R_{sh}$ of the SWNT films in this dissertation. Silver metal was e-beam deposited on the films through a shadow mask to define fine metal lines on the SWNT films. The spacing between the lines ($d_i$) was linearly increased from 0.9 to 6.9 mm. The sheet resistance, $R_{sh}$, was derived from the slope, $m$, of the plot of the two-point resistance between adjacent lines versus line spacing using:

$$m = \frac{R_{sh}}{W} \tag{3.2}$$

where $W$ is the width of the metal line and was equal to 1 cm for all lines. The structure is illustrated in Figure 3.5.

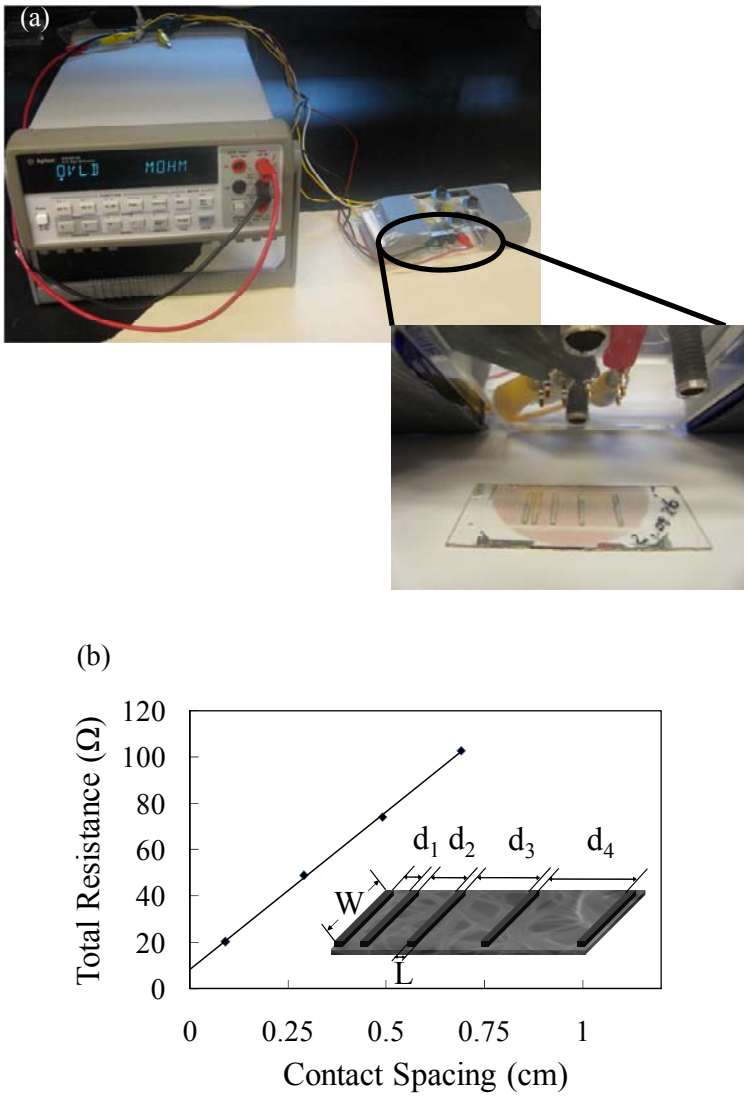


**Figure 3.5.** (a) Photograph of testing apparatus. (b) Application of Transfer Length Method used to determine $R_{sh}$ in SWNT films. Total resistance is plotted versus contact spacings of 0.9 mm, 2.9 mm, 4.9 mm, and 6.9 mm. Fitted least squares line is used to determine the slope, $m$. Inset illustrates metal lines deposited on SWNT films.

The statistical variation of $R_{sh}$ between films of similar transparency was determined by analyzing 12 SWNT films produced between April 1, 2008 and June 26,

2008. The mean $R_{sh}$ of these films was 332 ± 49 Ω-sq$^{-1}$ with a transmittance of 80 ± 1.7% at 550 nm.

### 3.4.4. Error Analysis of $R_{sh}$ Determined from TLM

Using a general error propagation approach, the relative uncertainty for $R_{sh}$ can be found by differentiating Eq. 3.2 [125].

$$\frac{\Delta R_{sh}}{R_{sh}} \cong m\frac{\Delta W}{W} + W\frac{\Delta m}{m} \tag{3.3}$$

where $\Delta R_{sh}$, $\Delta W$, and $\Delta m$ denote the error of $R_{sh}$, $W$, and $m$ respectively. Because the fine metal lines were deposited via ebeam deposition through a shadow mask of consistent dimensions, $\Delta W$ was considered to be negligible. For a sample size of 23 SWNT films the average $m$ was found to be 333 Ω-(sq*cm)$^{-1}$ with $\Delta m$ = 10.1 Ω-(sq*cm)$^{-1}$. Therefore, the relative error for $R_{sh}$ is equal to 3%.

### 3.4.5. Sources of Variability in SWNT Films

Due to the considerable number of processing steps involved in the fabrication of SWNT films (section 3.3), sources of variability exist that can impact the capability to repeatedly produce SWNT networks of similar transmittance and/or sheet resistance. For example, the concentration of the SWNT solution that is vacuum filtered through the membrane, as described in section 3.3.1, can vary based on the amount of SWNTs in large bundles of high density that are removed via centrifugation. The variance in the decanted solution from the centrifuge process is attributed largely to the effectiveness of

the prior sonication step in separating SWNT bundles into individual nanotubes and the degree in which re-aggregation of individual SWNTs into bundles occurs. Variability is also introduced during the vacuum filtration process. Variance in the pore size of the membrane filters can result in differing amounts of SWNTs remaining on the film after the vacuum process. In addition, as the diameter of the SWNTs and SWNT bundles increases due to re-aggregation or ineffective sonication, the amount of SWNTs that remain on the membrane filter will increase as well; thus providing further variation in the filtration process. The SWNT diameter distribution also yields variance in the optical absorption of film, since larger SWNT bundles decrease the void fraction of the nanotube network and increase the overall optical absorption for a given film thickness.

## 3.5. Conclusion

This chapter provides a description of the process used to fabricate SWNT films and a baseline characterization of "as-made" SWNT films (i.e. no augmentation made to film or fabrication process to improve optoelectronic performance) studied and presented hereafter in this report. Similar to state of the art SWNT films presented in chapter 2, the as-made film evaluated in this chapter exhibited no salient electrical degradation with mechanical strain due to bending. Also, with an average $R_{sh}$ of 332 Ω-sq$^{-1}$ at 80% transmittance, the optoelectronic properties of as-made films are within the range of typical $R_{sh}$ values reported in the literature (250 Ω-sq$^{-1}$ – 400 Ω-sq$^{-1}$ with transmittances at 550 nm of 80 – 85%) [80, 96, 97]. Therefore, the as-made films discussed in this chapter provide a good reference point for subsequent chapters (chapters 4 – 6) that will enhance the current understanding of SWNT networks with regard to their application as a transparent electrode surrogate for ITO.

# CHAPTER 4: ENHANCED ELECTRICAL CONDUCTION IN SWNT FILMS

## 4.1. Introduction

The SWNT films presented in the chapter 2 and 3 demonstrated significant optoelectronic potential, with state of the art sheet resistance, $R_{sh}$, values as low as 70 Ω-sq$^{-1}$ at 80% transmittance. However, as discussed in chapter 2, the origin of such improvement over standard SWNT films is a point of contention and ambiguity in the literature. To enable further progress in developing these electrodes, an understanding beyond the laboratory based "Edisonian approach" must be developed so that the mechanisms by which such results are derived are correctly understood. As a better comprehension is developed within the research community of how high electrical conductivity is achieved in SWNT films, realization of the full optoelectronic potential of SWNT networks is achievable. As such, it is the goal of this chapter to communicate a lucid understanding of conduction in SWNT films and the methods by which improvements are achieved. First, a qualitative understanding of electrical conduction in SWNT film is presented to serve as a basis for further discussion. Next, multiple modes of experimental characterization are corroborated with theoretical SWNT electronic structure to clearly depict the impact of charge carrier doping on the optical and electronic properties of SWNT films. Finally, the stability of such enhancements is investigated and a method to sustain improvements is presented.

## 4.2. Electrical Conduction in SWNT films

Electrical conduction in SWNT films can be modeled as a network of 1-D conducting sticks [63] as shown in Figure 2.13 in chapter 2. Appreciable conduction is obtained when a percolation threshold is achieved, such that sufficient nanotubes are present in the film to form a continuous conducting pathway. As the density of nanotubes is increased beyond the percolation threshold, more parallel conducting paths are created. The addition of more conducting paths reduces the overall resistance to current flow, as would be expected in a conventional parallel resistor model. The resistance along a particular conduction path, $R_{path}$, in the film can be understood with the simple model:

$$R_{path} = R_{SWNT-SWNT} + R_{SWNT} \tag{4.1}$$

where $R_{SWNT}$ and $R_{SWNT\text{-}SWNT}$ are the intratube and intertube SWNT resistances, respectively. Because typical SWNT films contain a mixture of 33% metallic and 66% semiconducting carbon nanotubes, the majority of 1-D nanotube conducting sticks in the percolation model have significant intrinsic electrical barriers to conduction. $R_{SWNT}$ for intrinsic semiconducting SWNTs is much higher than $R_{SWNT}$ for metallic SWNTs. Also, $R_{SWNT\text{-}SWNT}$ for metallic-semiconducting SWNT intertube contacts has been experimentally shown to be two orders of magnitude higher than contacts for semiconducting-semiconducting and metallic-metallic SWNT interaction [106]. As such, the best possible path for electrical conduction in an intrinsic SWNT network would consist of all metallic SWNTs. Therefore, the relative high sheet

resistances presented in Chapter 3 are expected, given that only one third of SWNTs in the random network are intrinsically metallic. Consequently, the possible 1-D, high conduction pathways which exist in SWNT network are limited.

In order to lower $R_{sh}$ for SWNT films in the context of a parallel resistor model of 1-D conducting sticks, either more parallel resistors of similar $R_{path}$ can be added to the network, or $R_{path}$ for the existing pathways can be decreased. In Chapter 3, more parallel resistors were added by increasing the total density of nanotubes in the network. However, to favorably compete with ITO as a transparent electrode, both methods of improvement must be strategically employed in order to realize a highly conductive transparent electrode.

It has been shown that the conductivity, $\sigma$, of SWNT films can be considerably enhanced through chemical treatment that results in the addition of charge carriers either in the form of hole or electron doping [108, 126, 127]. $R_{SWNT\text{-}SWNT}$ is limited by a tunneling barrier between nanotubes in electrical contact. As the density of charge carriers, $n$, is increased in the SWNT film, local electric fields are created at SWNT interfaces that can modify the shape and height of tunnel barriers [128]. In fact, the hole doping process used later in this chapter has been shown to increase tunneling probability in SWNT films, thereby resulting in lower $R_{SWNT\text{-}SWNT}$ [129]. Also, $\sigma$ is related to the density of free charge carriers in a material by:

$$\sigma = ne\mu \qquad 4.2$$

where $n$, $e$, and $\mu$ are the charge carrier density, electronic charge, and charge

mobility, respectively. Sufficient degenerate doping can result in the metallization of semi-conducting tubes, thus electrically activating previously non-conducting, semiconducting pathways.

For the development of electrode materials for organic electronic applications, p-doping of the SWNT films is the preferred treatment, since holes are collected/injected at the electrode and organic material interface. $HNO_3$ and $SOCl_2$ have been shown to significantly p-dope individual SWNTs as evidenced through the effective pinning of the Fermi Level inside the valence band [108, 112, 113]. As shown in Figure. 4.1a, $HNO_3$ molecules and/or $NO_x$ residues dope the SWNTs by intercalation within the network [111]. As illustrated in Fig. 4.1b, exposure to $SOCl_2$ results in the nucleophilic substitution of carboxylic acid groups on the sidewalls and tips of the SWNT with more electronegative acyl chlorides [24, 108]. Since chemical treatment with $HNO_3$ and $SOCl_2$ can p-dope individual SWNTs through different mechanisms, it is expected that both processes can be utilized to achieve optimal electrical behavior.

To evaluate impact of doping on the optoelectronic properties of SWNT film, as-made SWNT films will be characterized and compared with chemically treated, p-doped SWNT films in the section to follow.

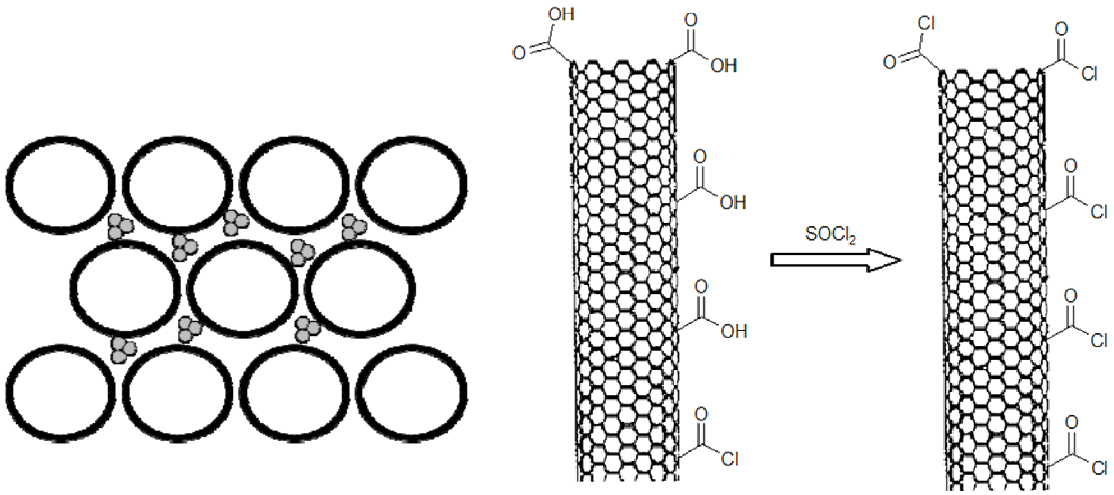


**Figure 4.1.** (a) Simple space filling model of intercalated $HNO_3$ molecules within a SWNT unit cell. (b) Nucleophilic substitution of carboxylic acid groups on the sidewalls and tips of the SWNT with acyl chlorides via chemical treatment with $SOCl_2$.

## 4.3. Impact of Doping on SWNT Film Electrical Properties

### 4.3.1. Optical and Electrical Characterization of As-made and Doped SWNT Films

As-made transparent SWNT films were prepared as described in Chapter 3. Hole doping of the SWNT films through chemical treatment was performed by immersing the films into solution for 30 - 45 minutes. These doping times were utilized since additional testing revealed no salient difference in the electrical properties of the films with increased immersion times up to 12 hours. After immersion in the acid, the films were carefully air blown dry. Films were subsequently heated in an oven at 80°C for up to 10 minutes. The heating step was proven effective to remove the optically visible haze that formed on the substrate (due

to $SOCl_2$ treatment), thereby eliminating optical transmission losses due to doping.

Sheet resistance was measured approximately four hours after doping treatment due to the time dedicated to drying the film and the subsequent deposition of silver lines. In addition to measuring the sheet resistance of the transparent electrode, the optical transparency was characterized by measuring the transmittance using a Cary 5E UV-Vis-NIR dual-beam spectrophotometer.

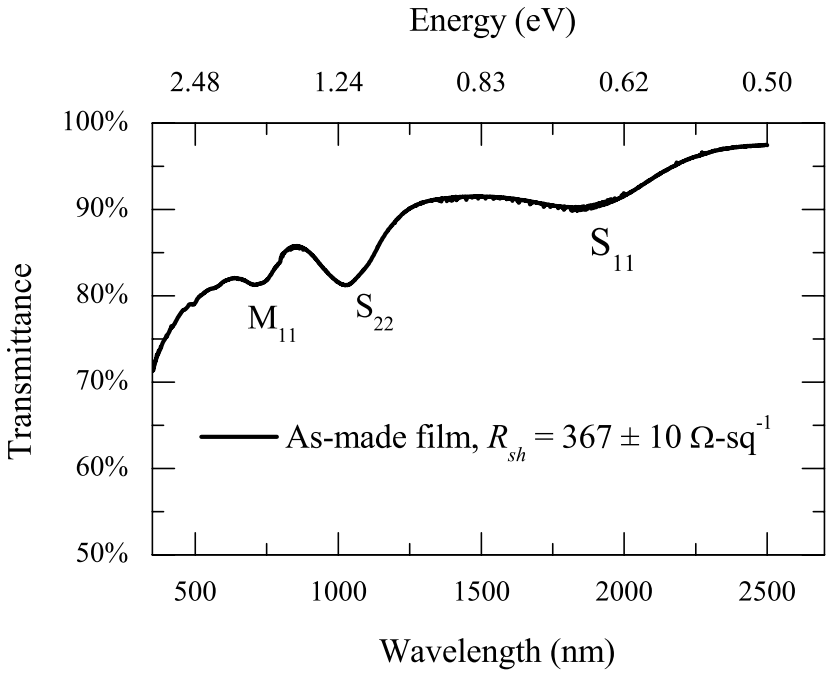


**Figure 4.2.** Optical transmittance of an as-made SWNT film.

Fundamental information on the specific properties of individual nanotubes and bundles can be found if a broader spectrum is analyzed beyond the typical wavelength range of 350 – 1100 nm as shown in Chapter 3. Shown in Figure 4.2 is the optical transmittance of an as-made SWNT film. The transmittance is plotted as a function of wavelength as was previously shown in Chapter 3. However, the wavelength range is

extended to 2500 nm, thus encompassing more of the near infrared spectrum (i.e. 750 – 2500 nm).

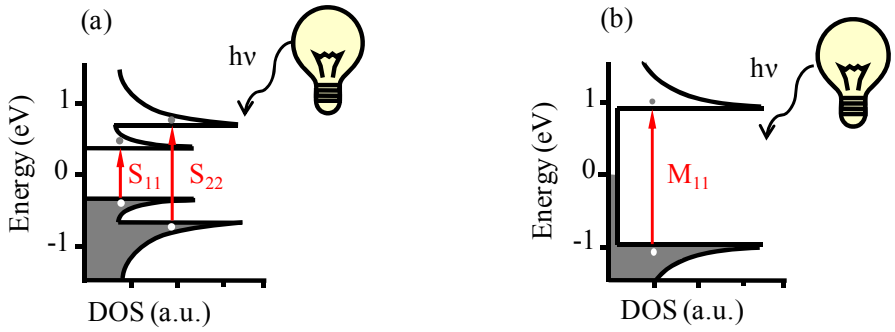


**Figure 4.3.** (a) Schematic diagram illustrating absorption at van Hove singularities in in semiconducting SWNTs. (b) Schematic diagram illustrating absorption at van Hove singularities in metallic SWNTs.

Evident in the as-made SWNT film in Figure 4.2 are the characteristic absorption peaks attributed to electronic transitions between mirror image van Hove singularities above and below the intrinsic Fermi level, $E_{Fi}$ [49]. $E_{Fi}$ describes the energy level of the Fermi energy when no charge carriers have been extrinsically added. Interband energy transitions in semiconducting SWNTs are referenced as $S_{11}$ and $S_{22}$ respectively, while the intraband transition in metallic SWNTs is labeled as $M_{11}$. The absorption processes at these singularities are illustrated in Figure 4.3 for semiconducting and metallic SWNTs. In this figure, the electronic density of states is plotted versus energy, with zero energy denoting the intrinsic Fermi level position. As light interacts with SWNTs, peak photon absorption occurs in energy ranges where the electron density reaches a local maximum, i.e. van Hove singularities. The mean diameter of the SWNTs in this study is approximately 1.4 nm. As such, the Kataura plot [49] of the energy separation of van Hove singularities in SWNTs as a function of SWNT diameter can be used to predict

interband optical energy transitions. The expected $S_{11}$ and $S_{22}$ energy transitions for semiconducting SWNTs are 0.6 eV and 1.2 eV, respectively, and an intraband transition of 1.8 eV for the metallic $M_{11}$ transition. A reproduction of the Kataura plot is shown in Figure 4.4 [48].

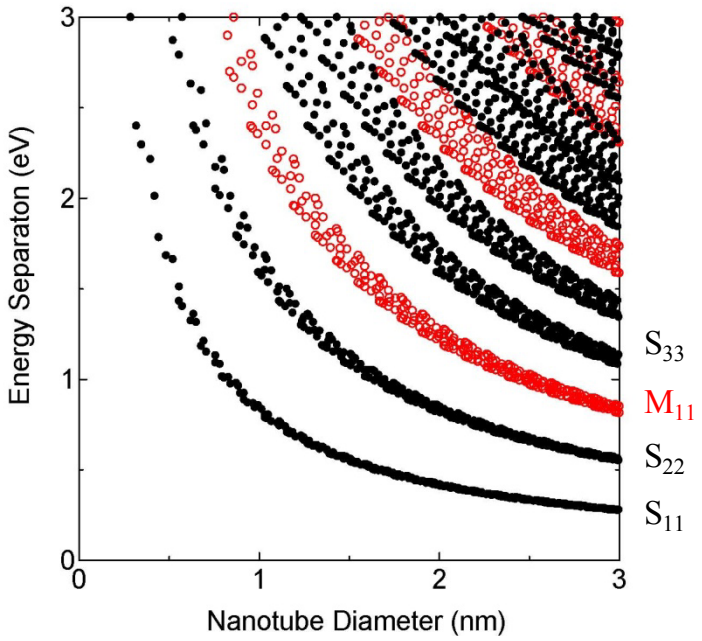


**Figure 4.4.** Reproduced Kataura plot of energy separation of van Hove singularities in carbon nanotubes versus nanotube diameter [48]. Black points are semiconducting nanotubes while red points are metallic nanotubes. The energy separation of van Hove singularities for the $S_{11}$, $S_{22}$, $M_{11}$, and $S_{33}$ energy transitions are denoted.

The observed absorption peaks in Figure 4.2 compare well with expected optical transition energies from the Kataura plot. An absorption peak can be seen for the $M_{11}$ transition at ca. 1.7 eV, while peaks observed for the $S_{11}$ and $S_{22}$ transitions are located at ca. 0.7 eV and 1.2 eV respectively. However, absorption attributed to the $S_{11}$ energy transition in Figure 4.2 is diminished with respect to the absorption expected from semiconducting SWNT density of electronic states. The bleaching of the $S_{11}$ energy peak

can likely be ascribed to the oxidation of SWNTs from oxygen adsorbed on the surface, as has been shown by other studies [72, 130]. As a result of oxidation, electrons in the valence band are withdrawn and therefore no longer contribute to interband energy absorption. The withdrawal of electrons can be conversely viewed as the injection of holes. Therefore, in the as-made film, a non-negligible amount of "unintentional" hole doping seems to occur. The SWNTs used in this study were not isolated from laboratory air during processing, nor was the exposure to oxygen history of the SWNTs as received from vendors known. Thus, it is highly likely that the SWNTs had significant exposure to oxygen and the resulting $S_{11}$ peak bleaching due to oxidation is within reason.

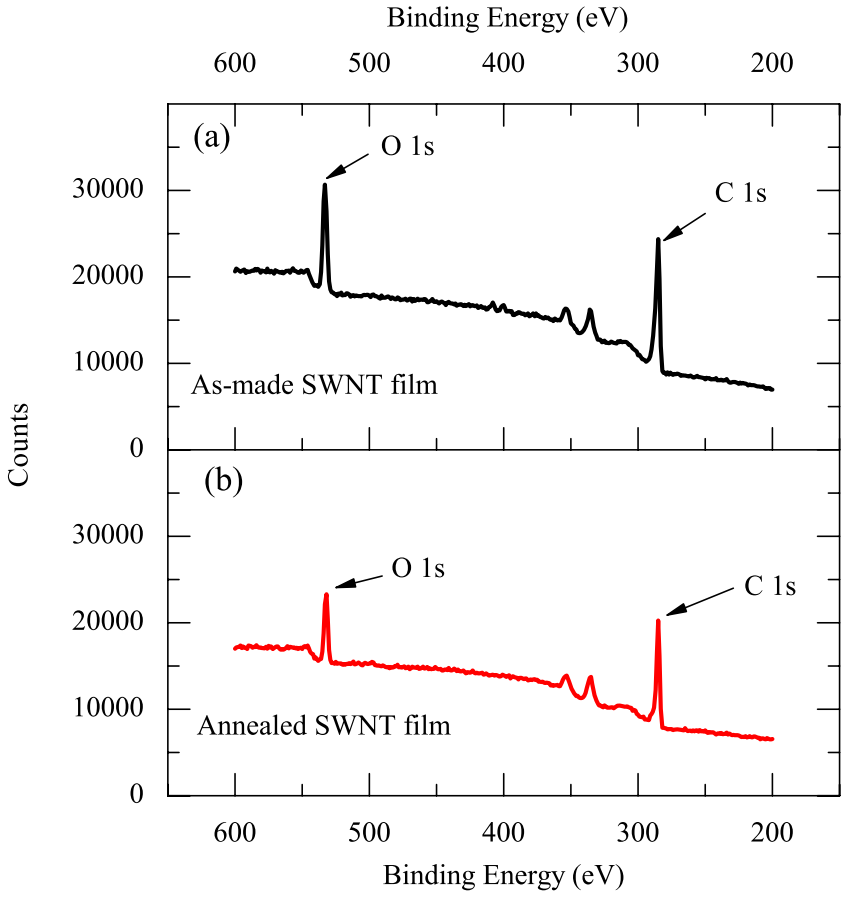


**Figure 4.5.** XPS spectra for (a) as-made SWNT film and (b) annealed SWNT film.

**Table 4.1.** XPS atomic ratio of oxygen to carbon species in SWNT films.

| | O:C | |
|---|---|---|
| | Range | Average |
| As-made film | [0.253, 0.255] | 0.254 |
| Annealed film | [0.175, 0.188] | 0.181 |
| Percent change | | -29% |

In order to validate the presence of oxygen on SWNT surfaces, X-ray Photoelectron Spectroscopy (XPS) was performed on the as-made film. XPS is a reliable measurement tool used to determine the chemical composition of materials and has been utilized to characterize SWNT films in prior reports [108]. The oxygen to carbon ratio as determined from the XPS spectra is shown in Table 4.1. Two locations were analyzed on each film and the average and range are included in the table. A representative XPS spectrum is shown in Figure 4.5a. Peaks associated with the binding energies of electrons from the 1s orbitals of oxygen and carbon atoms are denoted in the figure. A significant amount of oxygen species was found in the as-made SWNT network as indicated by the O1s peak in the spectrum and an average oxygen to carbon ratio of 0.254. A further validation of the presence of oxidation from air exposure was achieved by annealing the as-made SWNT films in vacuum at 200°C overnight (i.e. 14 hours) to remove adsorbed oxygen. Comparison of XPS measurements before and after annealing revealed a corresponding substantial decrease in the oxygen content of 29%. A reduced signature from the O1s electrons can be also be seen in Figure 4.5b. The remaining amount of oxygen species measured with XPS can likely be ascribed to carboxylic acid groups (OH–C=O) that are bonded to SWNTs during the purification process performed by SWNT manufacturers [72, 86]. After annealing, a substantial increase in the $S_{11}$ absorption peak can be seen in the transmittance spectra of an as-made and annealed film presented in Figure 4.6. Because the adsorbed oxygen species present on the SWNT surface prior to annealing have been removed, electrons are returned to their initial state

in the first van Hove singularity. Consequently, photon energies equal to the $S_{11}$ electronic interband transition will be absorbed as evidenced in the transmittance spectra at ca. 1850 nm.

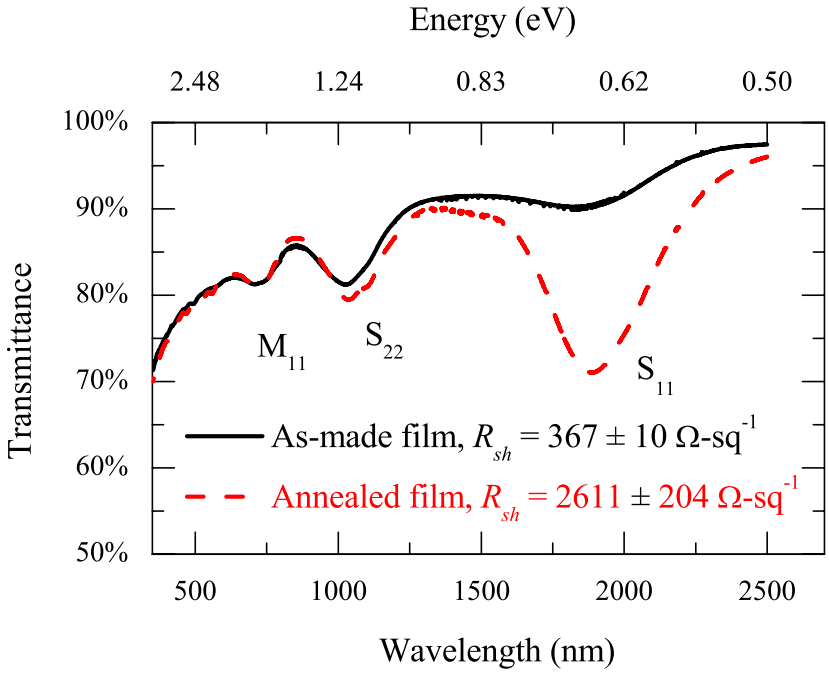


**Figure 4.6.** Optical transmittance spectra of an as-made and annealed SWNT film.

As a result of the "unintentional" oxygen doping of SWNT films, it is expected that the as-made film should demonstrate a lower $R_{sh}$ than the annealed film due to moderately doped semiconducting SWNTs that now exhibit metallic behavior. This is in fact the case in the two films. Prior to annealing, the as-made film had an $R_{sh}$ of 367 ± 10 Ω-sq$^{-1}$, compared to 2611 ± 204 Ω-sq$^{-1}$ after. This can be understood given the conducting sticks percolation model discussed in section 4.2 where previously non-conducting pathways now contribute to the parallel network conduction as a result of the unintentional degenerate doping of the semiconducting tubes. The $R_{sh}$ of the annealed film only represents the contribution of metallic SWNTs, a third of the network composition, that form percolating conduction pathways in the network. As the

semiconducting SWNTs are oxidized in the presence of adsorbed oxygen, p-type charge carriers are injected into the SWNTs, thereby resulting in more conducting pathways in the film. Given the parallel resistor construct presented earlier, more parallel pathways should significantly reduce the overall film resistance. The reduction in $R_{sh}$ of almost an order of magnitude in the experimental results supports this model.

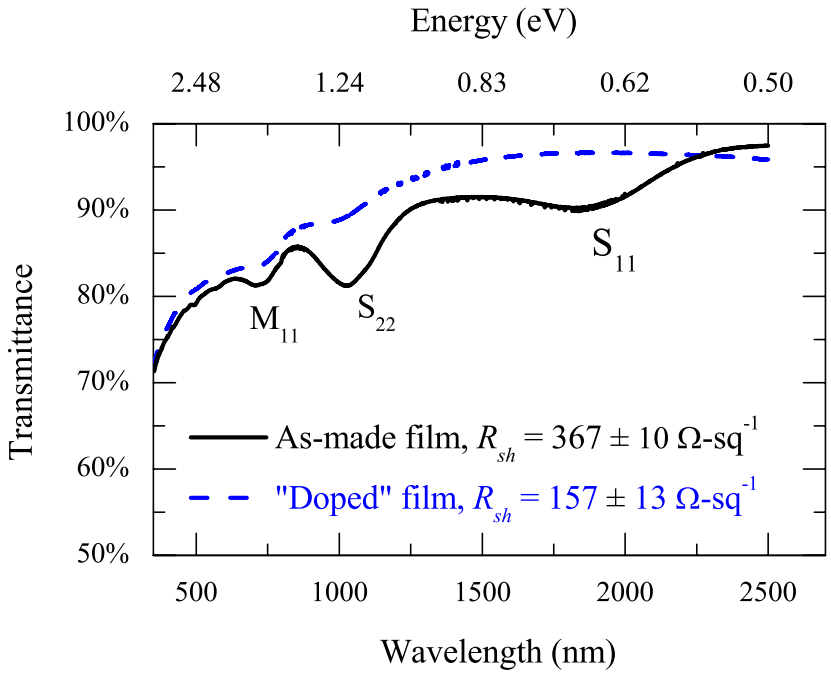


**Figure 4.7.** Optical transmittance spectra of an as-made and doped SWNT film.

The effect of further p-doping of SWNT films through chemical treatment in $HNO_3$ and $SOCl_2$ can be seen in the transmittance spectra shown in Figure 4.7. A total removal of the $S_{11}$ transition and a near complete reduction in the $S_{22}$ transition can be observed. This observation supports the position that chemical treatment with $HNO_3$ and $SOCl_2$ results in the injection of holes into the band structure of SWNTs. In addition, as more charge carriers are injected into metallic and semiconducting SWNTs through doping, $R_{sh}$ is reduced from 367 ± 10 Ω-sq$^{-1}$ to 157 ± 13 Ω-sq$^{-1}$. Because the parallel

pathways are governed by Eq. 4.1, each path is made more conductive with doping, as expected from Eq. 4.2.

Chemical treatment also results in the removal of any residual surfactant on SWNTs used to facilitate dispersion into aqueous solution, as discussed in Chapter 3. Residual surfactant increases $R_{SWNT\text{-}SWNT}$ as an additional electrical contact resistance between nanotubes. Shown in Figure 4.8 are the infrared spectra of as-made, annealed, and doped SWNT films. The wavenumber range is consistent with the vibrational stretch assigned to the C-H bond of dodecyl groups in the SDS surfactant [113]. The peaks are observed for the as-made and annealed films, but are absent from the chemically treated film. These results are in agreement with previous reports that have shown that treatment of SWNT films with nitric acid can remove residual surfactant [109]. As a result of chemical treatment, effectively all of the pathways are now "highly conductive pathways".

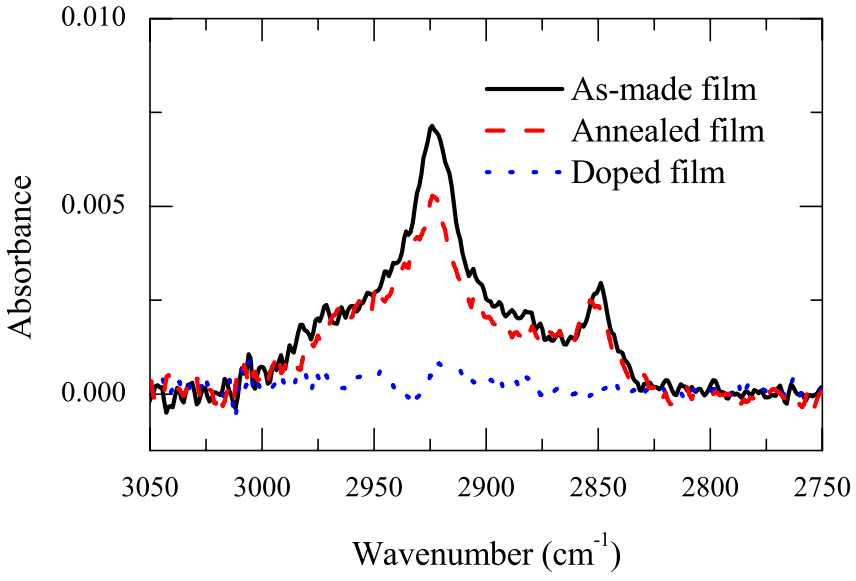


**Figure 4.8.** Infrared spectroscopy of an as-made, annealed, and doped SWNT film.

As evidenced in Figures 4.6 and 4.7, a significant correlation exists between $R_{sh}$ and the optical spectra of SWNT films in the near IR wavelength range. Specifically, the strength of the absorption peaks of the $S_{11}$ and $S_{22}$ energy transitions give direct insight into the amount of hole doping that has occurred in the film. However, when the optoelectronic properties of SWNT films are presented and discussed in the literature, typically, the sheet resistance and only the optical transmittance in the area near the visible spectrum (i.e. 350 – 1100 nm) are given. Often parametric studies or comparisons of multiple authors are made with regard to only the sheet resistance and transmittance at 550 nm. However, comparisons that do not consider the level of doping between different SWNT films are very likely to lead to spurious relationships and false conclusions. For example, if a particular SWNT sample has been exposed to more hole doping from exposure to air, its conductivity would be correspondingly affected. Therefore, any comparison that does not eliminate the possibility of hole doping contributions is purely speculative and may actually be false. Unfortunately, these types of speculative evaluations are pervasive in the literature at present. A qualitative assessment of the amount of hole doping can quickly and easily be inferred from the optical spectrum into the near infrared (e.g. [350 nm , 2500 nm]). An example is provided in Figure 4.9. With similar transparency in the wavelength range of 350 – 1100 nm (Figure 4.9a), film A has a sheet resistance of 304 $\Omega$-sq$^{-1}$ while film B has a sheet resistance of 809 $\Omega$-sq$^{-1}$, more than double that of film A. Both films were taken from the same solution and should therefore have similar properties in regard to SWNT diameter distribution, SWNT length, SWNT/surfactant concentration, and SWNT defect density, all critical parameters in determining overall SWNT film conductivity. If only

the optical spectra from 350 – 1100 nm is considered (Figure 4.9a), the origin of such a large discrepancy in electrical conductivity would be left to conjecture. However, observation of Figure 4.9b yields significant insight into the level of doping in each film. Film B has a considerably larger absorption intensity from the $S_{11}$ energy transition around 1800 nm, thus indicating a lower amount of p-type doping as discussed earlier in this chapter. With this insight gained from inspection of Figure 4.9b, the difference in electrical conductivity is no longer left to conjecture. Film A has a higher doping level than does the similarly processed film B. Therefore, it is expected from Eq. (4.2) that the electrical conductance of film A would be higher than film B.

As evidenced in the preceding example, when discussing the optoelectronic properties of SWNT films, it is imperative that conclusions be made with regard to the level of doping that has occurred in the film. Since an effective qualitative perspective can easily be gained through inspection of the optical absorption of the $S_{11}$ and $S_{22}$ energy transitions, optical transmittance spectra that is provided should extend to the near infrared as shown in Figure 4.9b. Such a full picture of the optoelectronic properties of specific SWNT films will facilitate a better understanding of the impact of other parametric inputs.

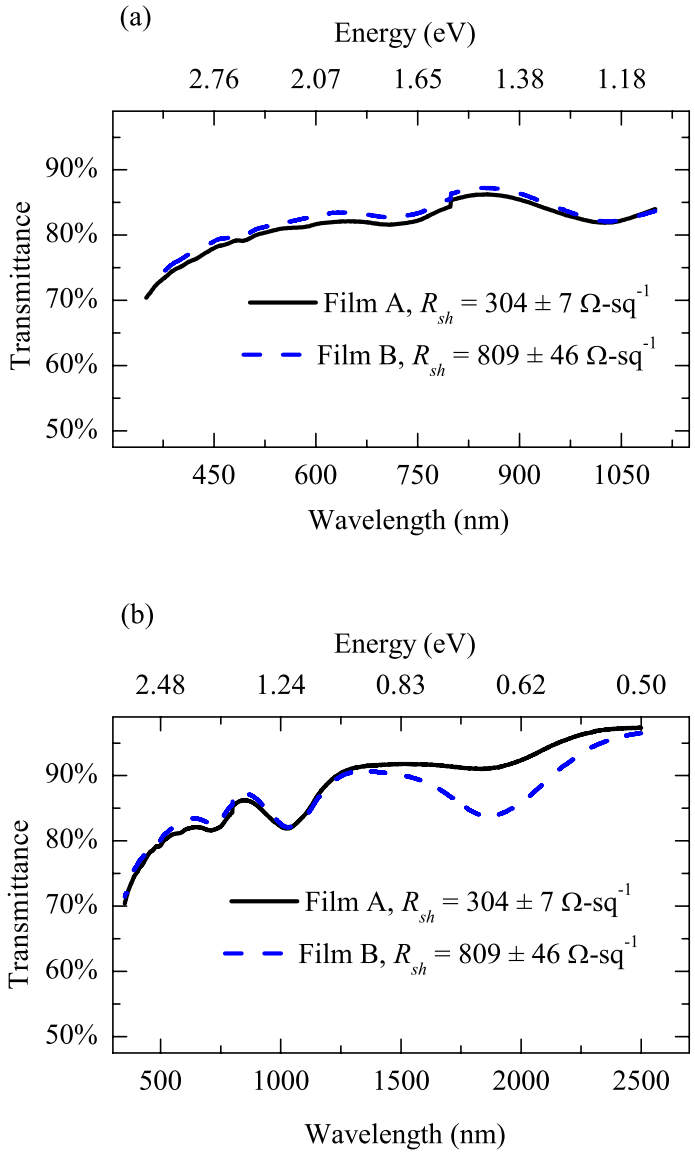


**Figure 4.9.** Optical transmittance of SWNT films with spectra wavelengths of (a) 350 – 1100 nm (b) 350 – 2500 nm.

### 4.3.2. Ultraviolet Photoelectron Spectroscopy (UPS) of SWNT Films

In addition to the evaluation of $R_{sh}$ and observation of the changes induced in the optical transmittance spectra to assess the impact of doping on SWNT films, the work function, $\Phi$, can also yield insight into the electrical nature of the film surface.

$\Phi$ is equal to the energy required to move an electron from the Fermi level, $E_F$, to vacuum. The effect of introducing charge carriers into individual SWNTs is to shift $E_F$ away from its intrinsic location, $E_{Fi}$. This effect can be qualitatively understood by re-examining the definition of $E_F$ as discussed in Chapter 2. $E_F$ is defined as the energy for which the probability of occupancy by an electron, $f$(E), is equal to ½ for all temperatures above absolute zero [131]. Therefore, as electrons are removed from the valence band through hole doping, the energy at which $f$(E) is equal to ½ is shifted to lower energies as illustrated in Figure 4.10 for an intrinsic and doped semiconducting SWNT. As $E_F$ is shifted to lower energies, the work function is also increased as shown in the figure.

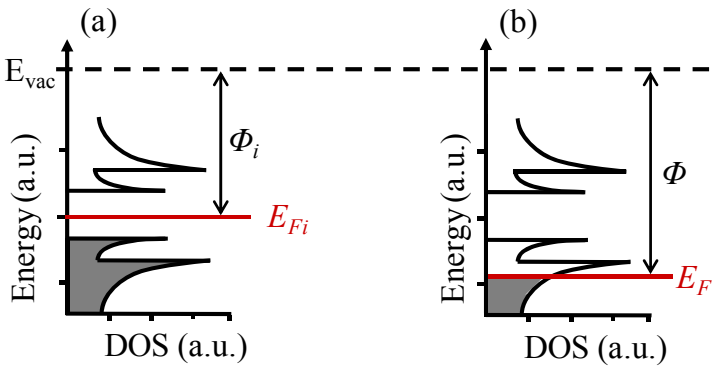


**Figure 4.10.** Density of electronic states versus energy for (a) intrinsic undoped semiconducting SWNT (b) degenerately doped semiconducting SWNT.

Ultraviolet Photoelectron Spectroscopy (UPS) can be used to determine $\Phi$ for a material through the measurement of kinetic energy of photoemitted electrons from its valence region [132]. UPS equipment and expertise were provided by the Dr. Neal Armstrong research group at the University of Arizona. The kinetic energy spectra of

an as-made SWNT film, an as-made SWNT film after annealing, and an as-made SWNT film after chemical doping are provided in Figure 4.11. For each film, three locations were analyzed on the surface of the film. The spectra most representative of the average are shown. The average low kinetic energy edge and corresponding work function are summarized in Table 4.2. The range of low kinetic energy edges measured at the three locations on the film is also included in the table. A photon energy, *hv,* of 21.2 eV was used to photoexcite valence electrons. In the analysis of UPS kinetic energy spectra, $\Phi$ is determined by:

$$\Phi = h\nu - (KE_{high} - KE_{low}) \qquad 4.3$$

where $KE_{high}$ and $KE_{low}$ are the high kinetic energy edge and the low kinetic energy edge, respectively. Because all samples were deposited on gold substrates for UPS testing, $KE_{high}$ was found for the gold substrate and was equal to 32.1 eV.

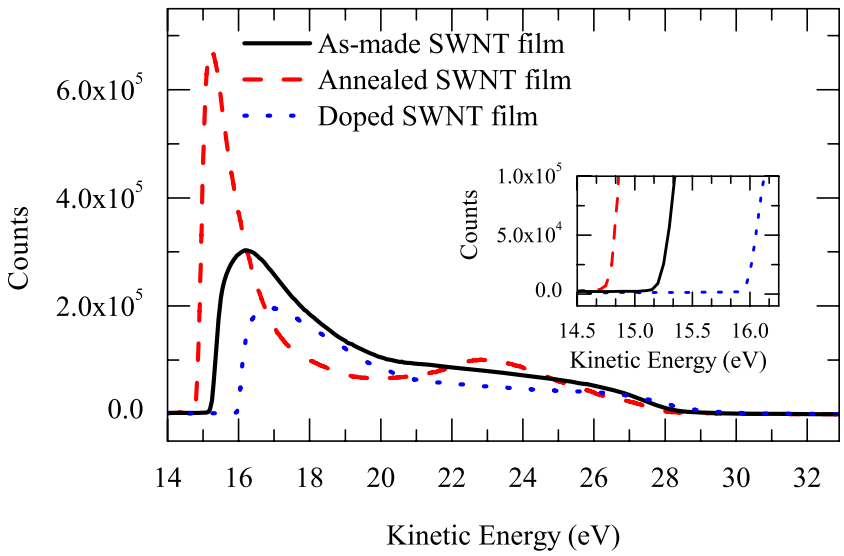


**Figure 4.11.** UPS kinetic energy spectra of as-made, annealed, and doped SWNT films. Inset: Low kinetic energy edge of provided spectra.

As expected, there is a significant difference between $\Phi$ of the samples, which is indicative of the $E_F$ change caused by "unintentional" oxidation and chemically induced hole doping. The lower $\Phi$ of the annealed SWNT film with respect to the as-made film provides further support of the conclusion that annealing an as-made film removes oxygen dopants, thus permitting the return of electrons to their intrinsic location in the density of states as described in Figure 4.10a. This evidence of "unintentional" doping is consistent with the aforementioned optical observations, XPS analysis, and electrical measurements of as-made and annealed SWNT films. The higher $\Phi$ of the doped SWNT film in comparison to the as-made SWNT film is also consistent with the conclusion made from the electrical and optical properties of SWNT films that chemical treatment results in additional hole doping. To this author's knowledge, the data presented in Table 4.2 represents the first summarized

report of the variation of $\Phi$ with "unintentional" and chemically doping. This is also the first known study to corroborate x-ray and ultraviolet photoelectron spectroscopy analysis, optical transmittance observations, and electrical measurements to clearly elucidate the effect of unintentional and chemically induced doping on SWNT films.

**Table 4.2.** Work function of as-made, annealed, and doped SWNT films.

| | $KE_{low}$ | | Average $\Phi$ |
|---|---|---|---|
| | Range (eV) | Average (eV) | (eV) |
| As-made | [15.13, 15.20] | 15.2 | 4.3 |
| Annealed | [14.73, 15.01] | 14.9 | 4.0 |
| Doped | [15.92, 15.93] | 15.9 | 5.0 |

### 4.3.3. Conductive-tip AFM Study of As-made and Chemically Treated SWNT Films

Conductive-tip AFM (C-AFM) instrumentation was used to map the conductivity of the SWNT surface and provide further insight into the impact of doping. C-AFM mapping of electrode surfaces is a useful method to determine the electrical activity of the surface on the nanoscopic scale. C-AFM equipment and expertise were provided by the Dr. Neal Armstrong research group at the University of Arizona. C-AFM current maps of an as-made and doped SWNT film are provided in Figure 4.12 and the effect of chemical treatment is immediately obvious. The images obtained for both samples were obtained with a tip to sample bias of 100 mV. The doped SWNT film in Figure 4.12b had significantly more surface area that passes current through the AFM tip. More current was indicative of a lower resistance between the AFM tip and the silver paste deposited on the SWNT surface a distance on the order of millimeters away. Chemical treatment not only resulted in electrical conductivity enhancement observable on the macroscopic scale (i.e. lower $R_{sh}$ as determined by the Transfer Length Method), the vast

majority of surface was electrically activated through reduction of electrical resistance along the nanotube and removal of surfactant on the surface of SWNTs that contributed to $R_{SWNT\text{-}SWNT}$.

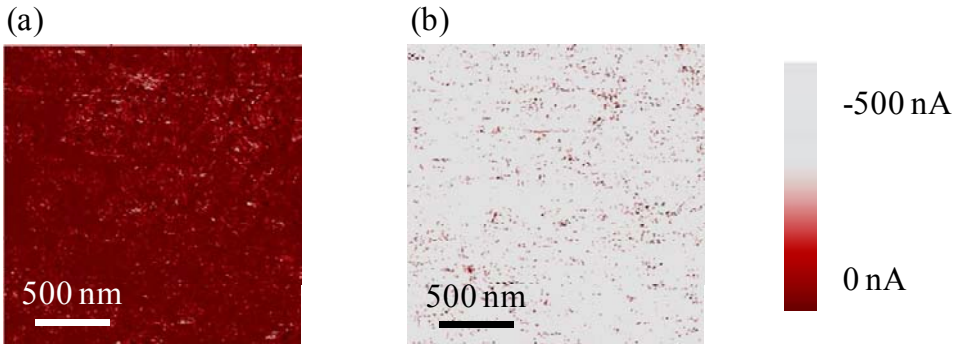


**Figure 4.12.** Conductive tip AFM images of (a) as-made SWNT film, (b) doped SWNT film.

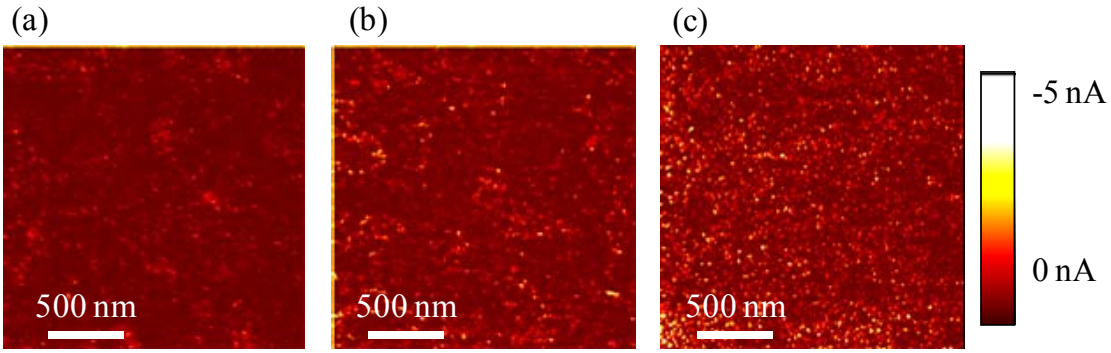


**Figure 4.13.** Conductive tip AFM images of (a) detergent cleaned ITO, (b) oxygen plasma cleaned ITO, (c) concentrated 12M HCl-0.2M $FeCl_3$ etched ITO. Images courtesy the Dr. Neal Armstrong research group at University of Arizona.

The importance of this result could be lost without examination of a C-AFM current map of ITO as shown in Figure 4.13. The images obtained for ITO were obtained with a tip to sample bias 5 mV in contrast to the higher bias used in the imaging of SWNTs. However, the behavior of the ITO was found to be similar at higher biases. In this regard, it is important to observe the "active" versus electrically "inactive" regions.

Detergent cleaned ITO had only a small percentage of surface area that was electrically "active". Even after improvement with concentrated acid treatment with 12M HCl-0.2M $FeCl_3$ solution, the surface still retained significant electrically inactive regions in comparison to the doped SWNT film. The importance of this difference between the doped SWNT film and the best case ITO can be understood within the application context of transparent electrodes. For example, in an organic photovoltaic device, charges are incident on the entire surface area of the electrode for collection. If the entire electrode is not nanoscopically conductive, charges will be forced to "redirect" to an electrically active area. Redirection of charges may increase recombination probability within the donor layer and thereby contribute to lower overall power conversion efficiency. In contrast, the vast majority of the surface of the doped SWNT film is conducive to charge collection. Therefore, while the present status of SWNT films may not have comparable macroscopic $R_{sh}$ with ITO, the better nanoscopic properties of doped SWNT electrodes may be able to compensate for such deficiencies. Furthermore, as progress continues in the reduction of $R_{sh}$ in transparent SWNT electrodes, the homogeneous nature of the electroactive surface of SWNTs may facilitate a better than expected improvement in device performance over ITO based devices.

### 4.4. Stability of Doped SWNT Films upon Air Exposure

It is clear that hole doping of SWNT films has a positive impact on the optoelectronic properties with regard to transparent electrode applications. In addition to the unintentional doping provided by oxidative oxygen species on the surface of SWNTs, chemical treatment further reduces $R_{sh}$ and electrically activates the entire surface. However, the stability of the doping enhancements from chemical treatment is of question, since it is known that acyl chlorides groups are very reactive and as such are often used as an reaction intermediate in the functionalization of SWNTs [133]. Similarly, the doping effects of $HNO_3$ have been shown to be easily reversible [113]. Futhermore, in actual device fabrication, chemical treatment of the anode would be an initial step followed by subsequent steps that include active layer deposition, cathode deposition, and module encapsulation. Each of these steps may involve processing at moderate temperatures such as plasma enhanced CVD (PECVD) for device encapsulation. In addition, actual device operation may also subject the SWNT films to moderately elevated temperatures [134]. Hence, it is desirable to have doped SWNT electrodes with enhanced electrical properties that are stable when exposed to air and to moderate temperatures. However, the electrical stability of such films with time and under thermal loading has not been evaluated in the literature.

In this section, the electrical stability of highly conductive transparent doped SWNT electrodes is investigated and presented. The degradation of the electrical conductivity of films doped with (i) $SOCl_2$, (ii) $HNO_3$, or (iii) $HNO_3$ followed by $SOCl_2$ was monitored with exposure to air and as a function of temperature from 20 to

80 ºC. The moderate temperature range investigated was chosen because it is typical of temperatures SWNT films would be exposed to during subsequent processing and device operation.

Figure 4.14 shows the evolution of the electrical properties of as-made and doped SWNT films upon exposure to laboratory air at ambient room temperature. While the sheet resistance of the as-made film remained stable with an initial $R_{sh}$ of 249 ± 2 Ω-sq$^{-1}$, all doped SWNT films showed a significant increase of the sheet resistance as a function of time. The cause of the increased $R_{sh}$ can be ascribed to the loss of hole dopants to the environment. The film doped with $SOCl_2$ had an initial sheet resistance of 202 ± 1 Ω-sq$^{-1}$ and experienced an increase of 18% over 400 hours to 234 ± 1 Ω-sq$^{-1}$. Films treated with $HNO_3$ and the combination of $HNO_3$ and $SOCl_2$ had lower initial sheet resistances (145 ± 3 Ω-sq$^{-1}$ and 141 ± 6 Ω-sq$^{-1}$, respectively). However, upon air exposure, these films experienced an increase of 50% or more over the same 400 hour period to final values of 202 ± 1 Ω-sq$^{-1}$ and 211 ± 13 Ω-sq$^{-1}$ for $HNO_3$ and $HNO_3$ plus $SOCl_2$ doping respectively. While the percentage increase in the sheet resistance was larger than that of $SOCl_2$ treated films, the sheet resistance was still lower after the 400 hour period. The increase in $R_{sh}$ of the film treated with $HNO_3$ provides further support of the hypothesis that the oxidative behavior of $HNO_3$ results in p-doping of SWNTs. This is in contrast to the report by Geng et al. [109] that stated $HNO_3$ did not result in p-type doping of SWNTs in the film. Of note, the low $R_{sh}$ of the as-made film in comparison to the mean $R_{sh}$ presented in section 3.4.3 is due to its lower transmittance at 550 nm of 75% in contrast to the 80% transmittance of the films discussed therein. The three chemically treated films

investigated for air exposure stability had a transmittance of 80% at 550 nm.

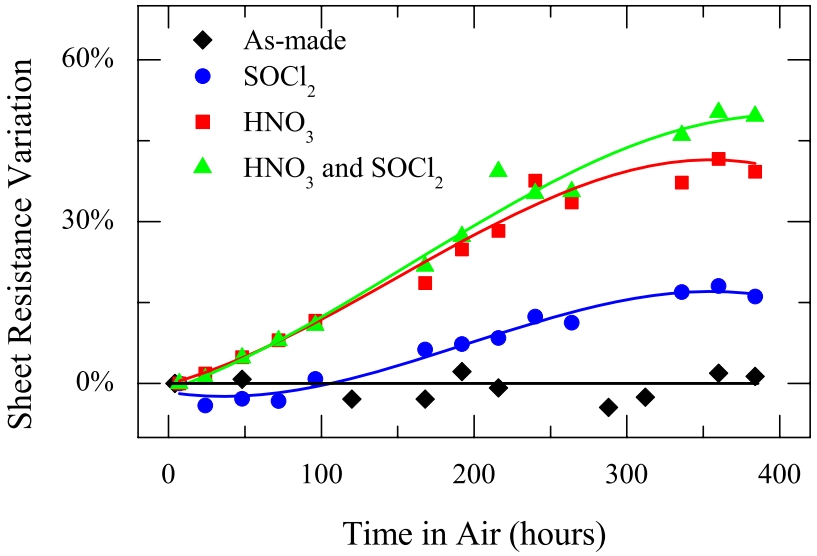


**Figure 4.14.** Sheet resistance variation versus time in air of four SWNT films. Lines are shown as a guide to the eye.

In addition to measuring $R_{sh}$ as a function of time in air to establish the stability of chemically induced hole doping of SWNTs, changes in $\Phi$ can also yield salient insight regarding the electrical nature of the surface of the film. It is expected that as the conductivity improvement induced by hole doping via chemical treatment is mitigated due to loss of hole dopants, $E_F$ should return to higher energies toward its intrinsic level. Because $\Phi$ directly measures the position of $E_F$, as shown in Figure 4.10, observation of the work function of the SWNT films evaluated in Figure 4.14 should provide further evidence of this effect.

To measure the stability of $\Phi$, relative work functions, $\Phi_{ref}$, were measured with a Qcept Technologies wafer inspection system (Chemtriq 500L). This system consists of a scanning Kelvin probe and has a capability of full wafer imaging and

local work function measurement through the utilization of a nonvibrating contact potential difference (CPD) technique.[135] For stability testing, one SWNT film was prepared for each type of doping treatment (i.e. $HNO_3$, $SOCl_2$, and $HNO_3$ plus $SOCl_2$) and divided into three samples (Figure 4.15). One sample was transferred to glass and subsequently chemically treated. $R_{sh}$ was measured versus exposure time to environment and the results of which were discussed in the previous section and shown in Figure 4.14. Concurrently, the remaining two samples were transferred to silicon substrates for work function measurements. One sample was exposed to chemical treatment, while the other served as a reference as-made sample.

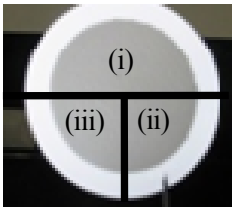


**Figure 4.15.** Illustration of SWNT film sample preparation. SWNT film on the MCE membrane was divided into three samples (i), (ii), and (iii). Sample (i) was transferred to glass and subsequently chemically treated. $R_{sh}$ was measured as a function of exposure time to ambient air (Figure 4.14). Sample (ii) was transferred to a silicon substrate and subsequently chemically treated. Sample (iii) served as the reference as-made sample and was transferred to a silicon substrate and not chemically treated. $\Phi$ was measured as a function of exposure time to ambient air.

In Figure 4.16, the change in $\Phi_{ref}$ for chemically treated films is shown. $\Phi_{ref}$ is equal to the work function of the chemically treated sample relative to the reference as-made sample. Initial Kelvin probe measurements were conducted two hours after doping the films, unlike the immediate UPS measurements made in section 4.3.2. Therefore, it is likely that the work function increase, anticipated in light of previous UPS measurements, was effectively mitigated on the surface of the films after exposure to moisture in air at typical conditions of 30 – 40% relative humidity. After eight hours, the work function of the $SOCl_2$ treated film stabilized at a value approximately 100 meV less than as-made film. While a work function magnitude of the chemically treated film smaller than the reference film was unexpected, it could be attributed to chemically induced defects on the SWNTs which increased the density of states at the Fermi energy. The increased density of states at the surface could in turn reduce the work function [136]. It is also possible that some of the "unintentional" oxygen doping on the as-made film was removed during chemical processing. Therefore, as the chemically induced dopants were removed, the chemically treated film surface returned to a state of fewer "unintentional" oxygen dopants on the surface in comparison to the as-made film. As a result, $\Phi$ of the air-exposed, chemically doped film was not as large as $\Phi$ of the oxidated as-made film.

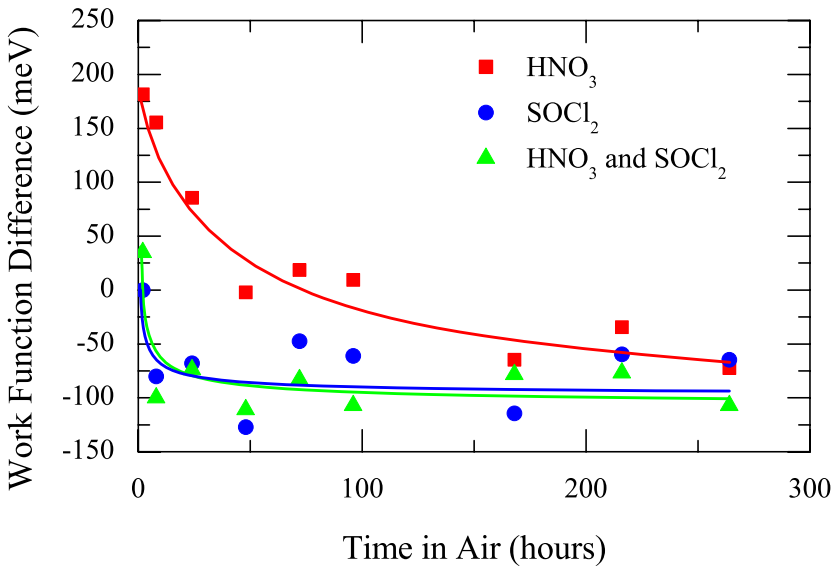


**Figure 4.16.** Work function difference between chemically treated and as-made SWNT samples as a function of air exposure for various doping process. Lines are shown as a guide to the eye.

After approximately seven days (168 hours) the work function of the $HNO_3$ treated film was comparable to the work function of $SOCl_2$ treated films. In all cases, the rate at which the work function of the chemically treated films decreased to a level below the as-made films was much higher than the rate of degradation in $R_{sh}$, as seen in Figure 4.14. Since the Kelvin probe work function measurement only considers the electronic nature on the surface of the film, it is therefore possible that only the functional groups on or very near the surface of the chemically treated films reacted quickly with air, while electron withdrawing molecules continued to interact with SWNTs in the bulk below the surface. This would be consistent with the higher conductivity over time of the chemically treated films compared with as-made ones.

It is interesting to point out that the work function of the film chemically

treated with the combination of $HNO_3$ and $SOCl_2$ behaved in a similar manner to that of $SOCl_2$ treated film. Thus, it appears that the surface of this film was comparable to $SOCl_2$ treated film while the bulk remains dominated by the initial $HNO_3$ treatment as suggested by its electrical stability after air exposure which was similar to that of $HNO_3$ treated films (Figure 4.14). These observations could be ascribed to a normal intercalation of $HNO_3$ molecules and/or $NO_x$ ions within the SWNT film during the initial $HNO_3$ treatment. However, immersion into $SOCl_2$ caused desorption of ionic species remaining on the surface, while introducing reactive acyl chloride groups. Since the measured work function was that of only the surface of the film, as was seen in the case of the film only treated with $SOCl_2$, it is likely that a rapid decomposition of acyl chlorides on the surface due to exposure to moisture in air occurred.

### 4.5. Impact of PEDOT:PSS Capping Layer on Doping Stability

In recent work [103, 137, 138], OLEDs and OPVs with SWNT films as the transparent electrode utilized PEDOT:PSS as a planarization layer on SWNT films to reduce surface roughness. The additional PEDOT:PSS layer was found to have no adverse effects on the conductivity of the resulting films [103]. This conducting polymer is also utilized on transparent conducting oxides in organic electronics to facilitate hole collection and injection. However, the PEDOT:PSS layer may also play an additional critical role in acting as a capping layer to stabilize the sheet resistance of the SWNT films. In this role, the PEDOT:PSS layer would act to prevent the reaction of acyl chloride groups of the nanotubes with air and prevent the

desorbtion of $HNO_3$ from the films.

The effect of PEDOT:PSS on the electrical stability with time after doping SWNT films is presented in Figure 4.17. A thin layer of PEDOT:PSS (Baytron P AI 4083) was spin coated at 5000 rpm for one minute on top of sample films followed by baking at 140°C for 10 minutes in air. Utilizing a stylus profilometer, the measured thickness of the PEDOT:PSS layer was approximately 30 – 40 nm. Given the low conductivity of PEDOT:PSS, approximately 0.001 S $cm^{-1}$, the sheet resistance of the layer alone would be approximately 250 – 330 MΩ-$sq^{-1}$. In comparison with the low sheet resistance of SWNT films presented in chapters 3 and 4, the sheet resistance values and corresponding variations obtained during testing can be assigned to the SWNT films beneath. In each case, the air stability of a coated and uncoated SWNT film is compared. For the films treated with $SOCl_2$, the uncoated film showed a sheet resistance increase of 15% after 240 hours while the PEDOT:PSS coated film showed an increase of less than 5%. For the $HNO_3$ treated film without the PEDOT:PSS layer, a 30% increase in sheet resistance occurred after 240 hours. Similarly, the use of the organic capping layer again resulted in an increase of only 5% after 240 hours. Finally, films which used a combined doping of $HNO_3$ and $SOCl_2$ without the PEDOT:PSS layer showed an increase of 30% after 240 hours and virtually no change in sheet resistance occurred with the addition of the PEDOT:PSS capping layer after 10 days. Additionally, extended testing carried out in air and at room temperature, show that the sheet resistance of the same sample capped with PEDOT:PSS was stable up to 1,500 hours while the samples which were not capped showed an increase in sheet resistance of 120%. It is clear that the addition of a organic capping layer

dramatically increases the stability in electrical properties of chemically treated films over time.

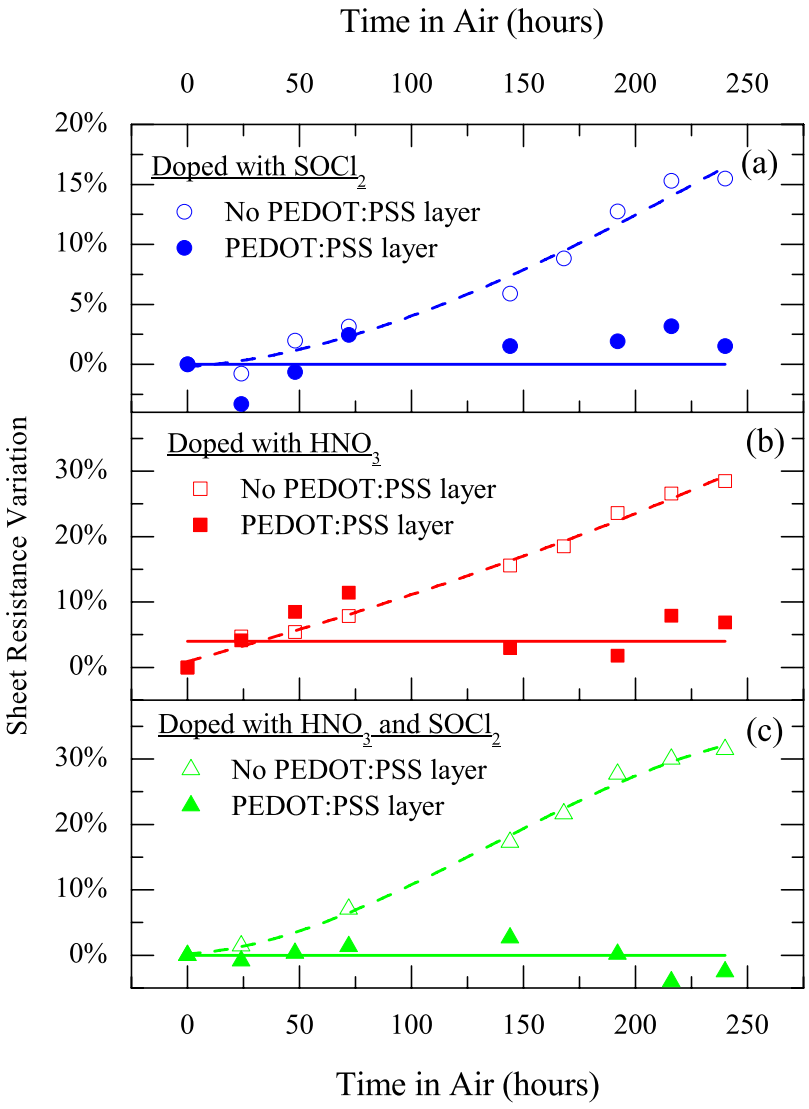


**Figure 4.17.** Sheet resistance increase of SWNT films versus time in air for: (a) $SOCl_2$ treated films with and without a PEDOT:PSS layer. (b) $HNO_3$ treated films with and without a PEDOT:PSS layer. (c) $HNO_3$ and $SOCl_2$ treated films with and without a PEDOT:PSS layer. Lines are shown as a guide to the eye.

Because exposure to elevated temperatures may be experienced during the operation of OLEDs and OPVs or during device fabrication steps, the thermal stability of chemically treated SWNT films are also addressed in this chapter. Elevated temperatures may enhance the loss of dopants out of the films. The results of the thermal stability experiments are shown in Figure 4.18. Changes in the sheet resistance for temperatures ranging from 20-80°C were measured for as-made and chemically treated SWNT films. In these experiments, the samples were heated to the setpoint temperature and the sheet resistance was measured at the setpoint. For each figure, data for films coated with a capping layer of PEDOT:PSS are presented with uncoated films. No significant differences in the temperature dependence of the sheet resistance were observed with the addition of a PEDOT:PSS capping layer. As shown in Figure 4.18a, the sheet resistance of as-made SWNT films and as-made SWNT films coated with PEDOT:PSS did decrease slightly with increasing temperature which is consistent with claims of previous reports. Some reports have shown that one dimensional metallic nanotubes have such a temperature dependence of their conductivity as described by a Luttinger Liquid which is different from bulk metallic systems [139-141]. In this manner, the electrical conductance, $G$, follows a power-law behavior as a function of temperature $T$, $G \propto T^{\alpha}$, where $\alpha$ provides insight into the strength of the innertube electron interaction. Others have attributed the decrease in $R_{sh}$ with increasing temperature to fluctuation-induced tunneling through barriers between contacting nanotubes.[30, 128, 142] It is likely that both the effects of 1-D Luttinger Liquid characteristic of SWNTs and fluctuation-induced tunneling contribute to the observed behavior in Figure 4.18a.

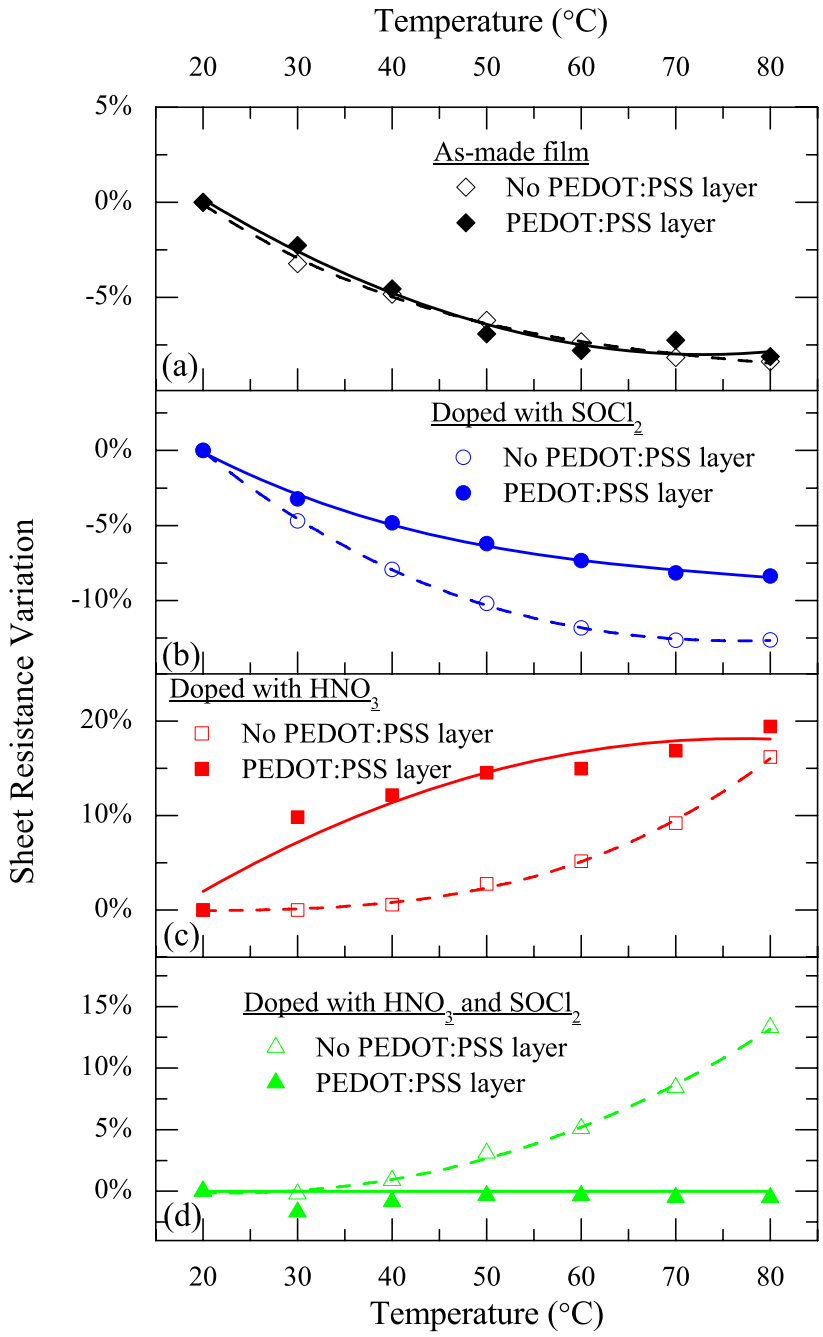


**Figure 4.18.** Sheet resistance increase of SWNT films versus temperature for: (a) as-made films with and without a PEDOT:PSS layer. (b) $SOCl_2$ treated films with and without a PEDOT:PSS layer. (c) $HNO_3$ treated films with and without a PEDOT:PSS layer. (d) $HNO_3$ and $SOCl_2$ treated films with and without a PEDOT:PSS layer. Lines are shown as a guide to the eye.

The electrical resistance of SWNT films treated with $SOCl_2$ also decreased by up to 10% with increasing temperatures between 20 – 80°C as shown in Figure 4.18b. The cause of the decrease is similar to that described for the as-made film. In contrast, the films treated with $HNO_3$ both demonstrated an increase in resistance with increasing temperature. Whereas earlier reports have shown intercalated $HNO_3$ and $NO_x$ ions readily desorb under thermal annealing at temperatures greater than 350°C [113, 143], we see this effect at temperatures less than 80°C. The $HNO_3$ treated film with a layer of PEDOT:PSS has an initial sharp increase in resistance with increasing temperature in comparison to the $HNO_3$ film with no layer of PEDOT:PSS. This could be explained by the interaction of the $HNO_3$ molecules on the surface of the SWNT film with the PEDOT:PSS layer. As was seen in the Kelvin probe study, the $HNO_3$ treated film retained significant surface interactions that were observed through measurements of higher values of the work function.

The case of films treated with a combination of $HNO_3$ plus $SOCl_2$ is shown in Figure 4.18d. The data show essentially no change in sheet resistance upon heating up to 80ºC when the film is capped with a layer of PEDOT:PSS. This is in contrast to uncapped chemically treated films whose resistance increases by more than 13% at elevated temperatures. Similar to the investigation of $R_{sh}$ versus exposure time in air, the film chemically treated with $HNO_3$ plus $SOCl_2$ behaved in a manner consistent with the film chemically treated only with $HNO_3$ and unlike the film treated with only $SOCl_2$.

Upon returning to room temperature, all uncapped chemically treated films exhibited a residual permanent increase in sheet resistance of 7%, 4%, and 6% for the $HNO_3$ treated, $SOCl_2$ treated and $HNO_3$ plus $SOCl_2$ treated films, respectively. However,

the $HNO_3$ plus $SOCl_2$ treated film capped with PEDOT:PSS showed no appreciable permanent change in resistance upon returning to room temperature with resistance values being within 1% of the original value. Thus, the capping layer shows the ability to stabilize both the temperature dependence of the sheet resistance and the stability after exposure to elevated temperatures.

## 4.6. Conclusion

The goal of this chapter was to communicate a lucid understanding of conduction in SWNT films and the methods by which improvements are achieved. To this end, a qualitative understanding of electrical conduction in SWNT film was first presented to serve as a basis for further discussion. Next, multiple modes of experimental characterization were corroborated with theoretical SWNT electronic structure to describe the impact of moderate and heavy charge carrier doping on the optical and electronic properties of SWNT films. A moderate level of p-type doping was shown to occur in as-made SWNT films due to air exposure, as evidenced by comparison to annealed samples. Chemical treatment was shown to result in a heavy level of p-type doping, as well as the removal of residual surfactant on SWNTs. Photoelectron spectroscopy was used to determine and present the first summarized report of the variation of the work function of as-made, annealed, and chemically doped SWNT films. Furthermore, conducting-tip AFM was utilized to reveal the highly electro-active nature of the SWNT film surface after chemical treatment, particularly with respect to the surface of ITO.

Of importance was the observation that as-made SWNT films contain a non-negligible amount of doping, as can be inferred from optical transmittance in the near infrared (ca. 1100 – 1800 nm). As such, investigations of the optoelectronic properties of SWNTs that do not control for unintentional hole doping contributions cannot be considered purely conclusive and may actually be false. It is imperative that conclusions be made with regard to the level of doping that has occurred in the film. Since an effective qualitative perspective can be gained through inspection of the optical absorption of the $S_{11}$ and $S_{22}$ energy transitions, optical transmittance spectra that are provided should extend to the near infrared (e.g. 2500 nm). Such a full picture of the optoelectronic properties of specific SWNT films will facilitate a better understanding of the impact of other parametric inputs and aid the overall development of SWNT networks as a transparent electrode.

While doping via chemical treatment was shown to yield enhanced film conductivity through p-type doping, these films exhibited limited stability in air over time and limited thermal stability at moderate temperatures. However, a thin layer of PEDOT:PSS was shown to effectively limit the degradation of films and even stabilize the improved sheet resistance of chemically treated films. These results help to address critical questions concerning the stability of chemically treated SWNT electrodes intended as a surrogate for ITO electrodes in organic electronic devices.

# CHAPTER 5: EVALUATION OF CARBON NANOTUBE NETWORKS OF HOMOGENEOUS ELECTRONIC TYPE

## 5.1. Introduction

As has been demonstrated in this dissertation, thin films of SWNT networks exhibit optical, electrical, and mechanical properties that show promise to become a viable alternative to transparent conducting oxides (TCO) as an electrode in electronic devices. The SWNT networks presented in chapters 2 – 4 consisted of a heterogeneous mixture of nanotubes with metallic and semiconducting behavior. The ratio of metallic to semiconducting SWNTs in these types of polydisperse networks is typically 1:2. In order to fully realize the potential of SWNT networks as a transparent electrode in organic electronic devices, it may be necessary to utilize monodisperse networks that leverage the electronic homogeneity of the film to achieve optimal device performance. Progress in the efficient separation of SWNTs by electronic type now allows for such an approach to be taken [144, 145].

While SWNTs can be classified as either metallic or semiconducting in behavior based on the chirality of the tube [146], because SWNTs are 1-D in structure, the traditional metal/semiconductor classifications are no longer strictly valid. In particular, metallic SWNTs have a relatively small density of states (DOS) at the Fermi energy when compared to traditional bulk metals [147]. On the other hand, semiconducting SWNTs can have a larger density of electronic states within the valence band, in comparison to metallic SWNTs at a similar energy level, as illustrated in Figure 5.1. A full understanding of the optoelectronic impact on nanotube electrodes that such a

departure from a traditional classification of metals and semiconductors has yet to be achieved.

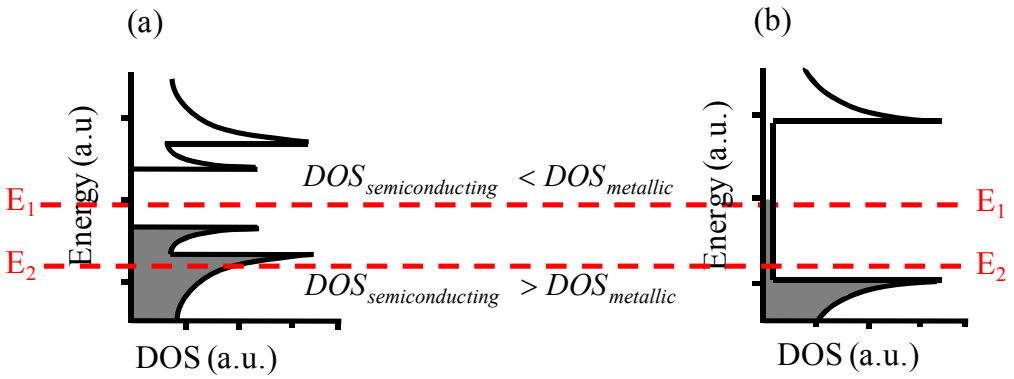


**Figure 5.1.** Illustration of the electronic density of states in (a) semiconducting SWNTs and (b) metallic SWNTs.

In a manner similar to that shown in chapter 4, heterogeneous films of metallic and semiconducting SWNTs can be effectively p-doped via chemical treatment with $HNO_3$ and $SOCl_2$ for improved conductivity [24, 97]. However, the impact of doping differs largely between metallic and semiconducting SWNT films as can be deduced from Figure 5.1 and as recently reported by Blackburn et al. [128]. In their study, films of monodisperse doped metallic SWNTs were higher in electrical resistance than similarly processed homogeneous networks of degenerately doped semiconducting SWNTs. This result is contrary to a conventional understanding of metals and semiconductors and in contrast to the goal of some research groups to obtain all metallic SWNTs for optimal transparent electrode optoelectronic properties [120]. Therefore, the goal of this chapter is to resolve this point of contest by applying the intrinsic electronic properties of the individual SWNTs that comprise the nanotube network to develop a

clear description of the optoelectronic behavior of SWNT films of metallic or semiconducting electronic type. Corroborative optical transmittance spectra, SWNT electronic band structure theory and photoelectronic characterization will be provided to support the conclusions presented.

## 5.2. Optoelectronic Characterization of Homogeneous Metallic and Semiconductor SWNT Films

SWNT solutions with greater than 95% homogeneity by electronic type and diameter range of 1.2 ~ 1.6 nm were purchased from Nanointegris and used to prepare transparent SWNT films on glass substrates as described in chapter 3. The SWNT film electrical sheet resistance, $R_{sh}$, was determined via the Transfer Length Method (TLM) described in chpater 3. Chemical treatment of the SWNT films was performed by immersing the films into solution for 45 minutes. The films were first immersed into $HNO_3$, removed and carefully air blown dry, subsequently heated on a hot plate at 90°C for a short time (e.g. 2 minutes) to remove any residual solution on the substrate, and then immersed into $SOCl_2$. After removing the film from the $SOCl_2$ bath, the film was blown dry with air and heated on the hot plate. The final heating step was proven effective to eliminate optical transmission losses in the visible range by preventing the soft haze that forms on the substrate from $SOCl_2$ exposure. SWNT films exposed to chemical treatment are referenced as "doped" in this report. SWNT films not exposed to chemical treatment are referenced as "as-made". Optical spectra for each SWNT film were measured using a Cary 5E UV-Vis-NIR dual-beam spectrophotometer. As expected, $R_{sh}$ of the as-made metallic SWNT film is less than

the $R_{sh}$ of the as-made semiconductor film, with values of 135 ± 4 Ω-sq$^{-1}$ and 465 ± 6 Ω-sq$^{-1}$ respectively.

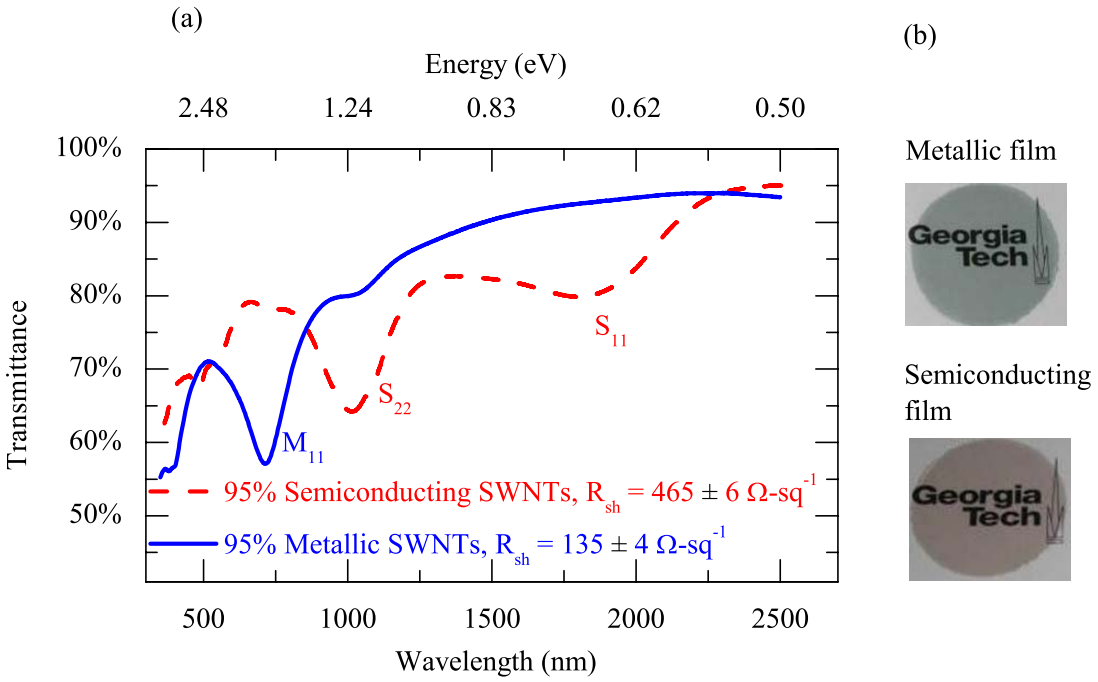


**Figure 5.2.** (a) Optical transmittance versus wavelength for as-made metallic and semiconducting SWNT films. Energy transitions at $S_{11}$, $S_{22}$, and $M_{11}$ van Hove singularities are labeled. (b) Photograph of metallic and semiconducting SWNT films on glass substrates. Georgia Tech logo is behind the film to illustrate transmittance.

Shown in Figure 5.2 are the optical transmittance spectra for as-made metallic and semiconducting SWNT films. Absorption peaks characteristic of metallic or semiconducting electronic type SWNTs can be clearly seen in the respective film. The origin of these absorption peaks was discussed in Chapter 4 but will be summarized again. Unlike the general illustration shown in Figure 5.1, the electronic density of states versus energy from the intrinsic Fermi level, $E_{Fi}$, are specifically calculated for SWNTs with (n,m) chiralities of (11,10) and (10,10) [48] and plotted in Figure 5.3. These

selected SWNTs have a diameter of approximately 1.4 nm and are representative of the diameter range of semiconducting and metallic SWNTs present in the SWNT networks used in this study. The (11,10) SWNT exhibits semiconducting behavior while the (10,10) SWNT is metallic. As discussed in chapter 2 (Eq. (2.10)) the electronic properties of SWNTs are proportional to the inverse of SWNT diameter and SWNTs of the similar diameter and electronic type exhibit similar electronic properties. Therefore, selection of these SWNTs provides an adequate depiction of the electronic structure of the SWNTs that comprise the film studied in this chapter. Only the band structure below $E_{Fi}$ is shown in the figure for clarity. The optical absorption peaks observable in Figure 5.2a are present due to electronic transitions between mirror image van Hove singularities above and below $E_{Fi}$ [49]. Interband energy transitions in semiconducting SWNTs are referenced as $S_{11}$ and $S_{22}$ for the first and second van Hove singularities respectively, and are labeled as such in the figure, while the intraband transition in metallic SWNTs is labeled as $M_{11}$. Also, shown in Figure 5.2a are the approximate spectral ranges for colors in the visible spectrum. As observed in the figure, the semiconducting SWNT film is more transmissive in the red color range, while the metallic film transmits more blue-green colors in the visible. This effect is also clearly seen in the photographs of a semiconducting and metallic SWNT film on a white background in Figure 5.2.b. Since the white background reflects light back through the film, the semiconducting SWNTs are visible as a red film, while the metallic SWNTs are visible as a blue-green film. The Georgia Tech logo is behind the film on the white background to illustrate transmittance.

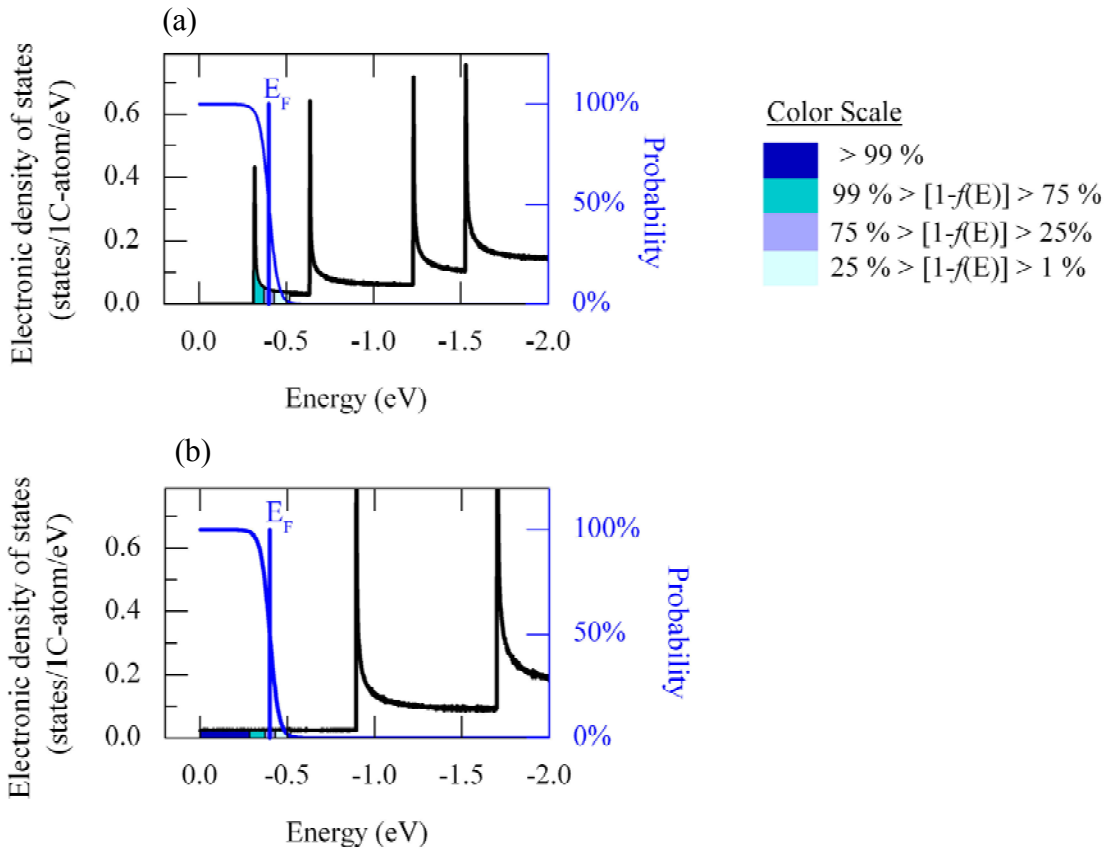


**Figure 5.3.** (a) (11,10) Semiconducting SWNT 1-D density of states with moderate doping. (b) (10,10) Metallic SWNT 1-D density of states with moderate doping. $E_{Fi}$ is set to zero.

Of particular note is the diminished absorption attributed to the $S_{11}$ energy transition in contrast to the absorption expected from observation of semiconducting SWNT density of electronic states. The cause of which can be seen in Figures 5.3a and b, where the probabilities that a particular state is filled with a hole is plotted on the same plot as the electronic band structure. The room temperature hole occupation probabilities, Pr*(p)*, are indicated with a color gradient and are determined by:

$$\Pr(p) = 1 - f(E) \tag{5.1}$$

where the Fermi function, *f(E)*, describes the probability that a state at a given energy (*E*) is filled with an electron. Figures 5.3a and b illustrate that a moderate doping level results in a Fermi energy shift of approximately 0.4 eV away from $E_{Fi}$. A Fermi energy shift of this magnitude is estimated for the as-made semiconducting film in Figure 5.3a, to account for the level of initial $S_{11}$ absorption bleaching. It has been shown that oxygen readily adsorbs on the surface of SWNTs resulting in oxidation of nanotubes and consequently an increase in the hole concentration within the valence band of semiconducting SWNTs [148] [130]. The reduced optical absorption of the $S_{11}$ energy transition is similar to that seen in chapter 4 for polydisperse films and is in agreement with other reports on the $S_{11}$ sensitivity to adsorbed oxygen [128]. Furthermore, a moderate level of oxygen doping also accounts for the appreciable conductivity of the semiconducting SWNT film. It is expected that an intrinsic semiconducting SWNT film would be substantially more resistive (i.e. not conductive) as other reports have shown [149]. In contrast, oxygen doping due to air exposure was not sufficient to induce salient changes in the absorption intensity of the $M_{11}$ intraband transition in the metallic SWNT film as suggested in Figure 5.3b.

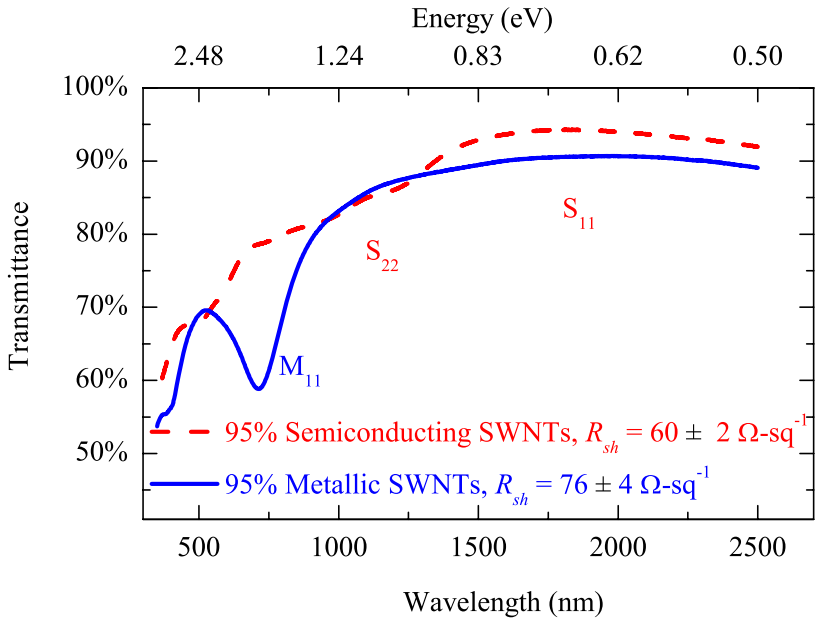


**Figure 5.4.** Optical transmittance versus wavelength for doped metallic and semiconducting SWNT films.

The optical transmittance spectra for doped metallic and semiconducting SWNT films are shown in Figure 5.4. The near complete bleaching of the $S_{11}$ and $S_{22}$ absorption peaks is indicative of hole doping that was sufficient to shift the Fermi energy beyond the second van Hove singularity in the valence band of semiconducting SWNTs. As illustrated in Figure 5.5a, a Fermi energy shift of approximately 0.8 eV from the intrinsic Fermi level would result in the occupation of holes in both van Hove singularities such that few electrons are present to transition to the mirror van Hove singularity in the conduction band. A similar absorption peak reduction at the $M_{11}$ energy transition is not observed in Figure 5.4 because of the energy differences of the van Hove singularities in metallic and semiconducting SWNTs as shown in the energy band diagrams in Figure 5.5. The first van Hove

singularity in metallic SWNTs is located approximately 0.9 eV from the intrinsic Fermi energy level, compared to 0.3 eV and 0.6 eV for the first and second van Hove singularities in semiconducting SWNTs, respectively. The level of doping was not sufficient to shift the Fermi energy in excess of 0.9 eV from $E_{Fi.}$, such that a significant occupation of holes in the van Hove singularity was achieved, as is illustrated in the figure.

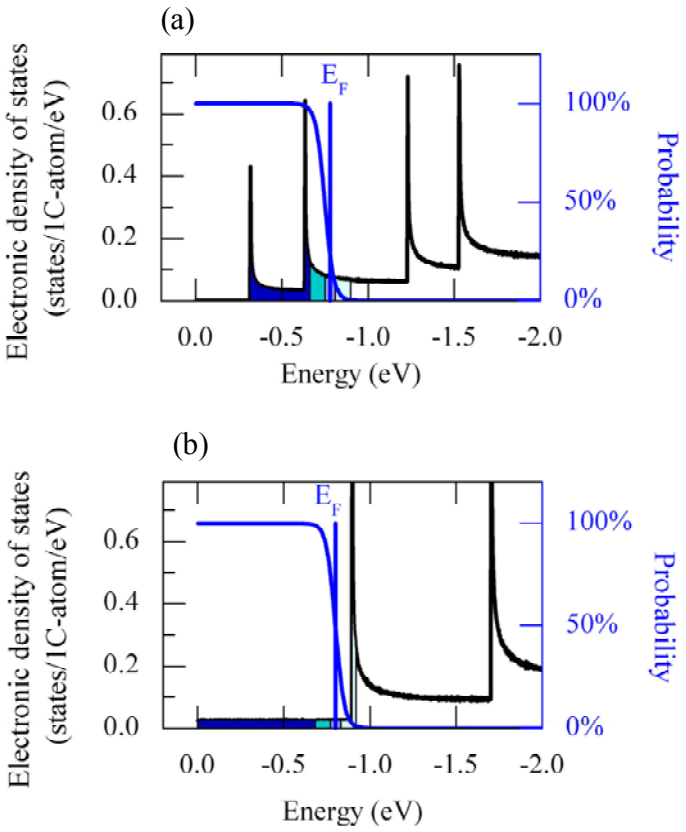


**Figure 5.5.** (a) (11,10) Semiconducting SWNT 1-D density of states with heavy doping (b) (10,10) Metallic SWNT 1-D density of states with heavy doping.

Chemical treatment of the semiconducting and metallic SWNT films was done to ascertain the impact of doping on films of different electronic type. As seen in

Figure 5.4, the doped metallic SWNT film was less conductive than the similarly doped semiconducting SWNT film with $R_{sh}$ values of 76 ± 4 Ω-sq$^{-1}$ and 60 ± 2 Ω-sq$^{-1}$, respectively. A similar trend was reported by Blackburn et al. [128]. This result can be understood by investigating the properties of individual semiconducting and metallic SWNTs. As shown in Figure 5.1, metallic SWNTs have a smaller number of electronic states at the Fermi energy, in comparison to bulk metals. This feature of metallic SWNTs allows them to be doped in such a manner as to shift the Fermi energy away from its intrinsic location. Therefore, the electronic behavior of a metallic SWNT more closely resembles the conceptual behavior of a bulk semiconductor with a nonzero density of states in the "pseudo band gap". As also illustrated in Figure 5.1 and 5.3, there is a larger density of electronic states near $E_F$ within the valence band of semiconducting SWNTs in comparison to metallic SWNTs at a similar energy level. The impact of the different electronic band structures of metallic and semiconducting SWNTs on electrical conduction may explain the superior optoelectronic properties of doped semiconducting SWNTs and will be discussed in the section to follow.

### 5.3. Electrical Conduction in Monodisperse SWNT Films

As discussed in Chapter 4, electrical conduction in SWNT films can be modeled as a parallel network with the resistance along a particular conduction path, $R_{path}$, in the film described as:

$$R_{path} = R_{SWNT-SWNT} + R_{SWNT} \tag{5.2}$$

where $R_{SWNT}$ and $R_{SWNT\text{-}SWNT}$ are the intratube and intertube SWNT resistances, respectively. Many reports have stated that conductance in SWNT films is overwhelmingly a function of $R_{SWNT\text{-}SWNT}$, due to the large intertube resistance, which was shown to be orders of magnitude higher than intratube resistance [105, 150]. However, in the case of primarily homogeneous SWNT films, there are several factors that suggest this is no longer the case. First, these reports are based on near-ballistic charge transport along carbon nanotubes, with an approximate mean free path, $\lambda$, on the order of 1 μm. While these reports present best case resistances, significant variability in the intratube resistance has been shown [151]. Furthermore, in SWNT networks, the mean free path of a charge carrier is significantly reduced, due to the existence of defects on the surface. The density of defects are considerably increased through processes such as acid-based purification [72] and ultrasonication [75] that are employed to achieve highly disperse, homogeneous solutions of purified nanotubes. While $\lambda$ is not known for these films, it is reasonable to expect it to be substantially lower than values used in previous studies that compared $R_{SWNT}$ to $R_{SWNT\text{-}SWNT}$. Also, as shown by Fuhrer et al. [152], the $R_{SWNT\text{-}SWNT}$ for nanotubes of similar electronic type is two orders of magnitude lower than the $R_{SWNT\text{-}SWNT}$ between metallic and semiconducting SWNTs. Therefore, in contrast to past comparisons of $R_{SWNT}$ to $R_{SWNT\text{-}SWNT}$, SWNT films of homogeneous electronic behavior may have comparable values for $R_{SWNT}$ and $R_{SWNT\text{-}SWNT}$ that merit investigation into the impact that both have on the overall conductivity of the film.

As also discussed in Chapter 4, hole doping of SWNT films can reduce $R_{path}$, since both $R_{SWNT}$ and $R_{SWNT\text{-}SWNT}$ can be decreased by the injection of additional p-type

charge carriers. The total density of holes is found by integrating the density of holes per unit energy, *p(E),* over all energies below $E_{Fi}$. *p(E)* is defined as the product of the density of states below $E_{Fi}$ and the probability that a particular state is not filled such that:

$$p(E) = g_v(E)\left[1 - f(E)\right] \tag{5.3}$$

where $g_v(E)$ and *f(E)* are the density of states below $E_{Fi}$ and the Fermi function respectively. It follows that the total density of holes, *p*, is found by:

$$p = \int p(E)dE = \int_{-\infty}^{E_{Fi}} g_v(E)\left[1 - f(E)\right]dE \tag{5.4}$$

Examination of Figure 5.5 with respect to Eq. (5.4) suggests that the doping process injected more holes into semiconducting nanotubes than in metallic nanotubes, given the estimated Fermi level position in the energy band structure and the corresponding hole occupation probability.

## 5.4. Impact of Chemical Doping

To confirm the level of hole doping that occurs in as-made and doped SWNTs, complimentary ultraviolet photoelectron spectroscopy (UPS), electrical sheet resistance, and UV-Vis-NIR spectroscopy measurements were made on representative monodisperse SWNT films (Figures 5.6 and 5.7). The UV-Vis-NIR spectra of an as-made and doped semiconducting SWNT film are shown in Figure 5.6. As expected,

the sheet resistance is reduced from 408 ± 28 Ω-sq$^{-1}$ to 136 ± 11 Ω-sq$^{-1}$ after chemical treatment and the $S_{11}$ and $S_{22}$ optical transitions are bleached. In the UPS spectra in Figure 5.6b, a shift of the low kinetic energy edge can be seen after doping the semiconducting SWNT film, which is indicative of an increase in the surface work function [132] as described in chapter 4. For each film, three locations were analyzed on the surface of the film. The spectra most representative of the average are shown. The average low kinetic energy edge and corresponding work function are summarized in Table 5.1. The range of low kinetic energy edges measured at the three locations on the film is also included in the table. A total work function increase of 0.4 eV is observed in doped semiconducting SWNTs, which is similar to the expected Fermi level shift from observations of the bleaching of the $S_{11}$ and $S_{22}$ transitions from the transmission spectra in Figure 5.2 and the electronic DOS in Figure 5.3. These results are consistent with other reports that show a shift of the Fermi level of SWNTs after doping [97, 108] and similar to the results of chapter 4 for heterogeneous SWNT networks comprised of ca. 66% semiconducting SWNTs. It must be noted that the lower sheet resistance of the doped semiconducting SWNT film in Figure 5.4 in comparison to the film in Figure 5.6 is because the film in Figure 5.4 has a higher concentration of nanotubes, as indicated by its lower transmittance in the visible spectrum.

**Table 5.1.** Work function of as-made and doped semiconducting SWNT films.

| | $KE_{low}$ | | Work function, $\Phi$ |
|---|---|---|---|
| | Range (eV) | Average (eV) | Average (eV) |
| As-made | [15.49, 15.53] | 15.5 | 4.6 |
| Doped | [15.84, 15.88] | 15.9 | 5.0 |

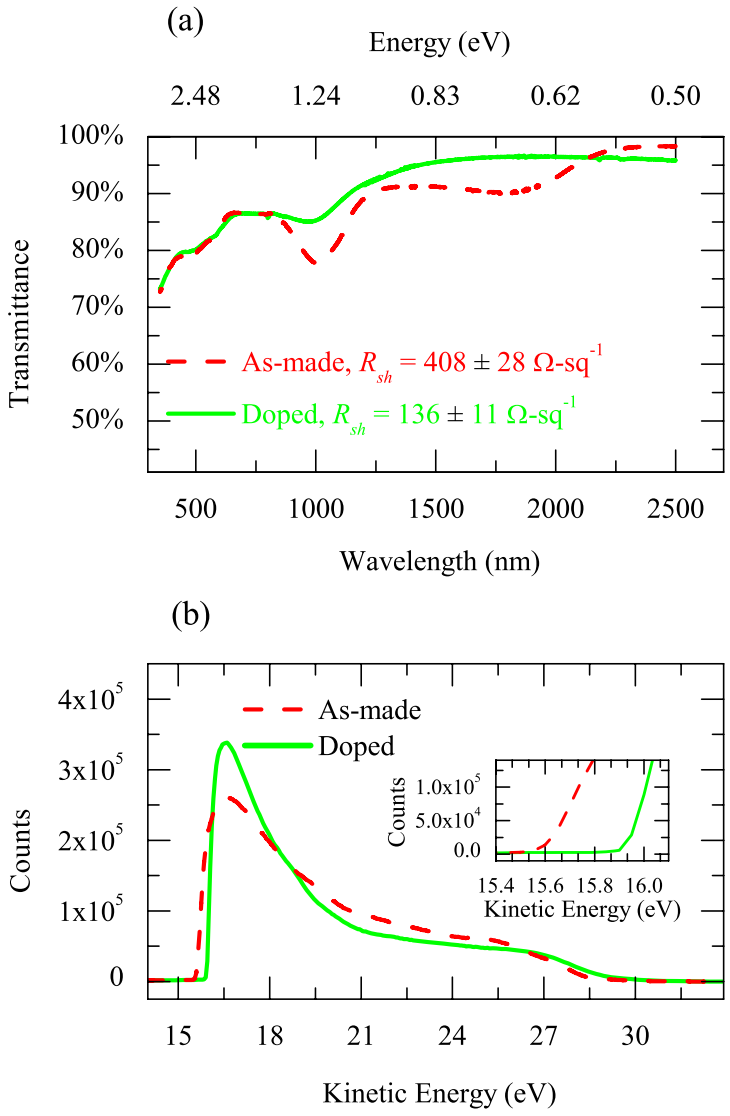


**Figure 5.6.** (a) Optical transmittance spectra of as-made and doped semiconducting SWNT films. (b) Representative UPS spectra of as-made and doped semiconducting SWNT films. Inset: Low kinetic energy edge of provided spectra.

Shown in Figure 5.7 are the UV-Vis-NIR spectra of an as-made and a doped metallic SWNT film. The optical behavior of the small percentage (≤ 5%) of semiconducting SWNTs remaining in the metallic film suggests that the initial Fermi level position was in a similar location as the as-made semiconducting SWNT film.

The work function of an as-made metallic SWNT film derived from UPS spectra in Figure 5.7b provides further verification of this observation. The average low kinetic energy edge and corresponding work function are summarized in Table 5.2. The range of low kinetic energy edges measured at three locations on the film is also included in the table. After doping via chemical treatment, the work function increased by 0.4 eV, an amount similar to that seen for the semiconducting SWNT film. Likewise, decrease in the electrical sheet resistance from 212 ± 1 Ω $sq^{-1}$ to 124 ± 10 Ω $sq^{-1}$ occurred after chemical treatment. However, the change in $R_{sh}$ for the metallic SWNT film was considerably smaller than the change in resistance seen for the semiconducting film after doping. As illustrated in Figure 5.3, a Fermi level shift that does not exceed the energy of the first metallic van Hove singularity results in substantially fewer holes, $p$, being injected into metallic SWNTs in comparison to the total number of holes gained by semiconducting SWNTs. These results provide experimental support of the estimated shifts in the Fermi level energy of the SWNT films due to doping, shown in Figures 5.3 and 5.5. Therefore, the observed smaller sensitivity of $R_{sh}$ of the metallic SWNT film in comparison to the sensitivity of $R_{sh}$ of the semiconducting SWNT film is consistent with the previous discussion of the impact of increased charge carriers on the magnitude of $R_{path}$. Also, other studies have shown similar trends [128, 149].

**Table 5.2.** Work function of as-made and doped metallic SWNT films.

| | $KE_{low}$ | | Work function, $\Phi$ |
|---|---|---|---|
| | Range (eV) | Average (eV) | Average (eV) |
| As-made | [15.41, 15.32] | 15.4 | 4.5 |
| Doped | [15.86, 15.90] | 15.9 | 5.0 |

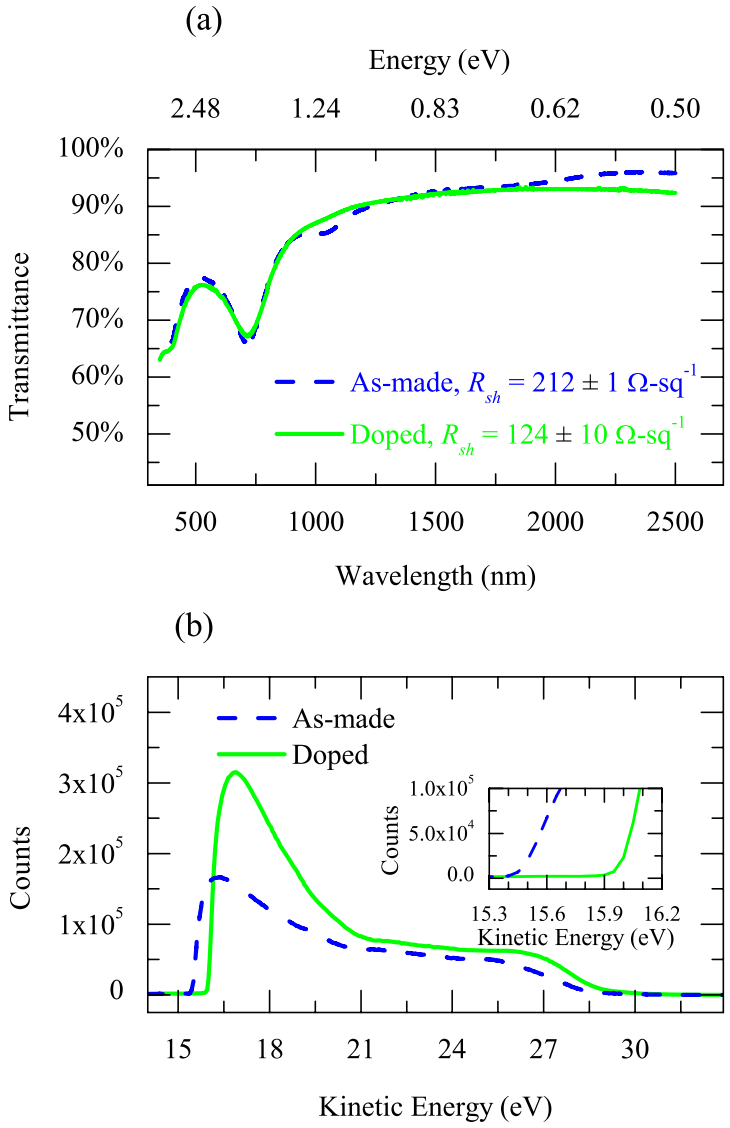


**Figure 5.7.** (a) Optical transmittance spectra of as-made and doped metallic SWNT films. (b) UPS spectra of as-made and doped semiconducting SWNT films.

### 5.5. Impact of Annealing SWNT Films

In order to determine the optoelectronic impact of oxygen adsorbed on the surface of the SWNTs in prepared films, as-made SWNT films were annealed and investigated. As discussed for the heterogeneous SWNT networks studied in Chapter

4, adsorbed oxygen can significantly affect the optical and electronic properties of SWNTs. Shown in Figure 5.8 are the optical transmittance and UPS spectra of a semiconducting SWNT film as-made and after annealing.

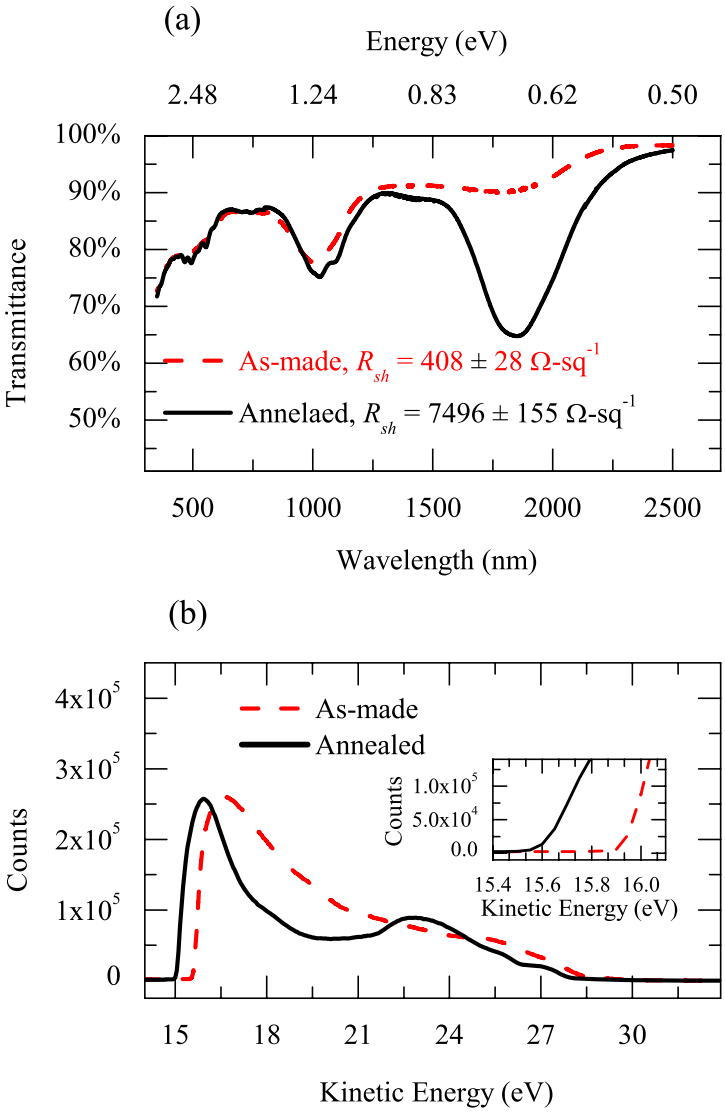


**Figure 5.8.** (a) Optical transmittance spectra of as-made and annealed semiconducting SWNT films. (b) UPS spectra of as-made and annealed semiconducting SWNT films.

After annealing, the following occurred: a) an increase in the $S_{11}$ absorption peak in the film transmittance spectrum (Figure 5.8a), b) a shift in the surface work function to a lower energy (Figure 5.8b), and c) an increase in the sheet resistance of the film from 408 ± 28 Ω-sq$^{-1}$ to 7496 ± 155 Ω-sq$^{-1}$. The increase in the $S_{11}$ absorption peak is due to the removal of adsorbed oxygen species present on the SWNT surface prior to annealing. As described in chapter 4, electrons replaced hole dopants in the valence band up to the first van Hove singularity and as a consequence, photon energies equal to the $S_{11}$ electronic interband transition were absorbed as evidenced in the spectra in Figure 5.8a. Further support of a reduction in the percentage of oxygen present on the as-made SWNT film after annealing is provided by the XPS measurements in Figure 5.9. In the figure, the binding energy peaks from the 1s core electrons from carbon and oxygen are identified at 285 eV and 532 eV, respectively. The atomic ratio of carbon and oxygen were determined for both samples and summarized in Table 5.3. The remaining amount of oxygen in the annealed sample can likely be attributed to carboxylic acids bonded to the SWNTs to aid in dispersion in solution and other non-oxidative oxygen species. Also, the work function decrease of approximately 0.5 eV (Table 5.4) is consistent with a shift of $E_F$ to higher energies due to the loss of hole dopants. Finally, because oxidation from chemi-adsorbed oxygen resulted in the degenerate doping of semiconducting SWNTs, $R_{sh}$ is increased by more than an order of magnitude after annealing, as $E_F$ is shifted from within the valence band to the energy band gap. A similar trend of increased electrical resistance with $E_F$ shifts was reported by Wu et al. [77]. However, unlike the tests performed in this dissertation that utilized chemical charge transfer doping,

Wu et al. used electric fields to modulate the Fermi level position via a field effect transistor. Also, these results are similar to the trend observed for the heterogeneous mixture of SWNTs studied in Chapter 4, where $R_{sh}$ increased from 367 ± 10 Ω-sq$^{-1}$ to 2611 ± 204 Ω-sq$^{-1}$. The larger increase of $R_{sh}$ in this semiconducting film is due to the absence of a significant number of metallic SWNTs remaining in the film to form high conducting pathways. Unlike the mixed SWNT film with approximately 33% metallic SWNTs by composition, the percentage of metallic SWNTs in the semiconducting SWNT film was less than 5%.

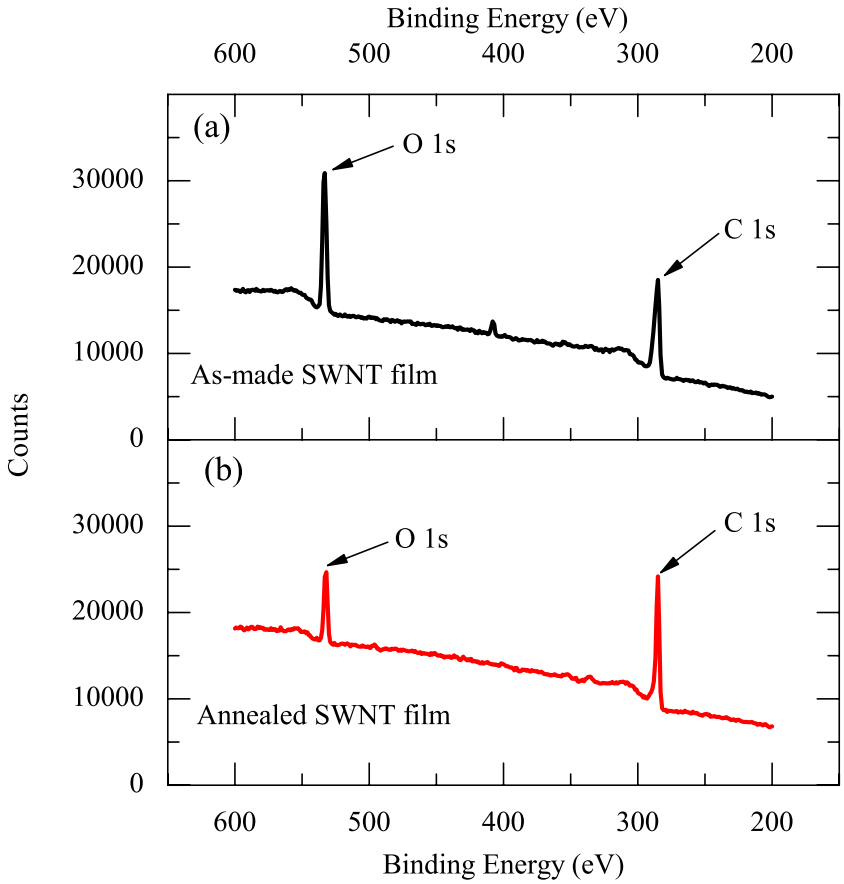


**Figure 5.9.** XPS spectra for (a) as-made semiconducting SWNT film and (b) annealed semiconducting SWNT film.

**Table 5.3.** Summary of the atomic ratio of oxygen to carbon ratio in the semiconducting SWNT films, as determined from XPS spectra.

| | O:C | |
|---|---|---|
| | Range | Average |
| As-made film | [0.311 , 0.357] | 0.333 |
| Annealed film | [0.184 , 0.193] | 0.189 |
| Percent change | | -43% |

**Table 5.4.** Work function of as-made and annealed semiconducting SWNT films.

| | $KE_{low}$ | | Work function, $\Phi$ |
|---|---|---|---|
| | Range (eV) | Average (eV) | Average (eV) |
| As-made | [15.49, 15.53] | 15.5 | 4.6 |
| Annealed | [14.90, 15.00] | 15.0 | 4.1 |

The optical spectra of an as-made and annealed metallic SWNT film are shown in Figure 5.10a. After annealing, no salient changes occurred in the metallic $M_{11}$ absorption peak. However, the non-negligible amount of semiconducting SWNTs (< 5%) revealed that desorption of oxygen species did occur during annealing, due to increased absorption located at wavelengths equivalent to the $S_{11}$ and $S_{22}$ energy transitions. The XPS spectra shown in Figure 5.11 and the summary of oxygen to carbon ratios in the as-made and annealed films (Table 5.5) provide further evidence of oxygen reduction on the surface of the film. Also, the UPS spectra (Figure 5.10b) and subsequent analysis (Table 5.6) show that a similar work function decrease to 4.1 eV occurred after annealing as was seen for the semiconducting SWNT film discussed earlier. However, unlike semiconducting SWNTs that contain an energy band gap with no electronic states above the first van Hove singularity, metallic SWNTs have a non-zero density of states throughout the band

structure and therefore remain conductive even after annealing. As such, the metallic SWNT film exhibited a much smaller increase in sheet resistance after annealing than the semiconducting SWNT film, even though a similar change in work function occurred, along with a similar reduction in adsorbed oxygen. The sheet resistance of the metallic SWNT film increased from 212 ± 1 Ω-sq$^{-1}$ to 306 ± 7 Ω-sq$^{-1}$.

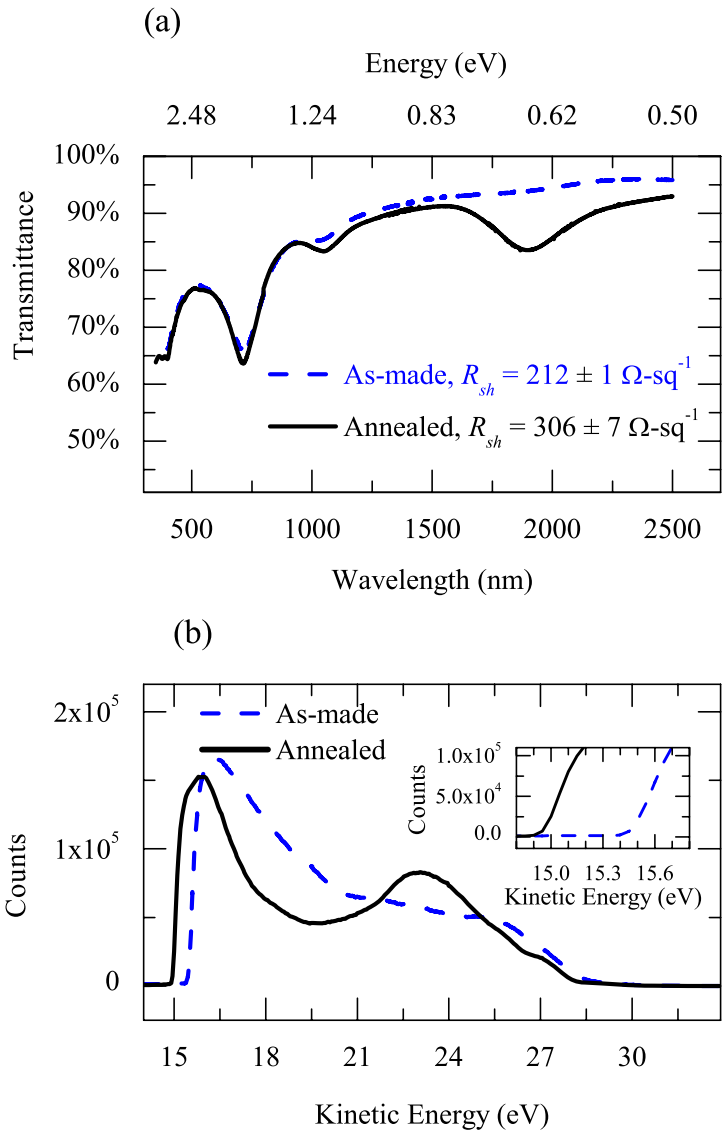


**Figure 5.10.** (a) Optical transmittance spectra of as-made and annealed metallic SWNT films. (b) UPS spectra of as-made and annealed metallic SWNT films.

It must be noted that the surface work function determined by UPS measurements include the Fermi level position of the sample as well as any surface dipoles created on the surface. Therefore, the Fermi level shift cannot be determined exactly by UPS measurements. However, the trends and direction of the Fermi level shift ascertained from UPS analysis corroborate UV-Vis-NIR spectra, XPS measurements, and electrical observations.

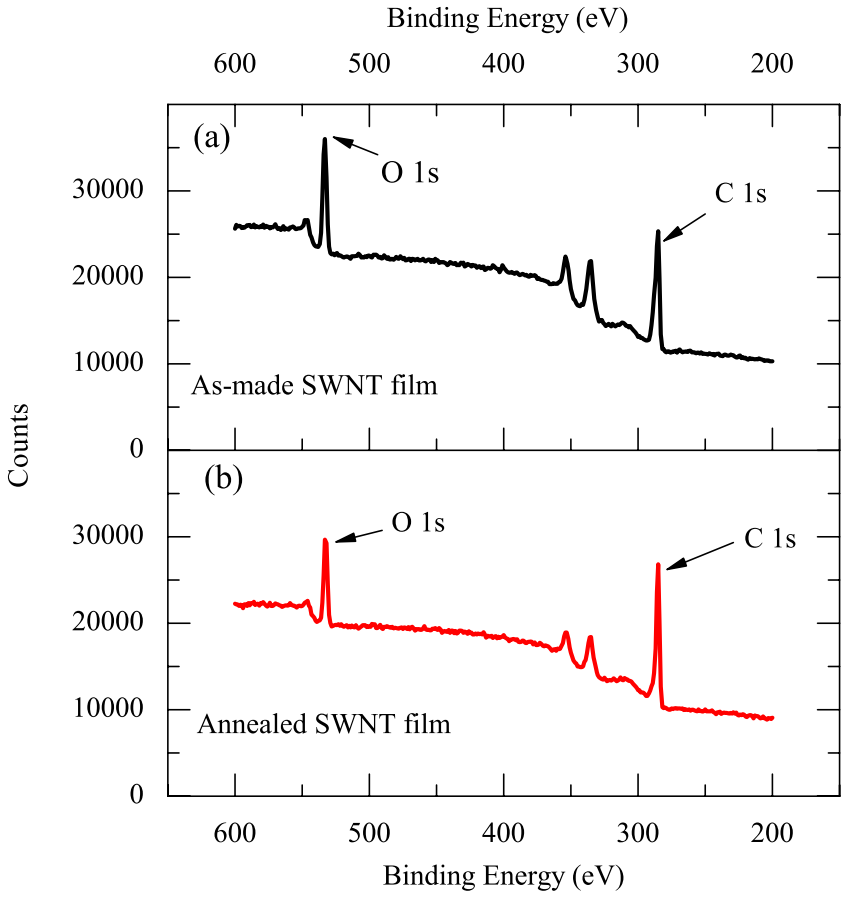


**Figure 5.11.** XPS spectra for (a) as-made metallic SWNT film and (b) annealed metallic SWNT film.

**Table 5.5.** Summary of the atomic ratio of oxygen to carbon ratio in the metallic SWNT films as determined from XPS spectra.

| | O:C | |
|---|---|---|
| | Range | Average |
| As-made film | [0.262 , 0.376] | 0.316 |
| Annealed film | [0.205 , 0.208] | 0.207 |
| Percent change | | -35% |

**Table 5.6.** Work function of as-made and annealed metallic SWNT films.

| | $KE_{low}$ | | Work function, $\Phi$ |
|---|---|---|---|
| | Range (eV) | Average (eV) | Average (eV) |
| As-made | [15.41, 15.32] | 15.4 | 4.5 |
| Annealed | [15.04, 14.98] | 15.0 | 4.1 |

## 5.6. Air Stability of Monodisperse SWNT Films

### 5.6.1. Air Stability of Semiconducting SWNT Films

A further measure of the relative optoelectronic differences of metallic and semiconducting SWNTs is shown in Figures 5.12 and 5.13. The evolution of $R_{sh}$ is shown as a function of exposure time to ambient conditions. To complement electrical stability observations, transmittance measurements were taken at exposure times of 3, 116, and 266 hours for each film.

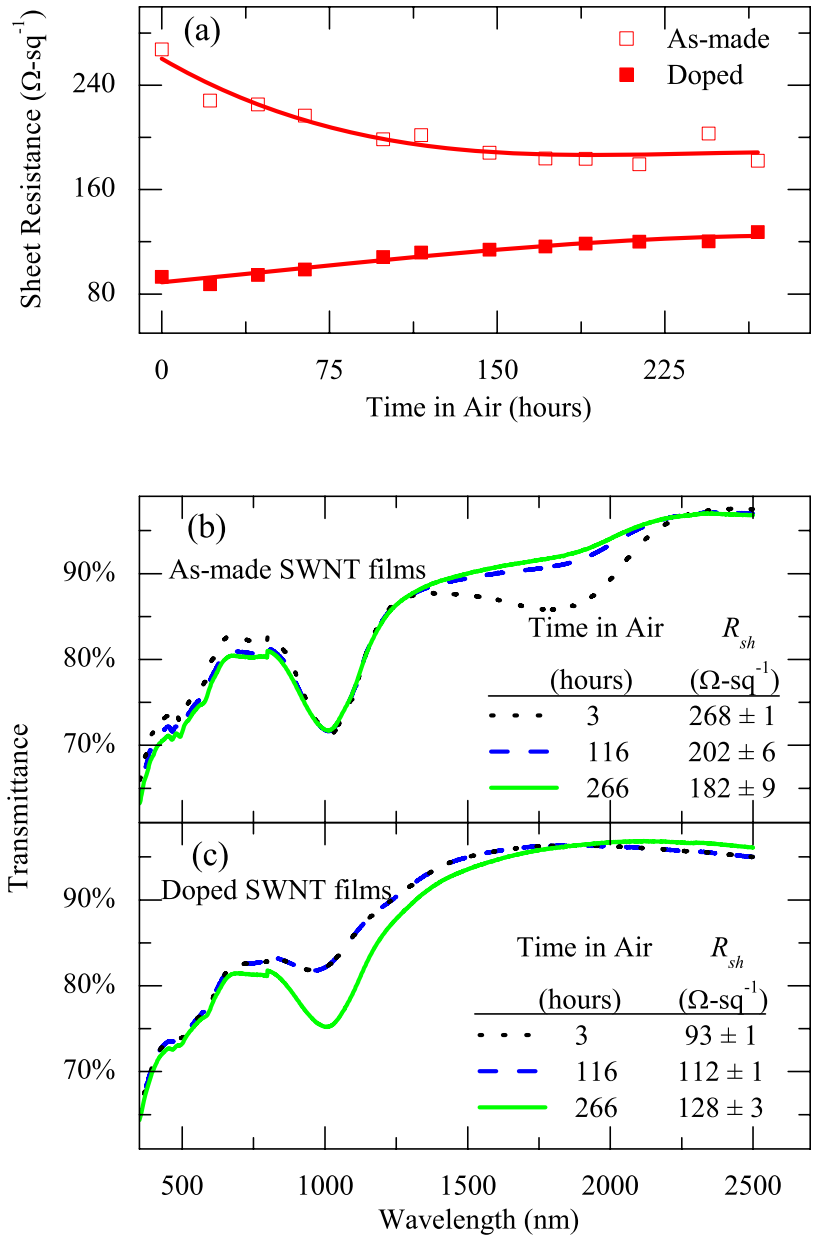


**Figure 5.12.** (a) Electrical sheet resistance versus time in air for semiconducting SWNT films. Lines are shown as a guide to the eye. (b) Optical transmittance versus wavelength for as-made semiconducting SWNT film taken at air exposure times of 3, 116, and 226 hours. (c) Optical transmittance versus wavelength for doped monodisperse semiconducting SWNT films taken at air exposure times of 3, 116, and 226 hours.

In the case of the as-made semiconducting SWNT film in Figure 5.12a, exposure to ambient air resulted in increased oxygen adsorption which in turn increased the hole carrier concentration, such that $R_{sh}$ decreased with time. Increased hole doping was further evidenced in Figure 5.12b as the absorption peak from the $S_{11}$ energy transition reduced as exposure time increased. Upon doping via chemical treatment, $R_{sh}$ for the semiconducting SWNT film was significantly reduced as observed in Figure 5.12c. Concurrently, the $S_{11}$ transition was completely bleached, while the $S_{22}$ transition was significantly reduced due to hole doping from the chemical treatment. However, as has been shown in chapter 4, the doping effects of $HNO_3$ and $SOCl_2$ are reversible upon air exposure, which can be seen in the increased value of $R_{sh}$ with time. An increase in the absorption intensity of the $S_{22}$ energy transition is seen in Figure 5.12c as the Fermi level shifted upward towards the intrinsic Fermi level due to loss of chemical dopants. Nevertheless, it must be noted that the $S_{11}$ transition remained bleached, indicating the location of the Fermi level was between $S_{11}$ and $S_{22}$ van Hove singularity.

### 5.6.2. Air Stability of Metallic SWNT Films

The electrical stability of as-made metallic SWNTs exhibited distinctly different behavior than similarly processed semiconducting SWNTs. Instead of a reduction of $R_{sh}$ as seen in semiconducting SWNTs with increased exposure time, $R_{sh}$ increased slightly by approximately 10% as seen in Figure 5.13. Also, the optical absorption spectra remained constant with no salient changes. While unexpected, the increase of $R_{sh}$ is likely significant since it exceeds the relative error of the TLM procedure of 3% determined in chapter 3. It is expected that oxygen did adsorb on the surface of metallic SWNTs to effectively hole dope the SWNTs through oxidation in a similar manner to the

process observed in semiconducting SWNTs. However, because the density of states between the intraband $M_{11}$ energy transition is relatively small, the cumulative amount of injected charge carriers was also sufficiently small such that an associated increase in conductivity did not occur. It is possible that adsorbed oxygen can reduce the charge mobility in SWNTs due to a decreased mean free path, thereby resulting in a slight increase in $R_{sh}$. While this could also occur in semiconducting SWNTs, the density of charge carriers injected into the film would more than compensate for any reduction in mobility.

In contrast to the as-made metallic SWNT film, the doped film behaved similarly to doped semiconducting SWNTs. $R_{sh}$ initially decreased by more than 40% due to doping. With increasing exposure time, $R_{sh}$ increased, consistent with a loss of p-type dopants. A slight increase in the $M_{11}$ absorption peak with time was also observed in Figure 5.13c. While smaller in magnitude, the increase was akin to the increase in the $S_{22}$ peak observed in doped semiconducting SWNTs with time. This observation further supports an understanding that the Fermi level in the metallic SWNTs was initially shifted downward into the electronic band structure of the SWNT due to p-doping as was done in the semiconducting SWNTs. However, the initial decrease in $R_{sh}$ is not as large as was observed in the semiconducting SWNTs, and consequently, the subsequent increase in $R_{sh}$ was smaller. This effect can likewise be understood in terms of the limited density of available states for injected holes between the intraband $M_{11}$ transition in comparison to the states available in the valence band of semiconducting SWNTs. Succinctly, since fewer holes were initially injected into the metallic SWNT film to fill

the fewer number of available states in the *DOS*, fewer charges were lost as a function of time.

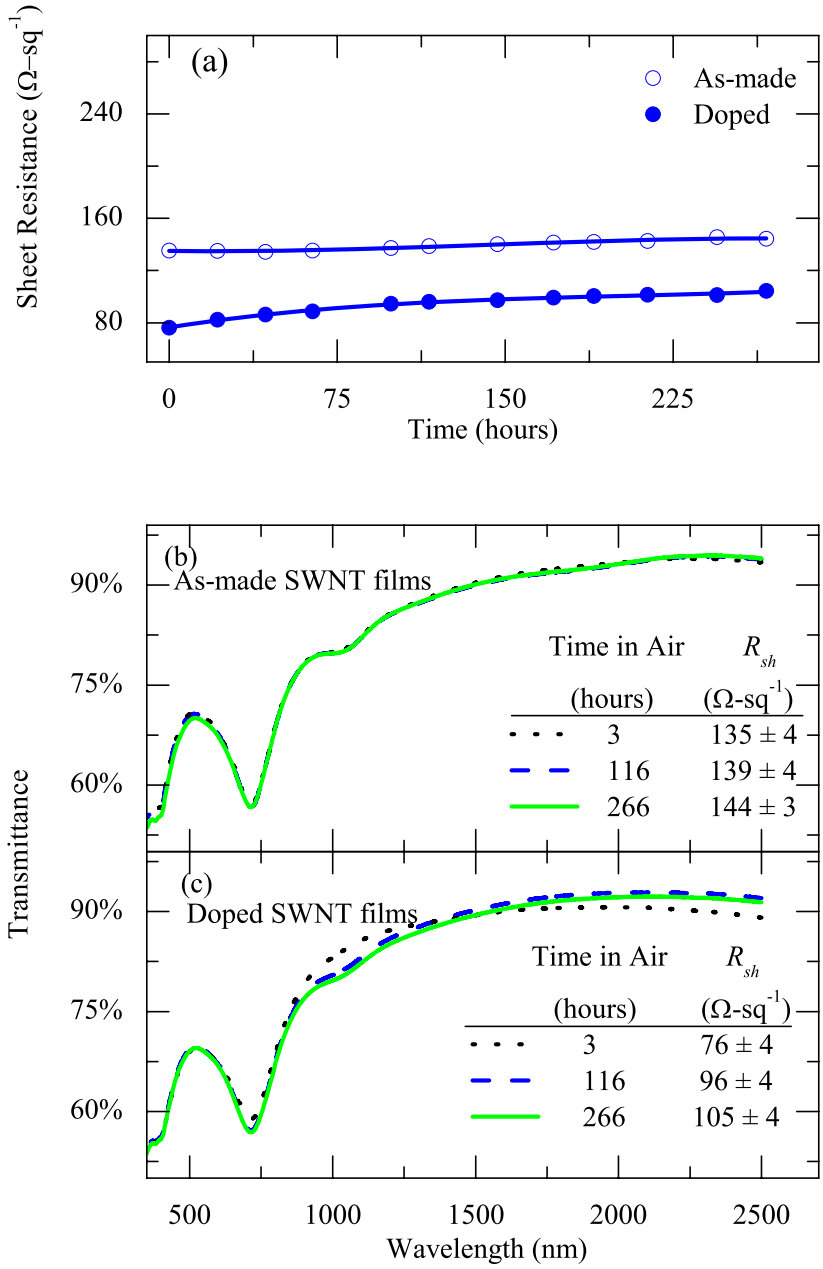


**Figure 5.13.** (a) Electrical sheet resistance versus time in air for metallic SWNT films. (b) Optical transmittance versus wavelength for as-made metallic SWNT films taken at air exposure times of 3, 116, and 226 hours. (c) Optical transmittance versus wavelength for doped metallic SWNT films taken at air exposure times of 3, 116, and 226 hours.

## 5.7. Comparison of the Air Stability of Polydisperse and Monodisperse SWNT Films

The air stability of as-made and doped polydisperse SWNT films was discussed in Chapter 4. $R_{sh}$ of both monodisperse and polydisperse SWNT films doped with $HNO_3$ and $SOCl_2$ increased with additional air exposure. In contrast, the stability of $R_{sh}$ of as-made metallic, semiconducting, and polydisperse films was different for each type. However, the resulting differences are reasonable. Since the polydisperse film was a mixture of metallic and semiconducting SWNTs, it is expected that it would have an electrical behavior representative of both electronic types. As shown in the previous section, $R_{sh}$ for the metallic film increased with time, while it decreased in the semiconducting film. Therefore, the observation of no change in $R_{sh}$ of the polydisperse SWNT film with time could be interpreted as the result of the interaction between the metallic and semiconducting SWNTs.

## 5.8. Verification of Metallic to Semiconducting Ratio

As can be seen in the UV-Vis-NIR spectra of annealed metallic SWNT films (e.g. Figure 5.10), a non-negligible amount of semiconducting SWNTs appear to be present by the emergence of $S_{11}$ and $S_{22}$ absorption peaks. It is widely accepted in the SWNT research community that as-received SWNT powders consist of a 2:1 ratio of semiconducting to metallic SWNTs, as discussed in Chapter 2. As such, a UV-Vis-NIR spectra of a polydisperse SWNT film was used to establish the composition of semiconducting SWNTs in the metallic film. Since semiconducting and metallic SWNTs have characteristic absorption peaks that are clearly distinguishable, the integrated area under these peaks can be used to ascertain the relative composition. Because the

absorption peak caused by the $S_{11}$ energy transition is highly sensitive to air exposure, the absorption peak due to the $S_{22}$ peak was used as the determinant of semiconducting SWNT composition [128]. The ratio of semiconducting SWNTs to metallic SWNTs in the metallic film, $R_{metallic}$, was determined by:

$$\frac{\left.\frac{A_S}{A_M}\right|_{polydisperse}}{\left.\frac{A_S}{A_M}\right|_{metallic}} = \frac{R_{polydisperse}}{R_{metallic}} \tag{5.5}$$

where $A_s$, $A_m$, $R_{polydisperse}$, are the integrated area under the $S_{11}$ peak, the integrated area under the $M_{11}$ peak, and the ratio of semiconducting to metallic SWNTs in a polydisperse SWNT film, respectively. The films investigated are shown in Figure 5.14, in which the integrated areas are shaded. The computed percentage of semiconducting SWNTs in this film was 4.99%, which is consistent with the manufacturer's specifications for purchased monodisperse SWNT solutions.

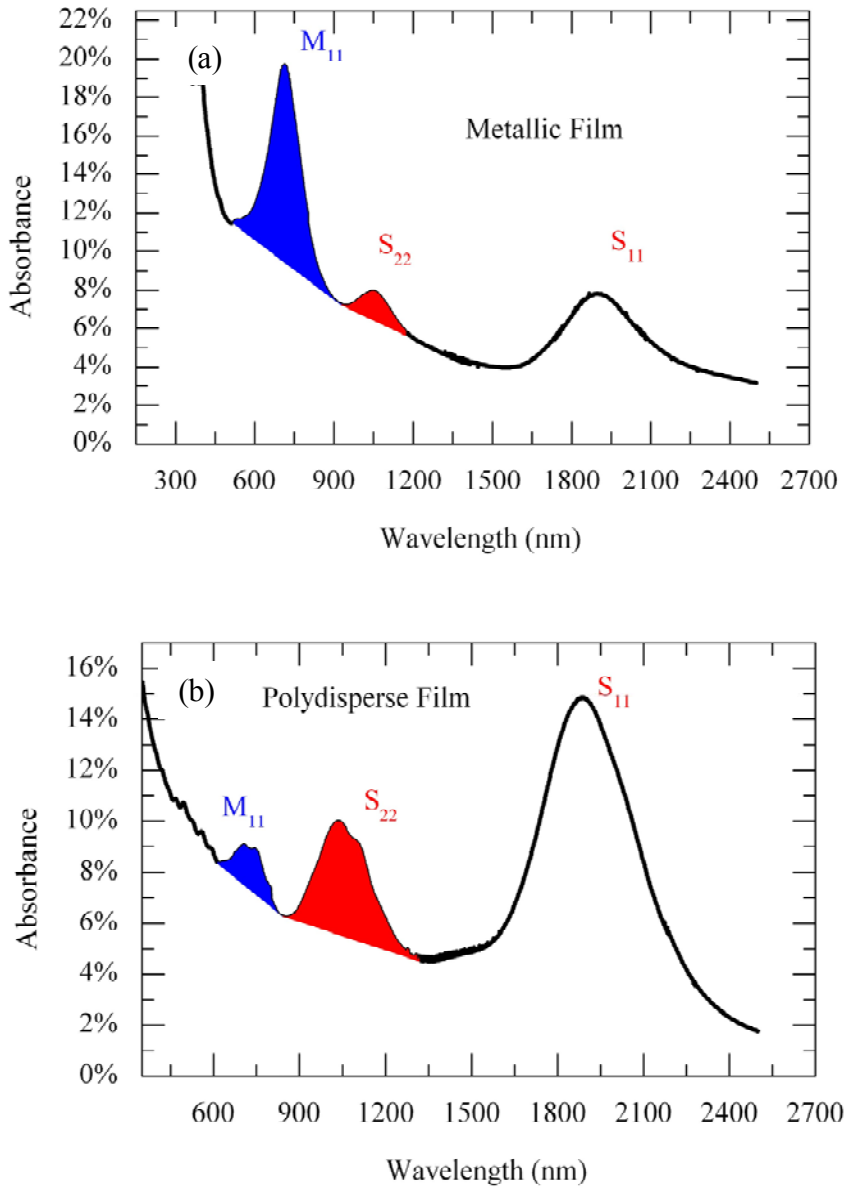


**Figure 5.14.** Absorbance versus wavelength for (a) metallic SWNT films and (b) polydisperse SWNT films. $A_s$, and $A_m$ are shaded to illustrate the absorbance contribution from semiconducting and metallic SWNTs, respectively.

## 5.9. Conclusion

The goal of this chapter was to present a clear description of the optoelectronic behavior of SWNT films of metallic or semiconducting electronic type. Similar to the

trend reported by Blackburn et al. [128], doped semiconducting SWNT films were found to be more optoelectronically favorable than doped metallic SWNT films. Because absorption at the first and second van Hove singularities in the semiconducting SWNTs was effectively removed via doping, films of degenerately doped semiconducting SWNTs exhibited lower transmission losses in the visible spectrum in addition to higher electrical conductivity. It was concluded that a greater number of free charge carriers were induced in doped semiconducting SWNTs than in metallic SWNTs due to the distinct differences in their intrinsic electronic density of states. Photoelectronic spectroscopy, $R_{sh}$ evaluation, and UV-Vis-NIR were presented to provide experimental corroboration of this theoretical conclusion. A larger number of free charge carriers injected into semiconducting SWNTs resulted in higher electrical conductivity in comparison to metallic SWNTs. In addition, the optical wavelength range most important to organic electronics is from 400 nm to 800 nm. Not only is the metallic absorption peak at the $M_{11}$ energy transition positioned in this range (~700 nm), it is not as susceptible to removal as the $S_{11}$ and $S_{22}$ peaks in semiconducting SWNTs. Therefore, SWNT films that contain a large portion of metallic SWNTs will also exhibit similar absorption losses in the visible spectrum as was evident in the doped polydisperse SWNT film studied in Chapter 4. Also, the significant variation in work function of as-made, annealed, and chemically doped monodisperse SWNT films was quantified and presented in this chapter. This detailed account represented the first summarized report of such data.

The results of this chapter suggest that the 1-D nature of SWNTs requires an unconventional approach to maximize their utility in electronic devices. While it is

expected that a film of homogeneous electronic type would provide superior electronic behavior, the analysis of monodisperse metallic and semiconducting SWNTs proved counterintuitive. In contradistinction to traditional methods that seek all metallic networks to achieve high conducting electrodes, degenerately doped semiconducting SWNTs may provide the optimal path to this goal. On the other hand, because $R_{sh}$ in metallic SWNTs is less sensitive to the Fermi level position, low work function networks of metallic nanotubes may also find utility as the negative electrode in organic electronics.

# CHAPTER 6: SPECIFIC CONTACT RESISTANCE AT METAL/SWNT INTERFACES

## 6.1. Introduction

While SWNT electrodes presented in chapters 2 – 5 have shown significant promise as a transparent electrode material, the resistive power losses arising from its sheet resistance remain a considerable barrier to the scaling of OPV devices for large area applications. Both ITO and SWNT electrodes have sheet resistance values comparable to the top emitter used in Si-based photovoltaics, which can lead to excessive resistive power losses. As a result, the integration of a metallic grid system is required in Si-based photovoltaics to mitigate these losses. Grid systems are comprised of low resistivity metallic fingers and busbars to assist in charge collection from the solar cell and thereby reduce the contribution of the emitter's sheet resistance to system level losses (Figure 6.1a). Due to similar concerns in the use of SWNT electrodes in OPVs, a metallic grid deposited on SWNT electrodes may also effectively reduce the lateral path that photogenerated electrical charges must traverse in the SWNT network before they are collected in low resistance metal fingers (Figure 6.1b). However, an additional resistive loss is formed at the interface between the SWNT electrode and the metal in the form of contact resistance.

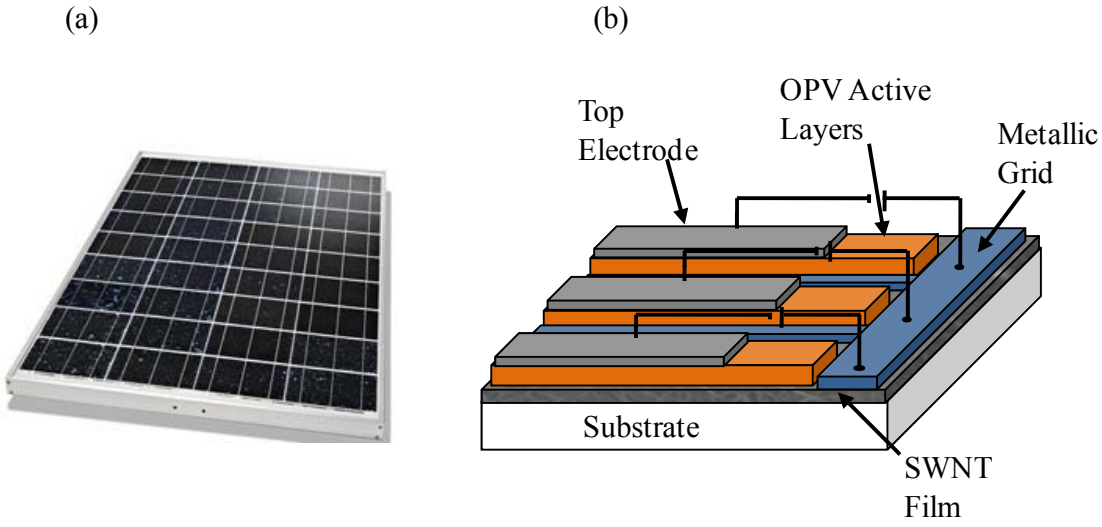


**Figure 6.1.** (a) Commercial silicon solar cell panel with metallic grids and busbars (www.midsummerenergy.co.uk). (b) Proposed OPV architecture incorporating a metallic grid system.

Figure 6.2 illustrates the path of current and the associated resistances within the electrode and at the metal/SWNT interface. In order to maintain minimum overall series resistance in system integration, it is essential that low contact resistance, $R_c$, exist between the SWNTs and the metallic fingers deposited on the electrode surface. To address this need, this section will explore the interfacial electrical contact resistance between the metal fingers and randomly distributed SWNT networks, providing the first ever data on such contact parameters. In addition, this study will also project the impact on power losses due to contact resistance in OPVs.

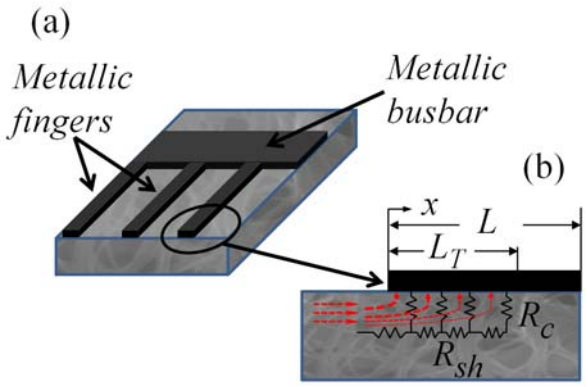


**Figure 6.2.** (a) Illustration of metallic grid deposited on SWNT film. (b) Schematic diagram of current and resistance distribution in electrode and electrode/contact interface.

## 6.2. Derivation of the Specific Contact Resistance from the Transfer Length Method

$R_c$ can be best understood as a series resistance at the contact interface that describes the deviation of an actual contact from an ideal condition [153]. In this regard, an ideal condition would exhibit no interfacial layers between the metal and semiconductor in contact. As described by Berger [153], the departure from ideal conditions can be attributed to the thin accumulation/depletion layer that develops in the semiconductor material. This layer on the surface of the semiconductor arises from work function differences of the metal and semiconductor or because of surface states of the semiconductor that exist in the energy bandgap. The difference in actual and ideal contact can also be derived from any lack of intimate contact at the metal/semiconductor interface and local chemistry between the two surfaces [154]. $R_c$ is intrinsically dependent upon the contact geometry and associated area. However, a quantity to describe the quality of the metal/semiconductor contact independent of contact area is

desired. To this end, the specific contact resistance, $\rho_c$, is commonly used and in practice is described as [155]:

$$\rho_c = R_c * A \tag{6.1}$$

with units of Ω-cm$^2$, where $A$ denotes the contact area at the metal/semiconductor interface. $\rho_c$ provides a convenient parameter to compare contacts of various sizes.

While series resistance parameters such as $R_{sh}$ can be measured, $\rho_{c,}$ must be obtained from other quantifiable properties. Multiple methods exist for deriving $\rho_{c,}$ among which exist the cross-bridge Kelvin resistor contact test structure proposed by Shih et al. [156], the contact end resistance test structure [157], and the transfer length method, TLM, an extension of the transmission line method originally suggested by Shockley [158]. The TLM is commonly used in practice and has been shown to be more pertinent and reliable for derivation of $\rho_c$ in p-type semiconductor/metal ohmic contacts [159]. Furthermore, the TLM provides a convenient method where $R_{sh}$, $R_c$, and the characteristic transfer length, $L_T$ can be simultaneously extracted. Therefore, TLM is used to ascertain $\rho_c$ to assess the quality of the SWNT/metal contacts.

The TLM is based on the premise that current crowding occurs at the edge of the metal contact resulting in a nonhomogenous flow of current from the semiconductor to the metal. A transfer length can be defined such that [160]

$$L_T = \sqrt{\frac{\rho_c}{R_{sh}}} \tag{6.2}$$

where $L_T$ can be described as the length over which 1/e of the current has been transferred from the semiconductor to the metal [159]. As can be observed from Figure 6.2, if the contact resistance is very low with respect to the sheet resistance of the semiconductor, $L_T$ will be small such that most of the current will transfer near the edge of the metal contact. Conversely, if sheet resistance is low or the contact resistance is high, $L_T$ will be large [161]. With this in mind, it is obvious that $L_T$ can never exceed $L$.

To allow the extraction of $R_{sh}$, $R_c$, and $L_T$, the TLM test structure consists of multiple metal pads at different spacings, $d_i$, deposited onto the semiconductor, as shown in Figure 6.3.

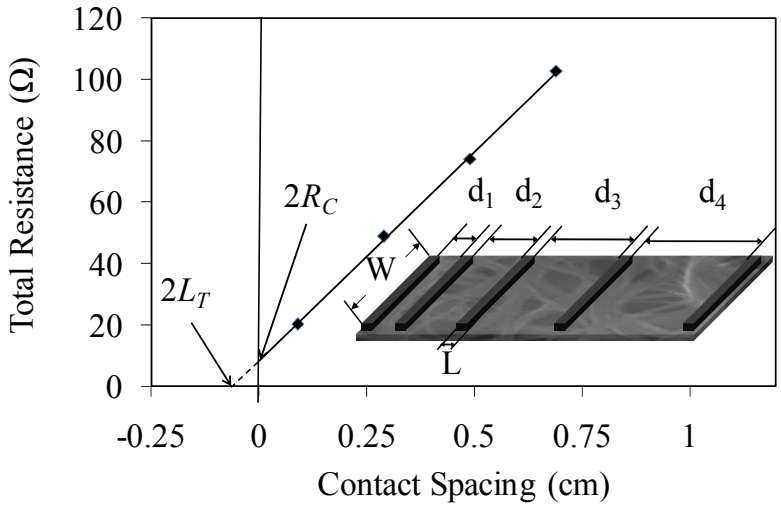


**Figure 6.3.** TLM test structure with a representative plot of total resistance, $R_T$, versus contact spacings, $d_i$, of 0.9 mm, 2.9 mm, 4.9 mm, and 6.9 mm. The extraction of $R_c$ and $L_T$ are illustrated.

The total resistance, $R_T$, is measured between each contact spacing and plotted versus $d$ and a least squares fit of $R_T$ can be approximated by [124]:

$$R_T = 2R_c + R_{sh} * \frac{d}{W} \tag{6.3}$$

However for the transmission line model, $R_c$ meanwhile can be further simplified to be equal to [153]:

$$R_c = \frac{R_{sh} * L_T}{W} \coth\left(\frac{L}{L_T}\right) \tag{6.4}$$

and for $L \geq 2 * L_T$, eq (6.4) can be simplified to

$$R_T = \frac{2R_{sh} * L_T}{W} + R_{sh} * \frac{d}{W} \tag{6.5}$$

### 6.3. Specific Contact Resistance Results and Discussion

A shadow mask was used to define the contact pads at spacings ($d_i$) of 0.09 cm, 0.29 cm, 0.49 cm, and 0.69 cm. The length ($L$) and width ($W$) of the contact pads were 0.1 cm and 1 cm respectively, as illustrated in Figure 6.3. The total resistance ($R_T$) was measured between silver pads for each contact spacing and plotted versus $d$. The least squares fit of $R_T$ versus contact spacing was approximated by Eq. (5.3) to

permit the extraction of $R_{sh}$ and $R_c$. $L_T$ and $\rho_c$ can subsequently be determined from Eq. (6.5) and Eq. (6.2) respectively. To validate the utility of the TLM in this application, ohmic contact between the metal pads and the SWNT film was verified with the observation of a linear current-voltage (I-V) relationship in both forward and negative bias (Figure 6.4). The current was measured at voltage steps of 1 mV. Silver was selected as the contact metal because of its ability to form ohmic contact with SWNT networks and its present application in Si-based photovoltaic grid systems [162].

Because p-doping of SWNT films via chemical treatment has been demonstrated as an effective method to improve the conductivity of SWNT electrodes [24, 97], the films in this study were chemically doped to ascertain the influence of this procedure on $\rho_c$. SWNT films were doped through a multi-treatment process consisting of immersion in $HNO_3$ followed by immersion in $SOCl_2$ to provide added conductivity enhancement as described by Jackson et al. [97] and in chapter 4 of this dissertation.

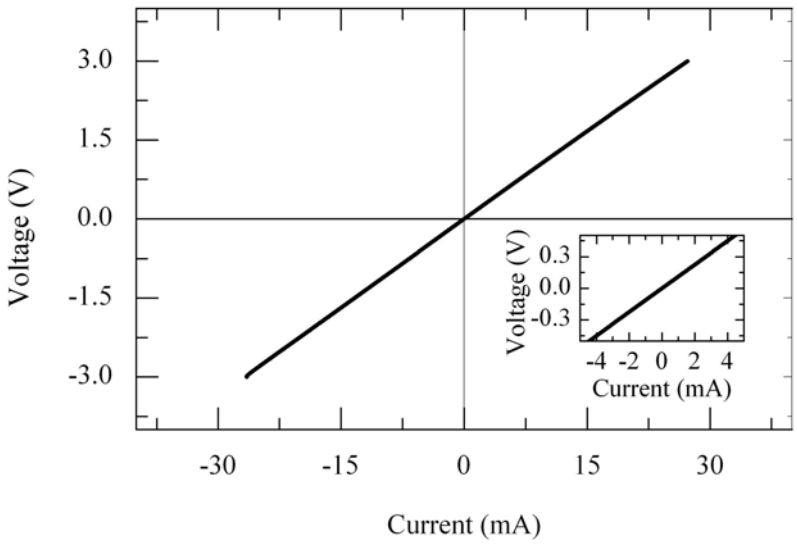


**Figure 6.4.** I-V curve between silver contact pads on SWNT film. Inset: Limited range I-V curve of silver contact pads on SWNT film to illustrate linearity near 0 V.

A total of 12 undoped SWNT films and 10 doped SWNT films were compared. The average sheet resistance of doped SWNT films was 200 Ω-sq$^{-1}$ (standard deviation, s = 35 Ω-sq$^{-1}$) compared to 338 Ω-sq$^{-1}$ (s = 32 Ω-sq$^{-1}$) for as-made films. Because $L_T$ and $\rho_c$ have small mean values, large variances, and cannot be negative, the resulting distribution is skewed. Thus, a Gaussian distribution cannot be assumed. In such cases of skewness, a log-normal distribution is often used [163]. The adequacy of this distribution was tested using the Shapiro-Wilk test for normality of the natural log of $L_T$ and $\rho_c$ (Table 6.1). For all cases, the p-value of the test was significantly large (> 0.05) such that the null hypothesis of log-normal distribution is not rejected. Therefore subsequent analysis of mean and variance is adequate.

**Table 6.1**. Results of Shapiro-Wilks test for normality of ln($L_T$) and ln($\rho_c$).

| | As-made SWNT film | | Doped SWNT film | |
|---|---|---|---|---|
| | degrees of freedom | p-value | degrees of freedom | p-value |
| ln($L_T$) | 12 | 0.77042 | 10 | 0.51876 |
| ln($\rho_c$) | 12 | 0.77436 | 10 | 0.29725 |

**Table 6.2.** Transfer lengths of as-made and doped SWNT films with silver contacts.

| | Mean | 68.3 % Confidence Interval | |
|---|---|---|---|
| | (cm) | Lower Bound | Upper Bound |
| Undoped SWNT Film | 0.008 | 0.004 | 0.013 |
| Doped SWNT Film | 0.021 | 0.015 | 0.032 |

**Table 6.3.** Specific contact resistance of as-made and doped SWNT films with silver contacts.

| | Mean (cm) | 68.3 % Confidence Interval | |
|---|---|---|---|
| | | Lower Bound | Upper Bound |
| Undoped SWNT Film | 0.02 | 0.007 | 0.062 |
| Doped SWNT Film | 0.091 | 0.042 | 0.199 |

The mean values of $L_T$ and $\rho_c$ of as-made and doped SWNT films with silver contacts are shown in Table 6.2 and 6.3. In both as-made and doped SWNT films, $L_T$ was experimentally found to be less than half of the contact pad length (0.1 cm), which justified the assumption of an electrically long contact in the application of eq. (6.5). $\rho_c$ for the as-made film was found to be 0.02 Ω-cm$^2$. As shown in Chapters 4 and 5, semiconducting SWNTs in as-made films are sufficiently doped from oxygen species to shift $E_F$ into the valence band, thereby causing semiconducting SWNTs to partially contribute to electrical conduction in the film along with metallic SWNTs. A schematic of the electronic structure of oxygen doped semiconducting SWNTs is shown in Figure 6.5a. Once silver was deposited onto the SWNT surface, electronic equilibrium must be reached such that $E_F$ was constant for the two materials in electrical contact, as illustrated in Figure 6.5b. As the Fermi levels equilibrate, electrons flow from the material with the lowest work function to the other. A Schottky barrier, $\varphi_b$, to electronic transport is formed at the metal/semiconductor interface at electronic equilibrium when there is an initial energy difference between the work function of the metal and the charge carrier band edge of the semiconductor,[164] as demonstrated in Figure 6.6. However, because, the work function of silver (ca. 4.7 eV[165]) lies below the carrier band edge in semiconducting SWNTs (S1 van Hove

singularity), no Schottky barrier is expected. Also, because oxygen doping is not sufficient to make semiconducting SWNTs as conductive as metallic SWNTs (Chapter 5), the electrical nature of the as-made SWNT film and metal contact interface is likely dominated by the interaction of the metal and metallic nanotubes where no charge transfer barrier is expected. The analysis presented in this discussion is consistent with the observed ohmic contact behavior over the full I-V curve in Figure 6.4. Consequently, the contact resistance at this interface is a factor of the lack of intimate contact over the contact pad area since electron beam deposition is not sufficient to provide conformal coating of the SWNT network, in addition to any local chemistry between the two surfaces. As discussed in Chapter 4, oxygen and water from the air, readily adsorb on SWNT surfaces, which would in turn, impact local surface chemistry between the contact metal and SWNT film.

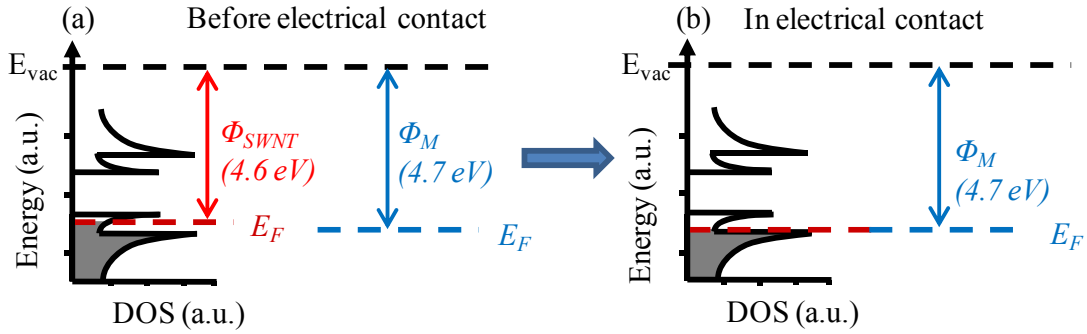


**Figure 6.5.** (a) Illustration of electronic band structure of semiconducting SWNTs in as-made SWNT film before electrical contact with silver pad. (b) Illustration of electronic band structure of semiconducting SWNTs in as-made SWNT film in electrical contact with silver pad.

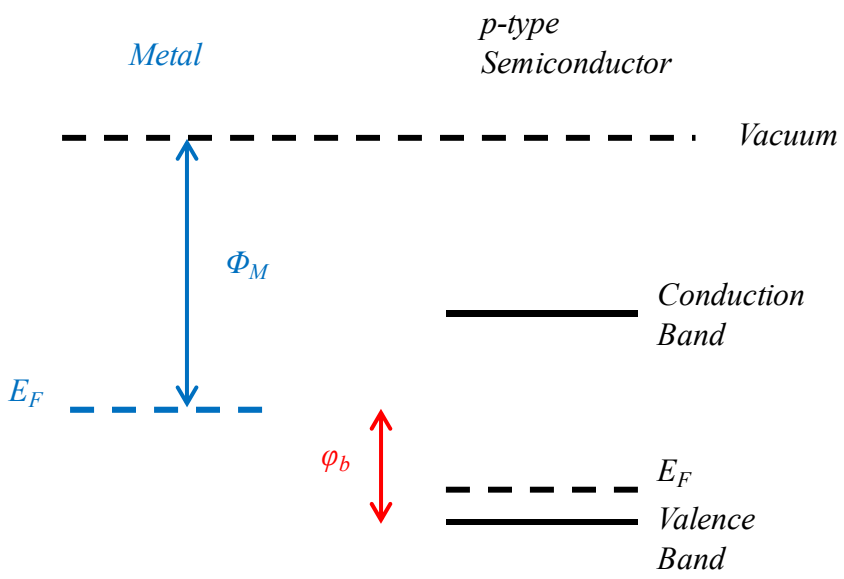


**Figure 6.6.** Energy band diagram of metal and p-type semiconductor before electrical contact.

As a result of doping through chemical treatment, higher conductive pathways were created in the SWNT film to effectively reduce the overall resistance to lateral current. Therefore, $L_T$ was larger for doped SWNT films as the resistance to current flow under the metal pad was decreased. While $R_{sh}$ was decreased due to doping, $\rho_c$ did not decrease as is typically observed in traditional metal/semiconducting contacts [161]. In these reports, increased doping results in lower $\rho_c$ due to the decrease in the effective barrier height at the metal/semiconductor interface. However, because the work function of silver lies within the valence band of semiconducting SWNTs, no Schottky barrier is expected. Thus, there is no barrier height to lower. As the metal and highly doped SWNTs are brought into electrical contact, electronic equilibrium at the SWNT/silver interface is similar to the as-made SWNT film as illustrated in Figure 6.7. Likewise, the contact resistance at this interface is then primarily a factor of the lack of

intimate contact over the silver pad area and any local chemistry between the two surfaces. However, the mean $\rho_c$ of the doped films of 0.091 Ω-cm$^2$ is higher and the distribution of $\rho_c$ is larger in doped films in comparison to as-made films (Table 6.3). This can likely be ascribed to the impact of residual ions from chemical treatment on the surface of the SWNT film that impact the local chemistry between the SWNT film and the silver.

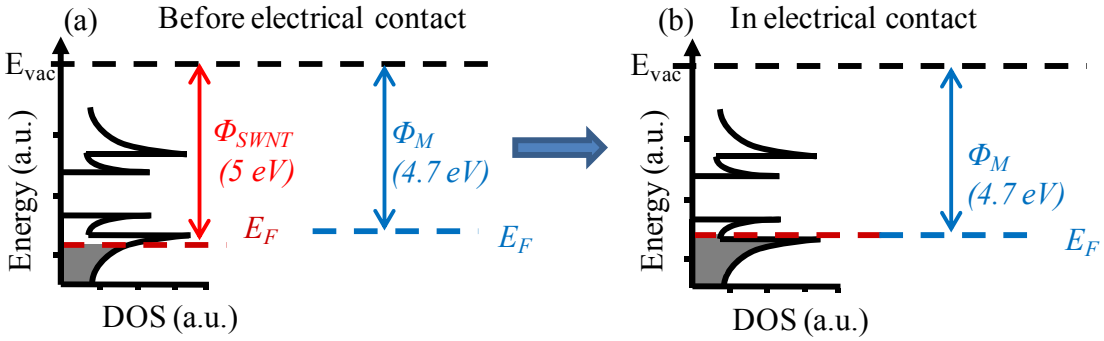


**Figure 6.7.** (a) Illustration of electronic band structure of semiconducting SWNTs in doped SWNT film before electrical contact with silver pad. (b) Illustration of electronic band structure of semiconducting SWNTs in doped SWNT film in electrical contact with silver pad. The equilibrium location of $E_F$ is similar to the as-made SWNT film in Figure 6.5.

## 6.4. Impact on Device Power Loss

When considering the impact of $\rho_c$ on photovoltaic ohmic losses, the power loss due to contact resistance ($P_{cont}$) can be normalized to the maximum output ($P_{out}$) of the cells. $P_{out}$ is estimated from current state of the art OPVs with device efficiencies of 5.1% [166]. At maximum power, the voltage ($V_{mp}$) and current density ($J_{mp}$) were

estimated to be 0.425 V and 12 mA/cm$^2$, respectively. The fractional losses due to contact resistance ($p_{loss}$) can be computed from

$$p_{loss} = \frac{P_{cont}}{P_{out}} = \frac{(JA)^2 R_c}{JAV} \tag{6.6}$$

where $A$ is the area between metallic fingers. With Eq. (6.2), $p_{loss}$ can be written as:

$$p_{loss} = \frac{Jd\rho_c}{VL_T} \tag{6.7}$$

where $d$ denotes the separation between metallic fingers. The finger separation was chosen to be 0.4 cm such that resistive power losses from the electrode sheet resistance can be limited as shown by Rowell et al [167]. The computed results for silver contacts on SWNT electrodes are shown in Table 6.4. For comparison, $L_T$, $\rho_c$, and $p_{loss}$ for silver lines deposited onto ITO and for screen printed silver contacts on the top emitter layer in silicon photovoltaics [162] are also shown in Table 6.4 under similar device operating conditions. The $L_T$ and $\rho_c$, for silver contacts on ITO was derived from the TLM in a similar manner as SWNT/silver contacts described in the previous section. The specific contact resistance was higher for an as-made SWNT film in contact with silver than for ITO and more than an order of magnitude higher than silicon based photovoltaics with a typical specific contact resistance of 1 mΩ-cm$^2$ and sheet resistance of 40 Ωsq$^{-1}$.

**Table 6.4.** $L_T$, $p_{loss}$, and $\rho_c$ for metal contacts on SWNT electrodes, ITO and the emitter layer in silicon based photovoltaics.

| | $\rho_c$ ($\Omega$-cm$^2$) | $L_T$ (cm) | $p_{loss}$ (%) |
|---|---|---|---|
| As-made SWNT/Silver | 0.020 | 0.008 | 2.82% |
| Doped SWNT/Silver | 0.091 | 0.021 | 4.89% |
| ITO/Silver | 0.008 | 0.011 | 0.82% |
| Si-PV/Silver | 0.001 | 0.005 | 0.23% |

## 6.5. Conclusion

The goal of this chapter was to describe the electrical nature of the interfacial contact resistance between the metal fingers and randomly distributed SWNT networks. To this end, the first ever data on such contact parameters were described. The specific contact resistance of a SWNT film in contact with a metallic silver pad was found to be significantly higher than typical values obtained in silicon-based photovoltaic applications, resulting in non negligible power losses. Higher $\rho_c$ can be attributed to the deviation from ideal planar contact of a SWNT mat in contact with silver surface, and any local chemistry between the SWNT surface and silver. However, while this work provides the first reported measurement of $\rho_c$ at this interface, no optimization has been performed, thereby providing an opportunity for reduced contact resistance with further research.

# CHAPTER 7: CONCLUSIONS AND FUTURE OUTLOOK

The research in this dissertation has been conducted to advance the goal of manufacturing SWNT networks with transparent electrode properties that meet or exceed those of ITO. To this end, SWNT films were characterized with regard to the collective and individual properties of the SWNTs that comprise the network. The insight gained from evaluation of intrinsic SWNT properties was effectively leveraged to expand the present understanding of SWNT networks to facilitate future SWNT electrode development.

Important findings of this dissertation are as follows:

- Chapter 4 expanded the understanding of how SWNT electrode optoelectronic properties are affected by moderate and heavy doping. Ultraviolet photoelectron spectroscopy was used to determine and present the first summarized report of the variation in work function of as-made, annealed, and chemically doped SWNT films. This chapter also presented the first known study to corroborate x-ray and ultraviolet photoelectron spectroscopy analysis, optical transmittance observations, and electrical sheet resistance measurements with an understanding of carbon nanotube electronic density of states to clearly elucidate the effect of unintentional and chemically induced doping on SWNT films. Conducting-tip AFM was used to reveal the highly electro-active nature of the SWNT film surface after chemical doping, particularly with respect to the surface of ITO. Sustained electrical conductivity of chemically doped SWNT films under

moderate thermal loading and air exposure was achieved via a thin conductive polymer "capping layer".

- Insight gained from Chapter 4 was used to suggest that comparisons of as-made SWNT films is enhanced and substantiated by accounting for incidental doping. To avoid comparisons of SWNT film electrical properties that are speculative and subject to spurious conclusions, inclusion of optical transmittance that extended into the near infrared (ca. 2500 nm) was shown to be a sufficient method to effectively infer a qualitative level of unintentional hole doping.
- Chapter 5 investigated the optoelectronic properties of SWNT films of homogeneous electronic type to clearly describe the impact of charge carrier doping on these networks. Counter to conventional intuition, chemically doped semiconducting SWNT films were found to have superior optoelectronic properties in comparison to similarly processed metallic SWNT films. It was concluded that a greater number of free charge carriers were induced in doped semiconducting SWNTs than in metallic SWNTs due to the distinct differences in the electronic density of states. Photoelectron spectroscopy, $R_{sh}$ evaluation, and UV-Vis-NIR transmittance spectra were presented and discussed to provide experimental corroboration of this conclusion. Ultraviolet photoelectron spectroscopy was also used to determine and present the first summarized report of the variation in work function of as-made, annealed, and chemically doped SWNT films of homogeneous electronic type.
- Chapter 6 provided the first report of the electrical nature of the interfacial contact between thin SWNT films and metallic contacts via quantification of the specific

contact resistance. The impact of specific contact resistance on OPV power loss was also estimated.

The research contribution of this dissertation can be leveraged with present state of the art in SWNT films to advance the goal of manufacturing SWNT networks with transparent electrode properties that meet or exceed those of ITO. However, issues remain that must be addressed before SWNT film electrodes can reach commercial market penetration. These primarily include further decreasing the sheet resistance to better compete with ITO on glass that has a sheet resistance of 10 $\Omega$-sq$^{-1}$ and successful and consistent integration of SWNT electrodes in organic electronic devices. These goals constitute future work and are discussed in the section to follow.

**Future Work: Integration of SWNT electrodes into OPV devices**

The research presented in this dissertation has demonstrated that SWNT films deposited on transparent substrates are increasingly becoming a viable alternative to ITO. Ultimately, these electrodes must be integrated into organic electronics with comparable or better performance than similar ITO devices. Preliminary data was obtained for small molecule based OPVs fabricated on SWNT electrodes. OPV devices were fabricated by spin coating a layer of PEDOT:PSS onto SWNT films fabricated and p-doped as described in Chapter 3 and 4. The PEDOT:PSS layer was used to serve as a "capping" layer to insulate the dopant molecules from the ambient environment and subsequent organic layers, in addition to providing a smoother surface for further deposition as was shown by other groups utilizing SWNTs as a positive electrode material in organic

devices.[91, 103] Bilayer devices comprised of Pentacene and $C_{60}$ small molecules were subsequently deposited via thermal evaporation as described in Yoo et al. [168] with the exception that silver was deposited as the cathode material. Figure 7.1a illustrates the described architecture for this device. Current density (J) – voltage (V) characteristics of a sample device is shown in Figure 5.1b with a similar bilayer device deposited on ITO electrodes for comparison. The OPV deposited onto a SWNT electrode (of heterogeneous electronic type) underperformed the standard ITO based OPV with SWNT devices achieving a power conversion efficiency of 1.1% compared to 3.9% for ITO devices.

A plausible explanation for this discrepancy can be attributed to the higher sheet resistance of SWNT films. As discussed in Chapter 1, the series resistance, $R_s$, is proportional to the sheet resistance of the transparent electrode. However, a more subtle cause for the lower performance can be related to the higher work function of doped SWNT films. Doped SWNTs can have a work function of approximately 5.0 - 5.3 eV compared to typical ITO electrodes with a work function of ca. 4.7 eV. The energy of the HOMO level of Pentacene is about 4.9 eV. As also discussed earlier, optimal hole collection in OPV devices is achieved when the work function of the positive electrode is close to the energy of the organic donor HOMO layer, which is accomplished in the ITO structure. Consequently the doped SWNT layer can introduce an energy barrier at the interface of the organic layer and thereby limit device performance.

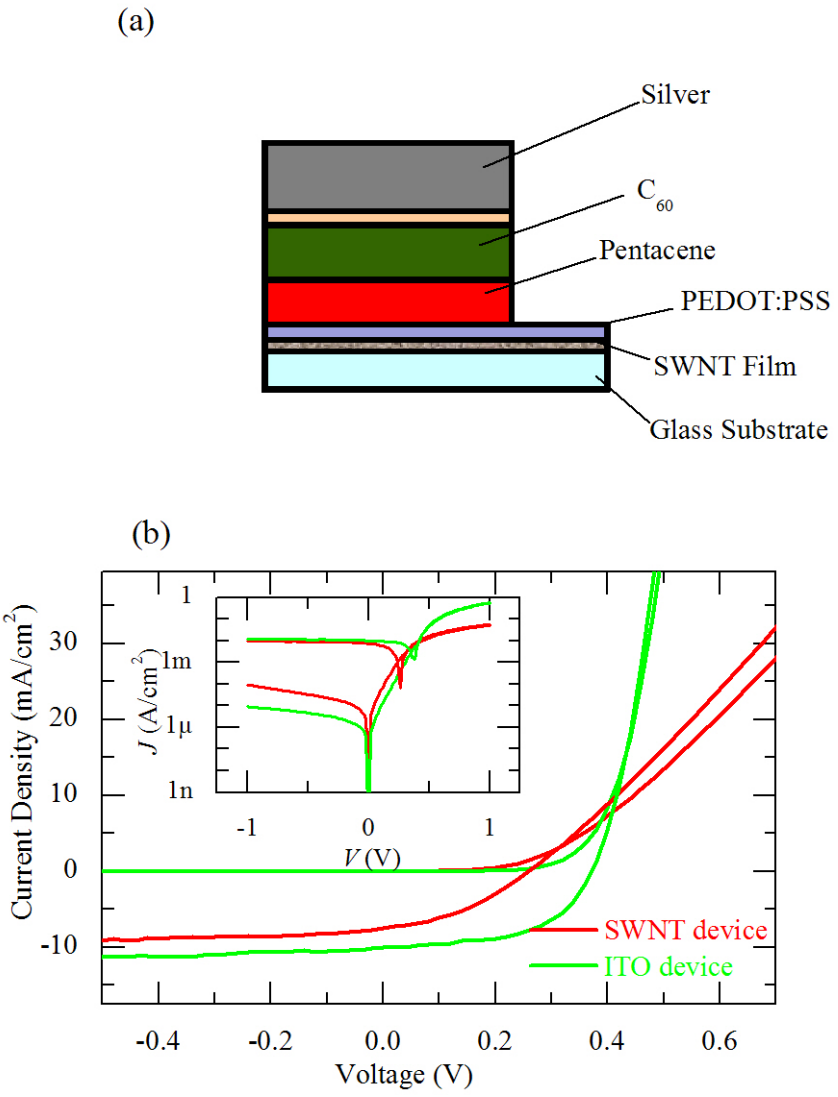


**Figure 7.1.** (a) Schematic device structure of OPV on SWNT film. (b) Current density (*J*) – voltage (*V*) characteristics of OPV devices constructed on SWNTs and on ITO for comparison. Inset: full-range curves in semi logarithmic scale under illumination and in dark.

Power conversion efficiencies of 2.5% have been reported by Rowell et al.[103] with polymer blend spin coated OPVs. Two noteworthy differences in device type and architecture can be observed in these reported devices and the devices obtained from preliminary tests. First, the HOMO level of the donor material in these devices is approximately 5.3 eV which would generate a reduced hole collection barrier at the SWNT/donor interface. Therefore, similar polymer blend spin coated OPVs should be fabricated on SWNT film and investigated for improved charge collection at the electrode/donor interface. Also, a grid system similar to the proposed architecture in Chapter 6 was incorporated in the devices to reduce the resistive impact of higher sheet resistance SWNT films. Devices containing similar grid systems should also be fabricated on SWNT electrodes to further assess the viability of SWNT electrodes as an alternative to ITO.

Lower $R_{sh}$ of SWNT films should be a priority in order to successfully displace ITO in organic electronics. As discussed in chapter 2 (2.4.3.2), SWNT length and bundle diameter affect $R_{sh}$. Optimization of solution dispersion should be sought to best achieve small bundle sizes with minimal mechanical damage and length shortening of the nanotubes. Also, it has been the observation of this author that nanotube films reported in the literature with SWNTs purchased from Iijin Nanotech Co. Ltd in South Korea have electrical properties that exceed those of similarly processed films. This could be attributed to the length composition of SWNTs in the batch supplied nanotube powder. A comprehensive study that compares SWNTs from different manufacturers in SWNT films utilizing methods outlined in this dissertation should be pursued to ascertain the difference in nanotube properties of different suppliers, if they exist.

The OPVs investigated in Figure 7.1 and others discussed in the literature have employed SWNT films of heterogeneous electronic type. A study should be conducted on OPVs on metallic and semiconducting homogeneous SWNT films to ascertain the impact of the different electronic structures on the charge collection in these devices. Also, due to the electronic homogeneity of the film, these devices have lower $R_{sh}$, which should in turn increase device performance.

However, the surface roughness of these films is most likely the largest barrier to successful integration into organic electronics. As demonstrated with AFM surface images in Chapter 3, SWNT film surfaces significantly rough and contain high peak to valley ratios. Since OPVs and OLEDs have small active layers on the order of 10 -100 nm in thickness, large spikes of SWNT ropes, metal catalysts, or carbonaceous impurities will significantly degrade device performance via electrical shorts to the negative electrode. Therefore, fabrication of SWNT electrodes should be evaluated to determine the best manner in which to produce smooth, conductive SWNT films. The ultrasonic spray technique developed by Tenent et al. [101] represents a key development to this end.

In conclusion, the results of this dissertation provide further optimism for the potential of SWNT transparent electrodes as a surrogate for ITO in organic electronics. The insight provided can be effectively leveraged in future SWNT electrode development to yield electrical sheet resistance values that compare well with the present values of 10 – 70 $\Omega$-sq$^{-1}$ for ITO. However, as suggested by the superior nanoscale surface electroactivity of SWNT electrodes in comparison to ITO, SWNT electrodes may be able to outperform ITO in device operation, even with higher electrical sheet resistances.

Also, due to the 1-D nature of SWNTs, an unconventional approach will likely be required to maximize their utility in electronic devices. In contradistinction to traditional methods, degenerately doped semiconducting SWNTs may provide the optimal path to all metallic networks that result in high conducting transparent electrodes. On the other hand, because $R_{sh}$ in metallic SWNTs is less sensitive to the Fermi level position, low work function networks of metallic nanotubes may also find utility as the negative electrode in organic electronics. Overall, the unique optoelectronic properties of single wall carbon nanotubes, in combination with the mechanical stability exhibited in thin nanotube networks, make SWNT transparent electrodes a promising candidate for organic photovoltaic and organic LED integration.

# REFERENCES


[1] C. W. Tang and S. A. Vanslyke, "ORGANIC ELECTROLUMINESCENT DIODES," *Applied Physics Letters,* vol. 51, pp. 913-915, Sep 1987.

[2] R. H. Friend, R. W. Gymer, A. B. Holmes, J. H. Burroughes, R. N. Marks, C. Taliani, D. D. C. Bradley, D. A. Dos Santos, J. L. Bredas, M. Logdlund, and W. R. Salaneck, "Electroluminescence in conjugated polymers," *Nature,* vol. 397, pp. 121-128, Jan 1999.

[3] Y.-L. Loo and I. McCulloch, "Progress and Challengers in Commercialization of Organic Electronics," *MRS Bulletin,* vol. 33, pp. 653-658, 2008.

[4] J. Walko, "UDC's white OLEDs break the 100 lm/W barrier," in *EE Times* London, 2008.

[5] B. Kippelen, "Organic Photovoltaics," in *Optics and Photonics News*, 2007.

[6] C. J. Brabec and J. R. Durrant, "Solution-Processed Organic Solar Cells," *MRS Bulletin,* vol. 33, pp. 670-671, 2008.

[7] L. Chkoda, C. Heske, M. Sokolowski, E. Umbach, F. Steuber, J. Staudigel, M. Stossel, and J. Simmerer, "Work function of ITO substrates and band-offsets at the TPD/ITO interface determined by photoelectron spectroscopy," *Synthetic Metals,* vol. 111, pp. 315-319, 2000.

[8] K.-B. Kim, Y.-H. Tak, Y.-S. Han, K.-H. Baik, M.-H. Yoon, and M.-H. Lee, "Relationship between surface roughness of indium tin oxide and leakage current of organic light-emitting diode," *Japanese Journal of Applied Physics, Part 2: Letters,* vol. 42, pp. 438-440, 2003.

[9] J. C. C. Fan, F. J. Bachner, and G. H. Foley, "Effect of O2 pressure during deposition on properties of RF-sputtered Sn-doped InO3 films," *Applied Physics Letters,* vol. 31, pp. 773-5, 1976.

[10] J. Olivier, B. Servet, M. Vergnolle, M. Mosca, and G. Garry, "Stability/instability of conductivity and work function changes of ITO thin films, UV-irradiated in air or vacuum: Measurements by the four-probe method and by Kelvin force microscopy," *Synthetic Metals,* vol. 122, pp. 87-89, 2001.

[11] J. S. Kim, B. Lägel, E. Moons, N. Johansson, I. D. Baikie, W. R. Salaneck, R. H. Friend, and F. Cacialli, "Kelvin probe and ultraviolet photoemission measurements of indium tin oxide work function: a comparison," *Synthetic Metals,* vol. 111-112, pp. 311-314, 2000.

[12] M. T. Bhatti, A. M. Rana, and A. F. Khan, "Characterization of rf-sputtered indium tin oxide thin films," *Materials Chemistry and Physics,* vol. 84, pp. 126-130, Mar 2004.

[13] Y. Zhou, L. Hu, and G. Gruner, "A method of printing carbon nanotube thin films," *Applied Physics Letters,* vol. 88, p. 123109, 2006.

[14] A. Chipman, "A commodity no more," *Nature,* vol. 449, pp. 131-131, Sep 2007.

[15] Y. Leterrier, L. Medico, F. Demarco, J. A. E. Manson, U. Betz, M. F. Escola, M. K. Olsson, and F. Atamny, "Mechanical integrity of transparent conductive oxide films for flexible polymer-based displays," *Thin Solid Films,* vol. 460, p. 156, 2004.

[16] M. Brumbach, P. A. Veneman, F. S. Matrikar, T. Schulmeyer, A. Simmonds, W. Xia, P. Lee, and N. R. Armstrong, "Surface composition and electrical and electrochemical properties of freshly deposited and acid-etched indium tin oxide electrodes," *Langmuir,* vol. 23, pp. 11089-11099, 2007.

[17] M.-H. Jung and H.-S. Choi, "Surface treatment of indium tin oxide using radio frequency atmospheric and low pressure plasma for OLEDs," *Journal of the Electrochemical Society,* vol. 155, pp. 334-340, 2008.

[18] G. Carter, M. J. Nobes, and D. G. Armour, "The erosion energy efficiency of sputtering," *Vacuum,* vol. 32, pp. 509-512, 1982.

[19] E. Fortunato, D. Ginley, H. Hosono, and D. C. Paine, "Transparent conducting oxides for photovoltaics," *MRS Bulletin,* vol. 32, p. 242, 2007.

[20] T. Aernouts, P. Vanlaeke, W. Geens, J. Poortmans, P. Heremans, S. Borghs, R. Mertens, R. Andriessen, and L. Leenders, "Printable anodes for flexible organic solar cell modules," *Thin Solid Films,* vol. 451-452, pp. 22-25, 2004.

[21] J. Huang, X. Wang, A. J. DeMello, J. C. DeMello, and D. D. C. Bradley, "Efficient flexible polymer light emitting diodes with conducting polymer anodes," *Journal of Materials Chemistry,* vol. 17, pp. 3551-3554, 2007.

[22] E. Kymakis, G. Klapsis, E. Koudoumas, E. Stratakis, N. Kornilios, N. Vidakis, and Y. Franghiadakis, "Carbon nanotube/PEDOT:PSS electrodes for organic photovoltaics," *EPJ Applied Physics,* vol. 36, pp. 257-259, 2006.

[23] J. B. Yoo, J. S. Moon, J. H. Park, T. Y. Lee, Y. W. Kim, C. Y. Park, J. M. Kim, and K. W. Jin, "Transparent conductive film based on carbon nanotubes and PEDOT composites," *Diamond and Related Materials,* vol. 14, pp. 1882-7, 2005.

[24] B. B. Parekh, G. Fanchini, G. Eda, and M. Chhowalla, "Improved conductivity of transparent single-wall carbon nanotube thin films via stable postdeposition functionalization," *Applied Physics Letters,* vol. 90, p. 121913, 2007.

[25] G. Gruner, "Carbon nanotube films for transparent and plastic electronics," *Journal of Materials Chemistry,* vol. 16, pp. 3533-3539, 2006.

[26] A. D. Pasquier, H. E. Unalan, A. Kanwal, S. Miller, and M. Chhowalla, "Conducting and transparent single-wall carbon nanotube electrodes for polymer-fullerene solar cells," *Applied Physics Letters,* vol. 87, p. 203511, 2005.

[27] Z. Wu, Z. Chen, X. Du, J. M. Logan, J. Sippel, M. Nikolou, K. Kamaras, J. R. Reynolds, D. B. Tanner, A. F. Hebard, and A. G. Rinzler, "Transparent, conductive carbon nanotube films," *Science,* vol. 305, pp. 1273-6, 2004.

[28] H. Jin Woo, K. Young Min, P. Young Wook, C. Jin Hwan, L. Jin Woo, L. Jong Woo, Y. Jae Woong, J. Sung Hoo, P. Kyeong Kap, and J. Byeong Kwon, "Characteristics of organic light-emitting diodes with conducting polymer anodes on plastic substrates," *Journal of Applied Physics,* vol. 103, pp. 044502-1, 2008.

[29] Y. Zhen, C. L. Kane, and C. Dekker, "High-field electrical transport in single-wall carbon nanotubes," *Physical Review Letters,* vol. 84, pp. 2941-4, 2000.

[30] E. Bekyarova, M. E. Itkis, N. Cabrera, B. Zhao, A. P. Yu, J. B. Gao, and R. C. Haddon, "Electronic properties of single-walled carbon nanotube networks," *Journal of the American Chemical Society,* vol. 127, pp. 5990-5995, Apr 2005.

[31] N. Saran, K. Parikh, D. S. Suh, E. Munoz, H. Kolla, and S. K. Manohar, "Fabrication and characterization of thin films of single-walled carbon nanotube bundles on flexible plastic substrates," *Journal of the American Chemical Society,* vol. 126, pp. 4462-4463, Apr 2004.

[32] M. E. Itkis, S. Niyogi, M. E. Meng, M. A. Hamon, H. Hu, and R. C. Haddon, "Spectroscopic study of the Fermi level electronic structure of single-walled carbon nanotubes," *Nano Letters,* vol. 2, pp. 155-9, 2002.

[33] S. Iijima, "HELICAL MICROTUBULES OF GRAPHITIC CARBON," *Nature,* vol. 354, pp. 56-58, Nov 1991.

[34] B. C. Edwards, "A hoist to the heavens," *IEEE Spectrum,* vol. 42, pp. 30-35, 2005.

[35] J. Chen, J. Z. Wang, A. I. Minett, Y. Liu, C. Lynam, H. Liu, and G. G. Wallace, "Carbon nanotube network modified carbon fibre paper for Li-ion batteries," *Energy and Environmental Sciences,* vol. 2, pp. 393-396, 2009.

[36] G. Rao, "Carbon nanotubes used for cancer cell destruction and drug delivery," *MRS Bulletin,* vol. 30, pp. 805-805, 2005.

[37] J. Kong, N. R. Franklin, C. W. Zhou, M. G. Chapline, S. Peng, K. J. Cho, and H. J. Dai, "Nanotube molecular wires as chemical sensors," *Science,* vol. 287, pp. 622-625, Jan 2000.

[38] M. S. Dresselhaus, G. Dresselhaus, and R. Saito, "PHYSICS OF CARBON NANOTUBES," *Carbon,* vol. 33, pp. 883-891, 1995.

[39] R. Saito, M. Fujita, G. Dresselhaus, and M. S. Dresselhaus, "ELECTRONIC-STRUCTURE OF CHIRAL GRAPHENE TUBULES," *Applied Physics Letters,* vol. 60, pp. 2204-2206, May 1992.

[40] J. C. Charlier, X. Blase, and S. Roche, "Electronic and transport properties of nanotubes," *Reviews of Modern Physics,* vol. 79, pp. 677-732, Apr-Jun 2007.

[41] M. S. Dresselhaus and P. C. Eklund, "Phonons in carbon nanotubes," *Advances in Physics,* vol. 49, pp. 705-814, 2000.

[42] V. N. Popov, "Carbon nanotubes: properties and application," *Materials Science & Engineering R-Reports,* vol. 43, pp. 61-102, Jan 2004.

[43] P. J. F. Harris, *Carbon Nanotubes and Related Structures*. Cambridge, United Kingdom: Cambridge University Pres, 1999.

[44] P. R. Wallace, "The band theory of graphite," *Physical Review,* vol. 71, pp. 622-634, 1947.

[45] G. S. Painter and D. E. Ellis, "ELECTRONIC BAND STRUCTURE AND OPTICAL PROPERTIES OF GRAPHITE FROM A VARIATIONAL APPROACH," *Physical Review B,* vol. 1, pp. 4747-&, 1970.

[46] R. Saito, G. Dresselhaus, and M. S. Dresselhaus, "Trigonal warping effect of carbon nanotubes," *Physical Review B,* vol. 61, p. 2981, 2000.

[47] *Understanding carbon nanotubes : from basics to applications*. Berlin ;: Springer, 2006.

[48] S. Maruyama, " "Shigeo Maruyama's Fullerene and Carbon Nanotube Site"."

[49] H. Kataura, Y. Kumazawa, Y. Maniwa, I. Umezu, S. Suzuki, Y. Ohtsuka, and Y. Achiba, "Optical properties of single-wall carbon nanotubes," *Synthetic Metals,* vol. 103, pp. 2555-2558, 1999.

[50] J. C. Charlier and P. Lambin, "Electronic structure of carbon nanotubes with chiral symmetry," *Physical Review B,* vol. 57, pp. R15037-R15039, Jun 1998.

[51] L. Yang and J. Han, "Electronic structure of deformed carbon nanotubes," *Physical Review Letters,* vol. 85, pp. 154-157, Jul 2000.

[52] C. L. Kane and E. J. Mele, "Size, shape, and low energy electronic structure of carbon nanotubes," *Physical Review Letters,* vol. 78, pp. 1932-1935, Mar 1997.

[53] C. E. Baddour and C. Briens, "Carbon Nanotube Synthesis: A Review," *International Journal of Chemical Reactor Engineering,* vol. 3, 2005.

[54] C. Journet, W. K. Maser, P. Bernier, A. Loiseau, M. L. delaChapelle, S. Lefrant, P. Deniard, R. Lee, and J. E. Fischer, "Large-scale production of single-walled carbon nanotubes by the electric-arc technique," *Nature,* vol. 388, pp. 756-758, Aug 1997.

[55] T. Guo, P. Nikolaev, A. Thess, D. T. Colbert, and R. E. Smalley, "CATALYTIC GROWTH OF SINGLE-WALLED NANOTUBES BY LASER VAPORIZATION," *Chemical Physics Letters,* vol. 243, pp. 49-54, Sep 1995.

[56] P. N. Vinod, "Application of power loss calculation to estimate the specific contact resistance of the screen-printed silver ohmic contacts of the large area silicon solar cells," *Journal of Materials Science: Materials in Electronics,* vol. 18, pp. 805-810, 2007.

[57] M. Jose-Yacaman, M. Miki-Yoshida, L. Rendon, and J. G. Santiesteban, "Catalytic growth of carbon microtubules with fullerene structure," *Applied Physics Letters,* vol. 62, pp. 202-204, 1993.

[58] H. J. Dai, "Carbon nanotubes: Synthesis, integration, and properties," *Accounts of Chemical Research,* vol. 35, pp. 1035-1044, Dec 2002.

[59] G. Che, B. B. Lakshmi, C. R. Martin, E. R. Fisher, and R. S. Ruoff, "Chemical vapor deposition based synthesis of carbon nanotubes and nanofibers using a template method," *Chemistry of Materials,* vol. 10, pp. 260-267, Jan 1998.

[60] J. Kong, H. T. Soh, A. M. Cassell, C. F. Quate, and H. J. Dai, "Synthesis of individual single-walled carbon nanotubes on patterned silicon wafers," *Nature,* vol. 395, pp. 878-881, Oct 1998.

[61] J. H. Hafner, M. J. Bronikowski, B. R. Azamian, P. Nikolaev, A. G. Rinzler, D. T. Colbert, K. A. Smith, and R. E. Smalley, "Catalytic growth of single-wall carbon nanotubes from metal particles," *Chemical Physics Letters,* vol. 296, pp. 195-202, 1998.

[62] L. X. Zheng, M. J. O'Connell, S. K. Doorn, X. Z. Liao, Y. H. Zhao, E. A. Akhadov, M. A. Hoffbauer, B. J. Roop, Q. X. Jia, R. C. Dye, D. E. Peterson, S. M. Huang, J. Liu, and Y. T. Zhu, "Ultralong single-wall carbon nanotubes," *Nature Materials,* vol. 3, pp. 673-676, Oct 2004.

[63] L. Hu, D. S. Hecht, and G. Gruner, "Percolation in transparent and conducting carbon nanotube networks," *Nano Letters,* vol. 4, pp. 2513-2517, 2004.

[64] Q. Cao, S.-H. Hur, Z.-T. Zhu, Y. Sun, C. Wang, M. A. Meitl, M. Shim, and J. A. Rogers, "Highly bendable, transparent thin-film transistors that use carbon-nanotube-based conductors and semiconductors with elastomeric dielectrics," *Advanced Materials,* vol. 18, p. 304, 2006.

[65] M. H. A. Ng, L. T. Hartadi, T. Huiwen, and C. H. P. Poa, "Efficient coating of transparent and conductive carbon nanotube thin films on plastic substrates," *Nanotechnology,* vol. 19, p. 205703 (5 pp.), 2008.

[66] S. Kim, S. Ju, J. H. Back, Y. Xuan, P. D. Ye, M. Shim, D. B. Janes, and S. Mohammad, "Fully transparent thin-film transistors based on aligned carbon nanotube arrays and indium tin oxide electrodes," *Advanced Materials,* vol. 21, pp. 564-568, 2009.

[67] Q. Cao, S. H. Hur, Z. T. Zhu, Y. Sun, C. J. Wang, M. A. Meitl, M. Shim, and J. A. Rogers, "Highly bendable, transparent thin-film transistors that use carbon-nanotube-based conductors and semiconductors with elastomeric dielectrics," *Advanced Materials,* vol. 18, pp. 304-+, Feb 2006.

[68] Q. Cao, Z.-T. Zhu, M. G. Lemaitre, M.-G. Xia, M. Shim, and J. A. Rogers, "Transparent flexible organic thin-film transistors that use printed single-walled carbon nanotube electrodes," *Applied Physics Letters,* vol. 88, pp. 113511-3, 2006.

[69] Q. Cao and J. A. Rogers, "Ultrathin Films of Single-Walled Carbon Nanotubes for Electronics and Sensors: A Review of Fundamental and Applied Aspects," *Advanced Materials,* vol. 21, pp. 29-53, Jan 2009.

[70] M. E. Itkis, D. E. Perea, S. Niyogi, S. M. Rickard, M. A. Hamon, B. Zhao, and R. C. Haddon, "Purity evaluation of as-prepared single-walled carbon nanotube soot by use of solution-phase near-IR spectroscopy," *Nano Letters,* vol. 3, pp. 309-314, Mar 2003.

[71] H. J. Huang, H. Kajiura, A. Yamada, and M. Ata, "Purification and alignment of arc-synthesis single-walled carbon nanotube bundles," *Chemical Physics Letters,* vol. 356, pp. 567-572, Apr 2002.

[72] H. Hu, B. Zhao, M. E. Itkis, and R. C. Haddon, "Nitric Acid Purification of Single-Walled Carbon Nanotubes," *Journal of Physical Chemistry B,* vol. 107, pp. 13838-13842, 2003.

[73] G. W. Lee and S. Kumar, "Dispersion of nitric acid-treated SWNTs in organic solvents and solvent mixtures," *Journal of Physical Chemistry B,* vol. 109, pp. 17128-17133, Sep 2005.

[74] L. Vaisman, H. D. Wagner, and G. Marom, "The role of surfactants in dispersion of carbon nanotubes," *Advances in Colloid and Interface Science,* vol. 128, pp. 37-46, Dec 2006.

[75] K. L. Lu, R. M. Lago, Y. K. Chen, M. L. H. Green, P. J. F. Harris, and S. C. Tsang, "Mechanical damage of carbon nanotubes by ultrasound," *Carbon,* vol. 34, pp. 814-816, 1996.

[76] K. Yurekli, C. A. Mitchell, and R. Krishnamoorti, "Small-Angle Neutron Scattering from Surfactant-Assisted Aqueous Dispersions of Carbon Nanotubes," *Journal of the American Chemical Society,* vol. 126, pp. 9902-9903, 2004.

[77] Z. C. Wu, Z. H. Chen, X. Du, J. M. Logan, J. Sippel, M. Nikolou, K. Kamaras, J. R. Reynolds, D. B. Tanner, A. F. Hebard, and A. G. Rinzler, "Transparent, conductive carbon nanotube films," *Science,* vol. 305, pp. 1273-1276, Aug 2004.

[78] V. C. Moore, M. S. Strano, E. H. Haroz, R. H. Hauge, R. E. Smalley, J. Schmidt, and Y. Talmon, "Individually Suspended Single-Walled Carbon Nanotubes in Various Surfactants," *Nano Letters,* vol. 3, pp. 1379-1382, 2003.

[79] H. Wang, W. Zhou, D. L. Ho, K. I. Winey, J. E. Fischer, C. J. Glinka, and E. K. Hobbie, "Dispersing single-walled carbon nanotubes with surfactants: A small angle neutron scattering study," *Nano Letters,* vol. 4, pp. 1789-1793, Sep 2004.

[80] D. Zhang, K. Ryu, X. Liu, E. Polikarpov, J. Ly, M. E. Tompson, and C. Zhou, "Transparent, conductive, and flexible carbon nanotube films and their application in organic light-emitting diodes," *Nano Letters,* vol. 6, pp. 1880-1886, 2006.

[81] M. F. Islam, E. Rojas, D. M. Bergey, A. T. Johnson, and A. G. Yodh, "High weight fraction surfactant solubilization of single-wall carbon nanotubes in water," *Nano Letters,* vol. 3, pp. 269-273, Feb 2003.

[82] H. Hu, A. Yu, E. Kim, B. Zhao, M. E. Itkis, E. Bekyarova, and R. C. Haddon, "Influence of the Zeta Potential on the Dispersability and Purification of Single-Walled Carbon Nanotubes," *The Journal of Physical Chemistry B,* vol. 109, pp. 11520-11524, 2005.

[83] M. N. Tchoul, W. T. Ford, G. Lolli, D. E. Resasco, and S. Arepalli, "Effect of Mild Nitric Acid Oxidation on Dispersability, Size, and Structure of Single-Walled Carbon Nanotubes," *Chemistry of Materials,* vol. 19, pp. 5765-5772, 2007.

[84] M. Burghard, "Electronic and vibrational properties of chemically modified single-wall carbon nanotubes," *Surface Science Reports,* vol. 58, pp. 1-109, Aug 2005.

[85] B. Kim, H. Park, and W. M. Sigmund, "Electrostatic interactions between shortened multiwall carbon nanotubes and polyelectrolytes," *Langmuir,* vol. 19, pp. 2525-2527, Mar 2003

[86] A. Kuznetsova, I. Popova, J. T. Yates, M. J. Bronikowski, C. B. Huffman, J. Liu, R. E. Smalley, H. H. Hwu, and J. G. Chen, "Oxygen-Containing Functional Groups on Single-Wall Carbon Nanotubes:  NEXAFS and Vibrational Spectroscopic Studies," *Journal of the American Chemical Society,* vol. 123, pp. 10699-10704, 2001.

[87] Y. Q. Tan and D. E. Resasco, "Dispersion of single-walled carbon nanotubes of narrow diameter distribution," *Journal of Physical Chemistry B,* vol. 109, pp. 14454-14460, Aug 2005.

[88] M. Kaempgen, G. S. Duesberg, and S. Roth, "Transparent carbon nanotube coatings," *Applied Surface Science,* vol. 252, pp. 425-429, Oct 2005.

[89] M. D. Lima, M. J. de Andrade, C. P. Bergmann, and S. Roth, "Thin, conductive, carbon nanotube networks over transparent substrates by electrophoretic deposition," *Journal of Materials Chemistry,* vol. 18, pp. 776-779, 2008.

[90] M. A. Meitl, Y. X. Zhou, A. Gaur, S. Jeon, M. L. Usrey, M. S. Strano, and J. A. Rogers, "Solution casting and transfer printing single-walled carbon nanotube films," *Nano Letters,* vol. 4, pp. 1643-1647, Sep 2004.

[91] E. Kymakis, E. Stratakis, and E. Koudoumas, "Integration of carbon nanotubes as hole transport electrode in polymer/fullerene bulk heterojunction solar cells," *Thin Solid Films,* vol. 515, pp. 8598-8600, Oct 2007.

[92] H.-W. Zhang and W.-y. Xu, "Effect of bias and post-deposition vacuum annealing on structure and transmittance of ITO films," *Vacuum,* vol. 43, pp. 835-836, 1992.

[93] B. G. Lewis and D. C. Paine, "Applications and processing of transparent conducting oxides," *MRS Bulletin,* vol. 25, pp. 22-27, 2000.

[94] M. J. de Andrade, M. D. Lima, V. Skakalova, C. P. Bergmann, and S. Roth, "Electrical properties of transparent carbon nanotube networks prepared through different techniques," *Physica Status Solidi-Rapid Research Letters,* vol. 1, pp. 178-180, Oct 2007.

[95] J. Li, L. Hu, L. Wang, Y. Zhou, G. Gruner, and T. J. Marks, "Organic light-emitting diodes having carbon nanotube anodes," *Nano Letters,* vol. 6, pp. 2472-2477, 2006.

[96] C. M. Aguirre, S. Auvray, S. Pigeon, R. Izquierdo, P. Desjardins, and R. Martel, "Carbon nanotube sheets as electrodes in organic light-emitting diodes," *Applied Physics Letters,* vol. 88, pp. 183104-1, 2006.

[97] R. Jackson, B. Domercq, R. Jain, B. Kippelen, and S. Graham, "Stability of Doped Transparent Carbon Nanotube Electrodes," *Advanced Functional Materials,* vol. 18, pp. 2548-2554, 2008.

[98] Z. R. Li, H. R. Kandel, E. Dervishi, V. Saini, Y. Xu, A. R. Biris, D. Lupu, G. J. Salamo, and A. S. Biris, "Comparative study on different carbon nanotube materials in terms of transparent conductive coatings," *Langmuir,* vol. 24, pp. 2655-2662, Mar 2008.

[99] B. Kippelen and J. L. Bredas, "Organic photovoltaics," *Energy & Environmental Science,* vol. 2, pp. 251-261, 2009.

[100] H.-Z. Geng, K. K. Kim, and Y. H. Lee, "Recent progresses in carbon nanotube-based flexible transparent conducting film," San Diego, CA, United states, 2008, p. The International Society for Optical Engineering (SPIE).

[101] R. C. Tenent, T. M. Barnes, J. D. Bergeson, A. J. Ferguson, B. To, L. M. Gedvilas, M. J. Heben, and J. L. Blackburn, "Ultrasmooth, Large-Area, High-Uniformity, Conductive Transparent Single-Walled-Carbon-Nanotube Films for Photovoltaics Produced by Ultrasonic Spraying," *Advanced Materials,* vol. 9999, p. NA, 2009.

[102] J. H. Yim, Y. S. Kim, K. H. Koh, and S. Lee, "Fabrication of transparent single wall carbon nanotube films with low sheet resistance," *Journal of Vacuum Science and Technology B: Microelectronics and Nanometer Structures,* vol. 26, pp. 851-855, 2008.

[103] M. W. Rowell, M. A. Topinka, M. D. McGehee, H. J. Prall, G. Dennler, N. S. Sariciftci, H. Liangbing, and G. Gruner, "Organic solar cells with carbon nanotube network electrodes," *Applied Physics Letters,* vol. 88, pp. 233506-1, 2006.

[104] M. Chhowalla, "Transparent and conducting SWNT thin films for flexible electronics," *Journal of the Society for Information Display,* vol. 15, pp. 1085-1088, Dec 2007.

[105] D. Hecht, H. Liangbing, and G. Gruner, "Conductivity scaling with bundle length and diameter in single walled carbon nanotube networks," *Applied Physics Letters,* vol. 89, pp. 133112-1, 2006.

[106] M. S. Fuhrer, J. Nygard, L. Shih, M. Forero, Y. G. Yoon, M. S. C. Mazzoni, H. J. Choi, J. Ihm, S. G. Louie, A. Zettl, and P. L. McEuen, "Crossed nanotube junctions," *Science,* vol. 288, pp. 494-497, Apr 2000.

[107] D. H. Shin, H. C. Shim, J.-W. Song, S. Kim, and C.-S. Han, "Conductivity of films made from single-walled carbon nanotubes in terms of bundle diameter," *Scripta Materialia,* vol. 60, pp. 607-610, 2009.

[108] U. Dettlaff-Weglikowska, V. Skakalova, R. Graupner, S. H. Jhang, B. H. Kim, H. J. Lee, L. Ley, Y. W. Park, S. Berber, D. Tomanek, and S. Roth, "Effect of $SOCl_2$ treatment on electrical and mechanical properties of single-wall carbon nanotube networks," *Journal of the American Chemical Society,* vol. 127, pp. 5125-5131, 2005.

[109] H. Z. Geng, K. K. Kim, K. P. So, Y. S. Lee, Y. Chang, and Y. H. Lee, "Effect of acid treatment on carbon nanotube-based flexible transparent conducting films," *Journal of the American Chemical Society,* vol. 129, pp. 7758-+, Jun 2007.

[110] B. Dan, G. C. Irvin, and M. Pasquali, "Continuous and Scalable Fabrication of Transparent Conducting Carbon Nanotube Films," *ACS Nano,* vol. 3, pp. 835-843, 2009.

[111] C. Bower, A. Kleinhammes, Y. Wu, and O. Zhou, "Intercalation and partial exfoliation of single-walled carbon nanotubes by nitric acid," *Chemical Physics Letters,* vol. 288, p. 481, 1998.

[112] W. Zhou, J. Vavro, N. M. Nemes, J. E. Fischer, F. Borondics, K. Kamaras, and D. B. Tanner, "Charge transfer and Fermi level shift in p-doped single-walled carbon nanotubes," *Physical Review B (Condensed Matter and Materials Physics),* vol. 71, pp. 205423-1, 2005.

[113] F. Hennrich, R. Wellmann, S. Malik, S. Lebedkin, and M. M. Kappes, "Reversible modification of the absorption properties of single-walled carbon nanotube thin films via nitric acid exposure," *Physical Chemistry Chemical Physics,* vol. 5, pp. 178-83, 2003.

[114] M. C. Hersam, "Progress towards monodisperse single-walled carbon nanotubes," *Nature Nanotechnology,* vol. 3, pp. 387-394, Jul 2008.

[115] S. R. Lustig, A. Jagota, C. Khripin, and M. Zheng, "Theory of structure-based carbon nanotube separations by ion-exchange chromatography of DNA/CNT hybrids," *Journal of Physical Chemistry B,* vol. 109, pp. 2559-2566, Feb 2005.

[116] R. Krupke, F. Hennrich, H. von Lohneysen, and M. M. Kappes, "Separation of metallic from semiconducting single-walled carbon nanotubes," *Science,* vol. 301, pp. 344-347, Jul 2003.

[117] P. C. Collins, M. S. Arnold, and P. Avouris, "Engineering carbon nanotubes and nanotube circuits using electrical breakdown," *Science,* vol. 292, pp. 706-709, Apr 2001.

[118] T. J. McDonald, J. L. Blackburn, W. K. Metzger, G. Rumbles, and M. J. Heben, "Chiral-selective protection of single-walled carbon nanotube photoluminescence by surfactant selection," *Journal of Physical Chemistry C,* vol. 111, pp. 17894-17900, Dec 2007.

[119] H. P. Li, B. Zhou, Y. Lin, L. R. Gu, W. Wang, K. A. S. Fernando, S. Kumar, L. F. Allard, and Y. P. Sun, "Selective interactions of porphyrins with semiconducting single-walled carbon nanotubes," *Journal of the American Chemical Society,* vol. 126, pp. 1014-1015, Feb 2004.

[120] A. A. Green and M. C. Hersam, "Colored semitransparent conductive coatings consisting of monodisperse metallic single-walled carbon nanotubes," *Nano Letters,* vol. 8, pp. 1417-1422, May 2008.

[121] A. A. Green and M. C. Hersam, "Ultracentrifugation of single-walled nanotubes," *Materials Today,* vol. 10, pp. 59-60, Dec 2007.

[122] V. Singh, B. Saswat, and S. Kumar, "Low temperature deposition of Indium tin oxide (ITO) films on plastic substrates," San Francisco, CA, United states, 2005, pp. 139-144.

[123] Z. Chen, B. Cotterell, and W. Wang, "The fracture of brittle thin films on compliant substrates in flexible displays," *Engineering Fracture Mechanics,* vol. 69, pp. 597-603, 2002.

[124] S. S. Cohen, "Contact resistance and methods for its determination," *Thin Solid Films,* vol. 104, pp. 361-79, 1983.

[125] H. Ueng, D. B. Janes, and K. J. Webb, "Error analysis leading to design criteria for transmission line model characterization of ohmic contacts," *IEEE Transactions on Electron Devices,* vol. 48, pp. 758-766, 2001.

[126] I. Yamaguchi and T. Yamamoto, "Soluble self-doped single-walled carbon nanotube," *Materials Letters,* vol. 58, pp. 598-603, 2004.

[127] R. Graupner, J. Abraham, A. Vencelova, T. Seyller, F. Hennrich, M. M. Kappes, A. Hirsch, and L. Ley, "Doping of single-walled carbon nanotube bundles by Bronsted acids," *Physical Chemistry Chemical Physics,* vol. 5, p. 5472, 2003.

[128] J. L. Blackburn, T. M. Barnes, M. C. Beard, Y.-H. Kim, R. C. Tenent, T. J. McDonald, B. To, T. J. Coutts, and M. J. Heben, "Transparent Conductive Single-Walled Carbon Nanotube Networks with Precisely Tunable Ratios of Semiconducting and Metallic Nanotubes," *ACS Nano,* vol. 2, pp. 1266-1274, 2008.

[129] T. M. Barnes, J. L. Blackburn, J. van de Lagemaat, T. J. Coutts, and M. J. Heben, "Reversibility, dopant desorption, and tunneling in the temperature-dependent conductivity of type-separated, conductive carbon nanotube networks," *ACS Nano,* vol. 2, pp. 1968-1976, 2008.

[130] M. Grujicic, G. Cao, and R. Singh, "The effect of topological defects and oxygen adsorption on the electronic transport properties of single-walled carbon-nanotubes," *Applied Surface Science,* vol. 211, pp. 166-183, 2003.

[131] S. O. Kasap, *Principles of electronic materials and devices*, 2nd ed. ed. Boston :: McGraw-Hill, 2002.

[132] D. Cahen and A. Kahn, "Electron energetics at surfaces and interfaces: Concepts and experiments," *Advanced Materials,* vol. 15, pp. 271-277, 2003.

[133] D. Tasis, N. Tagmatarchis, A. Bianco, and M. Prato, "Chemistry of carbon nanotubes," *Chemical Reviews,* vol. 106, pp. 1105-1136, Mar 2006.

[134] M. W. Davis, A. H. Fanney, and B. P. Dougherty, "Prediction of building integrated photovoltaic cell temperatures," *Transactions of the ASME. Journal of Solar Energy Engineering,* vol. 123, p. 200, 2001.

[135] C. Yang, J. Hawthorne, B. Steele, R. Bryant, D. Sowell, D. Maloney, and K. Ip, "Inspecting wafers using a potential difference imaging sensor method," *MICRO,* vol. 23, pp. 55-60, 2005.

[136] S. Suzuki, C. Bower, Y. Watanabe, S. Heun, T. Kiyokura, K. G. Nath, T. Ogino, W. Zhu, and O. Zhou, "Electronic structure of multi-walled carbon nanotubes studied by photoemission spectroscopy," *AIP Conference Proceedings,* p. 193, 2001.

[137] K. Ryu, D. Zhang, X. Liu, E. Polikarpov, M. Tompson, and C. Zhou, "Transparent, conductive and flexible carbon nanotube films and their application in organic light emitting diodes," San Francisco, CA, United States, 2006, pp. 19-24.

[138] L. Jianfeng, H. Liangbing, W. Lian, Z. Yangxin, G. Gruner, and T. J. Marks, "Organic light-emitting diodes having carbon nanotube anodes," *Nano Letters,* vol. 6, pp. 2472-7, 2006.

[139] M. Bockrath, D. H. Cobden, J. Lu, A. G. Rinzler, R. E. Smalley, L. Balents, and P. L. McEuen, "Luttinger-liquid behaviour in carbon nanotubes," *Nature,* vol. 397, pp. 598-601, 1999.

[140] D. J. Bae, K. S. Kim, Y. S. Park, E. K. Suh, K. H. An, J.-M. Moon, S. C. Lim, S. H. Park, Y. H. Jeong, and Y. H. Lee, "Transport phenomena in an anisotropically aligned single-wall carbon nanotube film," *Physical Review B,* vol. 64, p. 233401, 2001.

[141] V. Skakalova, A. B. Kaiser, Y. S. Woo, and S. Roth, "Electronic transport in carbon nanotubes: From individual nanotubes to thin and thick networks," *Physical Review B,* vol. 74, p. 10, Aug 2006.

[142] A. B. Kaiser, V. Skákalová, and S. Roth, "Modelling conduction in carbon nanotube networks with different thickness, chemical treatment and irradiation," *Physica E: Low-dimensional Systems and Nanostructures,* vol. 40, pp. 2311-2318, 2008.

[143] M. E. Itkis, S. Niyogi, M. E. Meng, M. A. Hamon, H. Hu, and R. C. Haddon, "Spectroscopic Study of the Fermi Level Electronic Structure of Single-Walled Carbon Nanotubes," *Nano Lett.,* vol. 2, pp. 155-159, 2002.

[144] T. Tanaka, H. Jin, Y. Miyata, S. Fujii, H. Suga, Y. Naitoh, T. Minari, T. Miyadera, K. Tsukagoshi, and H. Kataura, "Simple and Scalable Gel-Based Separation of Metallic and Semiconducting Carbon Nanotubes," *Nano Letters,* vol. 0.

[145] M. C. Hersam, "Progress towards monodisperse single-walled carbon nanotubes," *Nat Nano,* 2008.

[146] T. W. Odom, J. L. Huang, P. Kim, and C. M. Lieber, "Atomic structure and electronic properties of single-walled carbon nanotubes," *Nature,* vol. 391, pp. 62-64, Jan 1998.

[147] J. W. Mintmire and C. T. White, "Universal density of states for carbon nanotubes," *Physical Review Letters,* vol. 81, pp. 2506-2509, Sep 1998.

[148] P. G. Collins, K. Bradley, M. Ishigami, and A. Zettl, "Extreme oxygen sensitivity of electronic properties of carbon nanotubes," *Science,* vol. 287, pp. 1801-1804, Mar 2000.

[149] Y. Miyata, K. Yanagi, Y. Maniwa, and H. Kataura, "Optical properties of metallic and semiconducting single-wall carbon nanotubes," *Physica Status Solidi B-Basic Solid State Physics,* vol. 245, pp. 2233-2238, Oct 2008.

[150] A. Behnam and A. Ural, "Computational study of geometry-dependent resistivity scaling in single-walled carbon nanotube films," *Physical Review B,* vol. 75, Mar 2007.

[151] T. W. Ebbesen, H. J. Lezec, H. Hiura, J. W. Bennett, H. F. Ghaemi, and T. Thio, "Electrical conductivity of individual carbon nanotubes," *Nature,* vol. 382, pp. 54-56, Jul 1996.

[152] M. S. Fuhrer, Nyg, aring, J. rd, L. Shih, M. Forero, Y.-G. Yoon, M. S. Mazzoni, nbsp, C., H. J. Choi, J. Ihm, S. G. Louie, A. Zettl, and P. L. McEuen, "Crossed Nanotube Junctions," *Science,* vol. 288, pp. 494-497, April 21, 2000 2000.

[153] H. H. Berger, "CONTACT RESISTANCE AND CONTACT RESISTIVITY," *Journal of the Electrochemical Society,* vol. 119, pp. 507-514, 1972.

[154] C. Lan, P. Srisungsitthisunti, P. B. Amama, T. S. Fisher, X. Xu, and R. G. Reifenberger, "Measurement of metal/carbon nanotube contact resistance by adjusting contact length using laser ablation," *Nanotechnology,* vol. 19, p. 125703, 2008.

[155] H. H. Berger, "Models for contacts to planar devices," *Solid-State Electronics,* vol. 15, pp. 145-58, 1972.

[156] K. K. Shih and J. M. Blum, "CONTACT RESISTANCES OF AU-GE-NI, AU-ZN AND AL TO III-V COMPOUNDS," *Solid-State Electronics,* vol. 15, pp. 1177-&, 1972.

[157] J. G. J. Chern and W. G. Oldham, "DETERMINING SPECIFIC CONTACT RESISTIVITY FROM CONTACT END RESISTANCE MEASUREMENTS," *Ieee Electron Device Letters,* vol. 5, pp. 178-180, 1984.

[158] W. Shockley, "Research and investigation of inverse epitaxial UHF power transitors," Air Force Atomic Laboratory, Wright-Patterson Air Force Base, Ohio A1-TOR-64-207, September, 1964 1964.

[159] S. Oussalah, B. Djezzar, and R. Jerisian, "A comparative study of different contact resistance test structures dedicated to the power process technology," *Solid-State Electronics,* vol. 49, pp. 1617-22, 2005.

[160] D. L. Meier and D. K. Schroder, "CONTACT RESISTANCE: ITS MEASUREMENT AND RELATIVE IMPORTANCE TO POWER LOSS IN A SOLAR CELL," *IEEE Transactions on Electron Devices,* vol. ED-31, pp. 647-653, 1984.

[161] D. K. Schroder and D. L. Meier, "SOLAR CELL CONTACT RESISTANCE - A REVIEW," *IEEE Transactions on Electron Devices,* vol. ED-31, pp. 637-647, 1984.

[162] M. M. Hilali, K. Nakayashiki, C. Khadilkar, R. C. Reedy, A. Rohatgi, A. Shaikh, S. Kim, and S. Sridharan, "Effect of Ag particle size in thick-film Ag paste on the electrical and physical properties of screen printed contacts and silicon solar cells," *Journal of the Electrochemical Society,* vol. 153, pp. 5-11, 2006.

[163] E. Limpert, W. A. Stahel, and M. Abbt, "Log-normal distributions across the sciences: Keys and clues," *Bioscience,* vol. 51, pp. 341-352, May 2001.

[164] B. V. Zeghbroeck, "Principles of Semiconductor Devices," 2007.

[165] *CRC handbook on Chemistry and Physics* 2008.

[166] J. K. Lee, W. L. Ma, C. J. Brabec, J. Yuen, J. S. Moon, J. Y. Kim, K. Lee, G. C. Bazan, and A. J. Heeger, "Processing additives for improved efficiency from bulk heterojunction solar cells," *Journal of the American Chemical Society,* vol. 130, pp. 3619-3623, Mar 2008.

[167] M. W. Rowell, M. A. Topinka, M. D. McGehee, H.-J. Prall, G. Dennler, N. S. Sariciftci, L. Hu, and G. Gruner, "Organic solar cells with carbon nanotube network electrodes," *Applied Physics Letters,* vol. 88, p. 233506, 2006.

[168] S. Yoo, B. Domercq, and B. Kippelen, "Efficient thin-film organic solar cells based on pentacene/C60 heterojunctions," *Applied Physics Letters,* vol. 85, pp. 5427-5429, 2004.